Development of a terahertz time-domain spectrometer optimized at 5-8 THz and the study of surface polaritons in NiO-$SrTiO_3$ nano-composite ceramics

by

Ilya D. Vugmeyster

A dissertation submitted in partial fulfillment
of the requirements for the degree of
Doctor of Philosophy
(Applied Physics)
in The University of Michigan
2013

Doctoral Committee:

Professor Roberto D. Merlin, Chair
Assistant Professor Julie S. Biteen
Professor John W. Halloran
Associate Professor Jennifer P. Ogilvie
Research Scientist John F. Whitaker

ACKNOWLEDGEMENTS

The completion of a doctoral dissertation is a long journey, but I would like to acknowledge here that it was not without good fortune and support from many helpful colleagues. I have also made many friends in Ann Arbor over the past seven years who have been instrumental in keeping me in good spirits and I look forward to more good times with them in the future!

With regard to academics, I would like to thank my advisor Prof. Roberto Merlin for guiding me to maturity as a scientist over the years. His deep sense of physics and intuition for experiments has transferred gradually to me and I am deeply grateful for the profit.

I would like to thank Prof. John Whitaker for the extensive guidance, especially during important moments. In some sense, he was my co-advisor on THz techniques and I am grateful for the chance to work in his lab for almost two years at the Center for Ultrafast Optical Science where I learned a great deal.

And thank you to the rest of my committee: Prof. John Halloran, Prof. Julie Biteen and Prof. Jennifer Ogilvie. You have been extremely helpful and kind with your time, lab equipment, guidance and dissertation advice from which I have benefited.

I would like to express deep appreciation to Zhengjiu Xu and Prof. Youxue Zhang at the Geology department for being so generous with their lab and for teaching me how to prepare and polish samples–a skill that has been invaluable. I am also grateful to Pilar Herrera-Fierro and Sandrine Martin at the Lurie Nanofabrication Facility for

help with the metrology and wet-chemistry.

I would like to thank the many academic mentors at the University of Michigan: Prof. Ted Norris, Prof. Kim Winick, Prof. Almantas Galvanauskas, Prof. Herb Winful, Prof. Leopoldo Pando-Zayas, Prof. Duncan Steel, Prof. Cagliyan Kurdak, Prof. James Freudenberg and others. You have guided and inspired me to pursue a new academic path which turned out to be challenging, but very rewarding.

With regard to the detailed aspects of this dissertation, I would like to thank again Prof. Whitaker for the THz-TDS work; Prof. Halloran's Lab, Vladka Tomeckova, Cory Knill and Keilor Kastella for help with the ceramic fabrication and characterization; Prof. Basov's Lab and Greg Andreev for the FTIR reflectance measurements; and Prof. Lockwood for providing the CoF_2 single crystal. I have benefitted especially from these collaborations and the results of this dissertation owe a great deal to them.

Last but not least, I would like to thank all of my cool lab mates for the collaboration and camaraderie, and to state for the record that I have learned almost everything I know about experimental science bit by bit from you. The people that I have had the luck of working with include: Dr. Paul Jacobs, Dr. Daimian Wang, Dr. Mariano Trigo, Dr. Vladimir Stoica, Dr. Bianca Jackson, Dr. Galen Chen, Dr. Dong-Joon Lee, Dr. Charles Divin, Dr. Dong Sun, Dr Jingjing Li, Dr. Andrea Bianchini, Dr. Vladka Tomeckova, Dr. Matt Crites, Dr. Hailing Cheng, Cory Knill, Keilor Kastella, Daniel Stephan, Lei Jiang, Prashant Padmanabhan, Jessica Ames, Alexis Toulouse, Steve Young, Ibrahim Boulares, Meredith Henstridge, Ben Isaacoff, Momchil Mihnev and many others. To those of you nearing the end of your studies I wish the best of luck.

Finally and most importantly I would like to thank my family for the bottomless support which has made this work and the final result possible.

TABLE OF CONTENTS

LIST OF FIGURES

Figure

LIST OF APPENDICES

Appendix

CHAPTER I

Introduction

This thesis is divided into two parts that describe the main experimental thrusts making up this dissertation. The first is centered around the development of a THz time-domain spectrometer optimized for high frequency operation in the 5-8 THz range and in the second half we describe how this system is applied, in addition to other methods, to study the optical properties of a magneto-dielectric composite made up of ferroelectric Strontium Titanate (STO) inclusions inside a host of antiferromagnetic Nickel Oxide (NiO) which holds promise for bulk negative refraction.

Terahertz time-domain spectroscopy has become a popular tool for imaging applications and spectroscopic study of plasmonic based metamaterials, negative refraction, explosives and more traditional condensed matter investigations of characteristic vibrational and magnetic modes in the far-infrared wavelength range. [1] The popularity of this technique stems in part due to the wide availability of ultrafast Ti:sapphire based laser systems with which a THz emitter and detector pair can be combined. The accessibility, high signal-to-noise ratio (SNR) and ability to measure the time evolution of the field, thereby receiving double the information–amplitude and phase–have made this technique competitive with conventional Fourier Transform Infrared Spectroscopy (FTIR) methods. [2] Unfortunately, one of the main drawbacks of this approach is that the spectral sensitivity is typically limited to fre-

quencies below 6 THz, which leaves many interesting phenomena at high frequencies out of reach. [3, 4] In spectroscopic measurements additional losses are usually introduced due to the sample under investigation (reflection or transmission losses) and due to optics in the THz beam path, which reduces the available bandwidth further. [5] Taking these requirements into account and in part being motivated by some of our earlier measurements that lacked the necessary high-frequency signal, we have developed a system based on optical rectification and electro-optic sampling in Gallium Phosphide (GaP) capable of measurements in the range of 0.5 to 8 THz, driven by a 50 fs Ti:sapphire oscillator laser. The dispersion of the refractive index due to an infrared active phonon allows to achieve collinear phase matching between the near infrared pump beam and the generated THz pulse. The conversion efficiency is optimized at 5-8 THz, where typical systems tail off. The capability of the system is demonstrated by a spectroscopic reflectance measurement of a well-characterized material and by comparing the system to a commercially available photoconductive (PC) emitter. We show that our system has a factor of ~ 30 improvement to power conversion efficiency at 7 THz in comparison to the PC emitter which is designed for high power, broadband operation. On the theoretical side, we describe the emission, propagation and detection of THz pulses in the system in a unified framework taking into account the filtering that is introduced due to diffraction both inside the generating crystal and due to apertures of the collimating/focusing optics. We find that, in the absence of nonlinear saturation effects, the optimum high frequency generation occurs when the optical excitation beam is focused to a spot size equal to or smaller than the terahertz wavelength. We also measure and discuss the power scalability of this technique which has the potential to produce THz powers up to 20 μW by scaling up the pump power at similar operating conditions.

We employ a THz-TDS system in addition to FTIR and scanning electron microscopy (SEM) in the second half of this dissertation work to study the NiO-STO

composite ceramic system. This particular structure and the idea behind the project fits into the broad area of surface polariton photonics also known as plasmonics, for which we now give a brief overview. [6, 7] The name plasmonics is derived from the fact that metals are typically used in such applications for which the electromagnetic wave solutions are in the form of coupled electron plasma and light oscillations known as plasmon-polaritons. The central and most appealing feature of plasmonics is that the localization or restriction of the metal in one or more dimensions allows it to sustain electromagnetic radiation that is confined to the surface/interface such that the energy is also confined, leading to the name surface polaritons. In order to sustain localized surface modes, the material must contain a frequency region of negative electric permittivity, which for metals occurs below the plasma frequency in the visible wavelength range. Since the region of negative permittivity is the only requirement, [8] other types of materials may be used to accomplish the same effect. For example, ionic crystals contain vibrational resonances that induce negative regions of electric permittivity in the far-infrared range in which case the surface effects are due to phonon-polaritons. [9] Irrespective of the material used, the dispersion relation or natural frequencies of the surface polariton excitations are dependent on the geometric structure and may be engineered in a wide region of negative permittivity. Due to the recent advancements in material processing and fabrication techniques such as electron beam lithography, focused ion beam milling and specialized 3D self-assembly approaches, [10] it is possible to structure the interfaces with nanometer precision so that the electromagnetic energy may be controlled, guided and localized well below the wavelength of light for various applications which leads to nano-scale, sub-diffraction-limited operation. The virtue of nano-scale design is driven of course by the computing and electronics industries where the miniaturization of functional components and devices is key. Some of the hottest areas of plasmonics today include: nano-waveguiding [11], surface enhanced fluorescence and

Raman scattering which allows detection of single molecules, [6, 12] chemical and biological sensing which uses the fact that the surface-plasmon frequency depends on the surrounding environment, [12] nonlinear optical material engineering where the localization of intensity leads to enhanced nonlinear interactions, [6, 7] plasmonic absorption enhancement in solar photo-voltaic devices [13] and meta-materials for negative refraction and super-resolution imaging [6, 9, 14].

Our work fits into the meta-material sub-field of plasmonics which may be regarded as an independent field due to its popularity and wide range of research. [14] However, because plasmonics typically describes the underlying physics of metamaterial device operation and because the composites we fabricated rely on plasmonic (surface phonon-polariton) resonances of the inclusions, here we emphasize the umbrella plasmonics aspect.

Metamaterials are engineered electromagnetic media made up of scattering subunits that collectively serve to create a desirable electromagnetic property difficult to find or achieve in natural substances. The size of the unit cell is significantly smaller than the wavelength of light so that an effective, homogeneous material is seen by the light. The building blocks or unit cells are typically made up of resonant plasmonic metal structures as discussed above that are designed to produce tunable effective electric and magnetic permeabilities in the composite medium. The original motivation of this research was to implement a double negative (where the electric permittivity $\epsilon < 0$ and magnetic permeability $\mu < 0$) substance as postulated by Veselago more than forty years ago [15] thereby yielding an effective negative index of refraction which is not known to exist in any natural substance in the infrared and visible wavelength ranges. A negative-index medium (NIM) possesses many interesting reversed properties from a scientific point of view: negative refraction at an interface between a positive and a negative index medium, reversed Doppler shift, reversed Cerenkov cone and reversed energy flow relative to phase velocity [15]. From

the applications point of view, the most appealing feature of NIMs is their ability to produce super-resolution lenses–that is, lenses not limited by the fundamental diffraction limit which restricts the minimum focal spot to a size comparable to the wavelength of light [16]. Due to the fact that it is easier to produce unit cell structures with micron-sized geometry, metamaterials have found active use in THz technology for the design of absorbers, switching and modulation devices where the wavelength of light is one the order of 100 μm. [17]

Despite the numerous advances toward the production of metamaterial NIMs there remain significant obstacles. The most popular and groundbreaking design of meta-NIM was done by Smith and co-workers [18] which relied on a combination of split ring resonators (SRR) and metal wires arranged in a cubic lattice. The SRRs are resonant circuits that produced loop currents responsible for negative μ, whereas the metal wires served as the dilute plasma material with negative ϵ. However, the material operated at 5 GHz which is significantly lower than the visible frequencies where NIMs are sought and was composed of a finite number of layers which does not result in a truly bulk medium. As a result, the focus of researchers has shifted toward correcting these two shortcomings. [19] Soon after, there followed a down-scaled metamaterial at higher terahertz frequencies, [20] however, this was a 2D planar structure. The most recent and sophisticated advances have yielded either multilayer, but still 2D structures at visible wavelengths [21] or nearly 3D NIMs at telecommunication wavelengths [22], with both approaches requiring significant efforts at microfabrication. As mentioned above, at terahertz frequencies metamaterial development is also a vibrant research area because of the numerous applications in this spectral range, [17] however, structural design is also typically limited to two dimensions due to the challenges in fabrication. [10]

The second part of this thesis involves the fabrication and study of a composite ceramic metamaterial with the ultimate goal of producing a bulk NIM in the terahertz

frequency range. Unlike the SRRs that have been used to achieve the magnetic response by Smith et. al., [18] we chose to use the magnetic resonance of a natural substance with the antiferromagnets being the best candidates known to have strong magnetic-dipole active resonances in the terahertz frequency range [18]. Even though antiferromagnetic resonance (AFMR) phenomena typically have narrow linewidths, it is possible to tune the location of the resonance using temperature and pressure dependence. The material chosen for this purpose is Nickel Oxide (NiO) which has an AFRM at 1 THz and serves as the magnetically active host matrix. The advantage of this approach is that we obtain a three-dimensional magnetic system as a starting point compared to the finite layer arrays of SRRs. In order to attain negative electric permittivity, the magnetic NiO host is doped with resonant plasmonic inclusions of Strontium Titanate (STO). STO is not a typical plasmonic material because it is not a metal, however the large TO-LO splitting of the infrared-active vibrational mode provides a wide region of negative electric permittivity from 20 to 500 cm^{-1} which accomplishes the same effect with regard to surface mode behavior as metal structures at near infrared wavelengths. The NiO/STO material combination has been fabricated and studied previously [23], however, the proposed interpretation for the effective optical constants was based on weighted averaging of bulk properties as opposed to plasmonic properties. Moreover, no investigation of the resulting effective refractive index was made. It will be shown in the present thesis that geometry-dependent effects of the STO inclusions play a crucial role in determining the effective surface-polariton resonant behavior in the effective composite, the understanding and control of which is key for the design of successful, bulk metamaterials at terahertz frequencies.

The mixtures with low fractions of STO (0-15%) were measured in transmission and reflection geometries in the range of 10-600 cm^{-1}. Based on the transmission measurements, the antiferromagnetic resonance of bulk NiO was observed in the ce-

ramic mixtures in the temperature range of 5-295 K and its temperature dependence was found to agree with the values in the literature of bulk NiO. The magnetic permeability was measured although the oscillator strength of the magnetic mode was not found to be sufficient for negative permeability to occur at room temperature. Pronounced narrowing of the linewidth at 50 K and below makes it possible, in principle, for the permeability to turn negative over a narrow frequency range significantly smaller than one wavenumber around 1 THz, although precise experimental determination of the linewidth with resolution of 0.1 cm^{-1} or better requires further careful investigation.

The dielectric properties of the composite were measured and were found to be determined by surface mode resonances that depend on the shape of STO inclusions. The spectral features can be described well using the framework of the Clausius-Mosotti (CM) theory, taking into account the particle distribution and clustering. The observed reflectance displays a characteristic small-size, surface-mode splitting of the original bulk inclusion resonance into a range of modes in the region of negative permittivity of bulk STO. The three dominant features observed in all samples are: 1) a low frequency, temperature dependent peak at $\sim$ 20-100 cm^{-1} corresponding approximately to the bulk TO soft mode of STO which indicates the onset of a distributed absorption band of the composite, 2) a mode at $\sim$ 260 cm^{-1} which is the dipolar surface plasmon (Fröhlich resonance) of the nearly spherical, single-particle STO inclusions in the quasi-static limit and 3) a broad feature in between the TO and LO frequencies of the bulk STO phonon-polariton which corresponds to clustering and a distribution of particle shapes. The above three features can be interpreted within the framework of vibrational modes of ionic, finite-size STO particles in contrast to the well known phonon-polaritons of infinite crystals. Clustering effects are found to be significant and as a first order approximation clusters are viewed as effective single particle ellipsoids. Inter-particle interactions are included in the mean-field

sense, through the local field effect of the CM approximation. Feature (3) of the transmission and reflection data can be described statistically as a continuous distribution of ellipsoids corresponding to STO particle agglomerates and irregular single particles of varying shapes. The observation of continuous and single-particle features suggests the possibility of engineering ceramics to have desired bulk spectral features such as the strong dielectric resonances required for negative refraction although the particular spherical particle resonance that we see is far-removed from the magnetic behavior of NiO.

A detailed discussion of the above phenomena is organized into three chapters. Chapter two will provide the experimental background and techniques used in collecting the data, including the optical sources, the methods of ultrafast THz generation/detection and the ceramic fabrication technique. Chapter three will describe the high-frequency terahertz time-domain system, taking into account difference frequency generation, electro-optic sampling and propagative diffraction effects; as well as the performance evaluation of the emitter. Chapter four will present the experimental data and theoretical background of the composite NiO-STO project. Lastly, we will outline the strengths of the present findings and possible future research directions in chapter five.

CHAPTER II

Experimental Aspects

2.1 Introduction

Ultrafast time-resolved techniques have become popular and widespread over the past several decades due to the availability of stable optical sources of pulsed picosecond and femtosecond coherent radiation and the numerous applications in the areas of materials research, fundamental science and industrial uses such as metrology and micro-machining where these sources are being used. [24, 25] The present work is focused on applying ultrafast technology for investigating new photonic materials and fundamental optical properties that occur on short time scales with oscillation frequencies in the visible and infrared wavelength ranges. Some examples of the physics under investigation include nonlinear optics, negative refraction and plasmonics where in all cases the unusual properties of light inside matter are utilized or engineered with an eye toward applications such as high resolution imaging, spatially localized light enhancement or the production of coherent radiation in hitherto unattainable frequency ranges. The emphasis of the ultrafast technique is to observe these phenomena in the time-domain. [26] The ultra-short burst of energy from the laser serves as a pump to impulsively excite a dynamical process such as the oscillating vibration of a crystal lattice or a surge current in a biased semiconductor. Following the excitation, it is possible to observe the evolution of the dynamics in

time by gating the process with a second pulse, known as the probe, at precisely controlled time-delays with femtosecond resolution. This technique is known in the ultrafast community as pump-probe; and an important component of it which allows extension of the spectral range of investigation from the visible to the infrared wavelength range is terahertz time-domain spectroscopy (THz-TDS). [1] The idea is to use the ultrafast visible pump pulse for exciting rapidly decaying currents inside either a nonlinear or a photoconducting medium, known as the THz emitter, which produces free-space coherent THz radiation. The emitted THz pulse, which is typically single-cycle and contains a broad spectrum of frequencies, now serves as the pump for studying dynamics in a different frequency range or for imaging applications. However, unlike incoherent blackbody sources of far-infrared radiation, this technique retains its time-domain character since the visible probe pulse is still capable of gating the THz transient thereby measuring directly the free-space terahertz electric field. In this chapter we will review the optical sources that were used in experiments as well as give an overview of the components of the THz time-domain system. A number of experiments were performed at cryogenic temperatures which involved the addition of a cryostat in the propagation path of THz pulses. Finally a big component of the NiO-STO composite work was the fabrication of ceramics and their characterization which will also be presented.

2.2 Optical sources

The ultrafast optical source used in this experiment is a commercial model (Tsunami, Spectra-Physics) titanium-doped sapphire (Ti:sapphire) mode-locked laser in combination with a commercial solid-state pump laser (Millenia Vs, Spectra-Physics) based on the neodymium yttrium vanadate (Nd:YVO_4) gain medium. The Nd:YVO_4 output is frequency doubled by non-critically phase matched (temperature dependent) lithium triborate (LBO) crystal which provides a green pump input for the Ti:sapphire

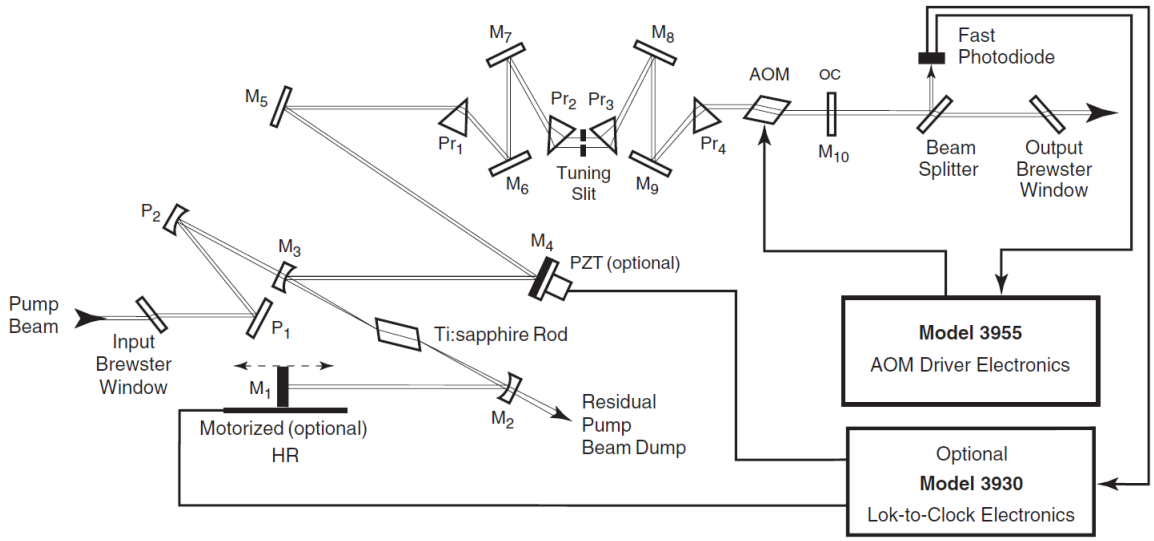

Figure 2.1: Beam path for Tsunami models 3960 and 3941 femtosecond configurations. Taken from [27].

at 532 nm. The Tsunami has a ten-mirror folded cavity design as shown in Fig. 2.1 with a standard set of optics that allows operation in the range of 720-850 nm. A pair of prisms which disperse the light in the cavity in combination with a slit are used for wavelength and pulse width tunability in addition to compensating for group-velocity dispersion (GVD) within the cavity. An acousto-optic modulator ensures mode-locked operation at 82 MHz with an output pulse width of ∼50 fs at optimal conditions. Since the lasing range of the Ti:sapphire crystal is 690-1080 nm, different sets of optics are available for extending the output range. The system is capable of being purged with dry nitrogen for eliminating water vapor absorption lines although we have not found it necessary to use this capability in the standard wavelength range. The Millenia pump laser operates at up to 5.5 W which yields an optimal Tsunami output of 800 mW of average pulsed power. For inelastic Raman scattering experiments which were done for material characterization, an Argon-ion laser (Beamlok 2060, Spectra-Physics) was used which produces continuous-wave output at a number of lines in the blue-to-green wavelength range, with the dominant lines

being: 457.9, 476.5, 488.0, 514.5, 528.7 nm. In order to extend the spectral range for scattering experiments, the Argon-ion was also used as a pump for a home-built continuous-wave Ti:sapphire based cavity with a birefringent-filter which provides wavelength tunability in the near-infrared range at 750-840 nm. Raman scattering was measured using one of two spectrometers: Dilor XY (HORIBA, Ltd.) or the SPEX 1404 (Horiba, Ltd.). [28] Raman scattering was done on powdered samples, where selection rules were not important and a standard 90° collection geometry was employed. [29]

2.3 Terahertz time-domain

The detailed schematic diagram of the THz system is shown in Fig 2.2. The output from the Ti:sapphire laser first makes a double pass through a pair of SF10 flint glass prisms which are used to pre-compensate for the positive group-velocity dispersion (GVD) of the optics further down in the optical path. The prism on the right can be adjusted into and out of the optical path and the prism separation length is fixed to match the total amount of GVD, [25, 30, 31] which in our case is 75 cm. The most dispersive optical elements of the set-up are housed in the optical isolator (OI), which contains a Terbium Gallium Garnet (TGG) Faraday rotation crystal and two Glan-Taylor calcite polarizers, and in the cryostat which contains a pair of plastic (TOPAS COC) windows. Following the splitting of the beam into pump and probe, the amount of dispersion in each path must be approximately equal in order to achieve optimal compensation. Due to the presence of higher order terms in the dispersion effect which cannot be compensated, it is desirable to keep the number of dispersive optical components at a minimum. The optical isolator is used for preventing reflections from going back into the laser cavity which affects the state of mode-locking. With careful alignment of optics further down the path it is possible to avoid the use of the optical isolator. Following the beam-sampler, the majority of

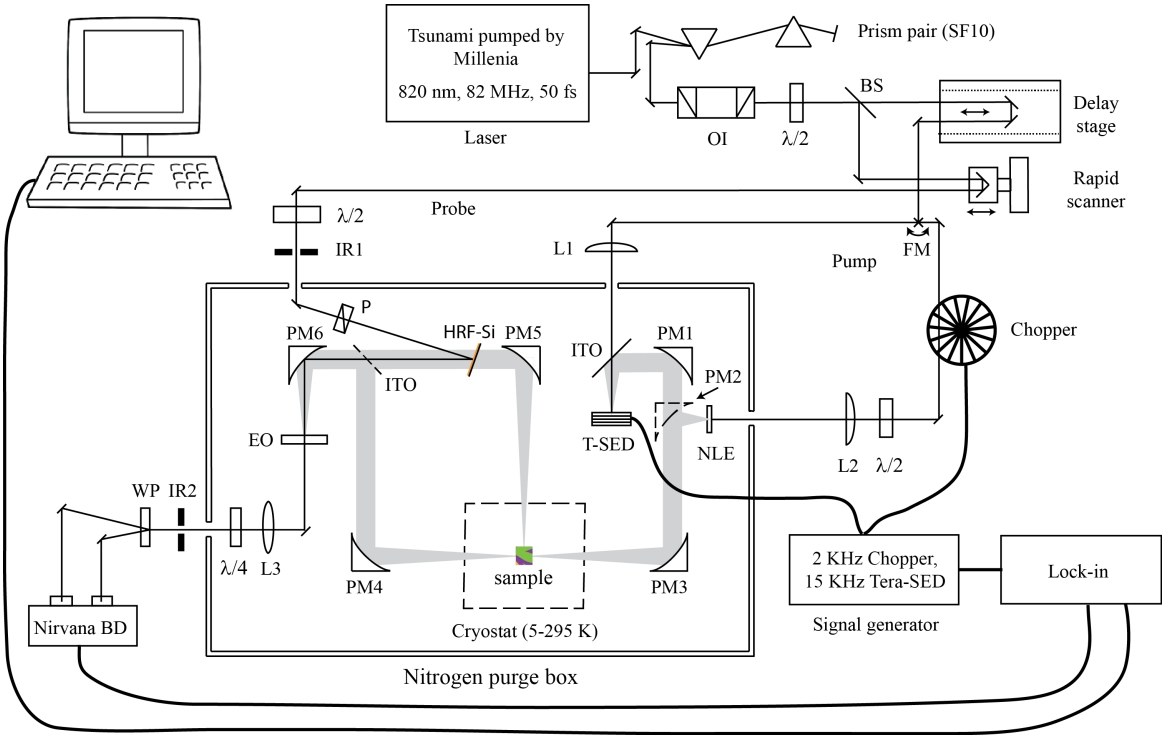

Figure 2.2: Schematic diagram of the terahertz optical set-up. Dashed lines indicate removable components. The abbreviations are: OI–optical isolator, $\lambda/2$–half-wave plate; $\lambda/4$–quarter-wave plate; BS–85% pump, 15% probe beam sampler; FM–flip mirror; L1–25 cm focal length plano-convex lens; L2–25 cm focal length plano-convex lens; L3–7.5 cm focal length bi-convex lens; IR–iris; P–high extinction polarizer; PM–90 ° off-axis parabolic mirror with effective focal length of: 1) 101.6 mm 2) 25.4 mm 3) 101.6 mm 4) 101.6 mm 5) 101.6 mm 6) 50.8 mm; NLE: nonlinear crystal emitter; T-SED–Tera-SED; HRF-Si–near-infrared high-reflection coated silicon dichroic filter; ITO–indium-tin-oxide coated glass slide; EO–electro-optic crystal; WP–Wollaston prism; BD–balanced photo-detector.

the beam (85%) is sent to the delay stage as the "pump" and the rest goes to the rapid scanner as the "probe". The function of the delay stage and the rapid scanner is to create an optical path difference between pump and probe which translates into a time difference of $\Delta t = \Delta d/c$ where c is the speed of light. Thus by scanning the path difference and performing sequential sampling measurements, it is possible to map out the time evolution of the measured process at the detector. The rapid scanner is implemented using a mini-shaker (Bruel & Kjaer 4810) with a mounted retro-reflector driven by a high-current amplifier at 1-5 Hz. This design is used for measuring the signal in real-time during the alignment process, however it is not optimal for precise measurement. For this purpose, the slow linear delay stage (Aerotech, Inc.) is used which scans one point at a time with a prescribed integration time and 0.5 μm resolution. On the pump path, there are two options for the THz emission process– the photoconductive emitter or the nonlinear crystal with the choice being made by adjusting the flip mirror. The photoconductive emitter is used in a backward geometry such that the emitted THz radiation is collected from the same side as the incident optical illumination. There are two choices for the photoconductive (PC) emitter: a commercial Tera-SED (Gigaoptics, GmbH) or a custom made single transmission line dipole antenna fabricated on low temperature grown GaAs (LT-GaAs). These choices and their operating principles will be discussed in the next section. An indium-tin-oxide coated glass slide (resistivity of $< 5\,\Omega/\text{in}^2$) serves as the dichroic filter for transmitting the near-infrared beam and reflecting the emitted THz beam. For the nonlinear emitter, either a slab of (110)-oriented GaP or (110)-oriented ZnTe is used in a collinear phase-matched configuration. Two parabolic mirrors (either PM1/PM3 or PM2/PM3) guide the THz beam toward the sample which may be cooled down to T = 5 K using Janis STVP-400 liquid helium flow cryostat. The sample can be measured either in reflection or transmission geometries, with both paths shown in the schematic, although it cannot be done simultaneously.

Dashed lines indicate the optical components that may be removed for implementing the various configurations. In the case of reflection, the THz beam is steered toward the electro-optic (EO) detection crystal using PM5/PM6, whereas for transmission PM4/ITO/PM6 accomplish the same effect. For each fixed position of the delay stage, the THz electric field is measured using EO detection as will be reviewed in the next section, which is implemented either in GaP or ZnTe nonlinear crystals similarly to the case of THz emission. The field is measured by nonlinear mixing of the THz pulse with the near-infrared probe beam which travel collinearly and are both focused onto the detection crystal. In order to achieve the collinear propagation, a high-reflection coated silicon substrate dichroic filter (SS-HRFZ-SI, Tydex Optics) is used to reflect the near-IR beam at 15° angle of incidence with better than 95% reflectance and simultaneously transmit the THz beam. A high-extinction polarizer is used prior to HRF-Si which is necessary for high-sensitivity, polarization dependent EO detection. The electro-optic effect in the crystal induces phase retardation between the orthogonal polarization components of the probe beam which is proportional to the terahertz electric field. A $\pi/2$ phase shift is introduced by the quarter-wave plate which is a necessary bias point such that the difference in intensities is linear. [32, 33] The beam goes through the Wollaston prism which separates the two orthogonal polarization states, each of which is directed into a separate photodiode of the Nirvana (0901, New Focus, Inc.) detector for balanced detection. Thus the difference signal of the two diodes is proportional to the terahertz electric field that we are measuring. The signal from the photo-detector is used as an input into a lock-in for phase-sensitive detection which results in electric-field sensitivity on the order of 10000:1 relative to the noise floor. As discussed in Wahlstrand's thesis, [34] phase sensitive detection requires the signal be tagged or modulated at a particular frequency such that noise at all other frequencies may be filtered out. For this purpose, we modulate the bias voltage of the PC emitter at 15 KHz or we use an optical chopper at 2 KHz in the

case of nonlinear generation. Finally, the data is routed to a personal computer for automated data collection and retrieval.

2.4 Terahertz generation

As discussed in the experimental layout, the system employs two types of emitters: photoconductive and nonlinear. They have different physical origins, but the same effect of producing oscillating currents that act like radiating antennas of THz radiation. We review the two different approaches below.

2.4.1 Photoconductive emission

Photoconductive emission operates according to the principle of the Auston switch [35]. An incident pulse of energy $\hbar\omega$ that is above the band gap energy of the semiconductor illuminates the surface and produces free carriers. The surface of the semiconductor is biased with an applied electric field by fabricating a pair of transmission lines with a spacing on the order of 10-100 μm. The applied field accelerates the freed carriers which causes a transient current lasting for several picoseconds, with the exact duration being determined by factors such as the duration of the incident pulse, carrier recombination and collision times. The resulting oscillating current will act as a Hertzian dipole antenna emitting terahertz radiation into free space. This radiation is then collected and guided by various optics as described in the previous section. If we assume that the dimension of the excitation source is smaller that the wavelength, then in the far-field the electric field is described by [36],

$$E(r,\theta,t) = \frac{l_e}{4\pi\epsilon_0 c^2 r}\frac{\partial j(t)}{\partial t}\sin\theta \tag{2.1}$$

where $j(t)$ is the current in the dipole, l_e the effective length of the dipole, ϵ_0 the permittivity of free space, c the speed of light and θ the angle relative to the dipole

axis. If we consider a finite surface area being illuminated by the incident beam, then we can express the photocurrent density as

$$j(t) = en(t)v(t) = \sigma(t)E_{in}(t), \tag{2.2}$$

where e is the electron charge, n the surface charge density, v the charge velocity, σ the conductivity and $E_{in}(t)$ the internal electric field. Here we have considered only one type of carrier to simplify the discussion, although in general electrons and holes will be generated. The internal field will be made up of two parts, the bias field and the opposing field due to the separated charges or current which will tend to screen out the bias field [37]. With respect to the properties of the illuminated photoconductor the generated THz field will be determined by the following dynamics,

$$E(t) \propto e[n(t)\frac{dv}{dt} + v(t)\frac{dn}{dt}]. \tag{2.3}$$

The carrier density will be primarily determined by the incident pulse intensity whereas the velocity will be proportional to the internal field in the semiconductor. If we consider the linear regime of low excitation densities such that the screening effect can be neglected then the velocity of the carriers can be expressed simply in terms of the Drude model [38, 39],

$$\frac{dv(t)}{dt} = -\frac{v(t)}{\tau_{col}} + \frac{e}{m}E_b \tag{2.4}$$

where E_b is the bias field that drives the electrons and τ_{col} is the collision time. This equation can be solved easily for $v(t)$. Now consider an impulse of magnitude $I_{opt}\delta(t)dt$ that excites a finite number of carriers, where I_{opt} is the optical intensity.

The resulting photocurrent will be,

$$j_\delta(t) = en(t)v(t) = \frac{e(1-R)(I_{opt}dt)}{\hbar\omega}\exp(-t/\tau_{rel})\frac{\tau_{col}}{m}(1-\exp(-t/\tau_{col}))E_b \qquad (2.5)$$

where we have also taken into account the carrier relaxation rate, τ_{rel}, and R is the reflectivity of the semiconductor. Thus the final photocurrent in terms of the incident intensity and the response times of the photoswitch is [37, 39]

$$j(t) = \frac{e(1-R)}{\hbar\omega}\int_0^\infty I_{opt}(t')\exp(-t'/\tau_{rel})\frac{\tau_{col}}{m}(1-\exp(-t'/\tau_{col}))E_b dt'. \qquad (2.6)$$

It is always desirable to have fast oscillations in the photoconductor such that the emitted pulse will have as broad of a frequency spectrum as possible. Based on the analysis of Eq. 2.6, the upper bound on the frequency spectrum of the pulse will be set primarily by the incident pulse duration which determines the initial spike in the THz transient and to a lesser degree by the relaxation/collision times which will affect the more gradual evolution of the current that happens afterward.

We have used two different photoconductive emitters in this work as shown in Figs. 2.3 and 2.4. The first is an emitter with a 5 μm dipole spacing fabricated on a $\sim$1.5 μm epitaxially grown layer of LT-GaAs on top of semi-insulating GaAs (SI-GaAs) substrate. The low temperature growth of GaAs reduces the carrier lifetime from $\sim$50 ps to $\sim$1 ps as measured by time-resolved reflectance, which improves the operation of the photoconductor for THz applications. The point dipole antenna does not couple out radiation easily to free space because of the high index mismatch between GaAs and air which leads to a critical angle on the order of 15°. For this reason, high-resistivity silicon dome lens is attached to the emitter in order to collimate the radiation. The leads of the transmission lines are wire-bonded to contacts such that bias voltage may be applied which is typically 10 V. This produces an electric bias

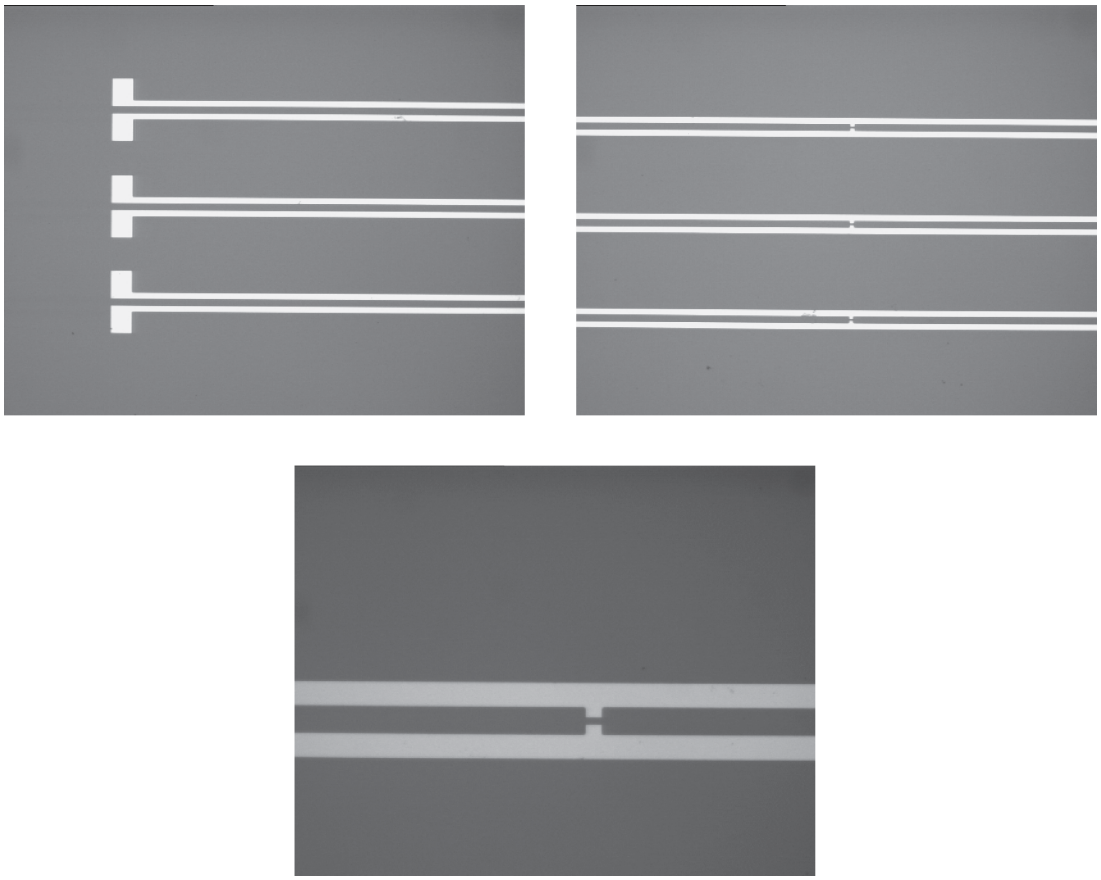

Figure 2.3: Images of the dipole LT-GaAs emitter pattern.

field in the dipole of 20 KV/cm, which is close to the breakdown voltage of the dielectric. The high bias field is important for accelerating the carriers and leads to a linear relationship with the emitted THz field.

The second photoconductive emitter is the Tera-SED (Gigaoptics, GmbH) which is a commercial device designed to produce high output power and a broad frequency spectrum. The principle of operation is the same as with the single dipole, except that an array of such lines is fabricated with 5 μm spacing. Every other line is blocked so that the adjacent currents do not flow in opposite directions as shown in Fig. 2.4. This design allows for a uniform bias field throughout the active area and a more efficient, large-aperture generation. [37, 42] Unlike in the single dipole case, the excitation area is much larger and could extend to several millimeters. The generated terahertz waves are nearly planar so that it is significantly easier to couple out the radiation into free space at normal incidence and a dome lens is not required. Average terahertz powers of 100 μW have been generated from this emitter with 800 mW of average incident power from the Ti:sapphire laser oscillator. [42]

2.4.2 Nonlinear emission

The nonlinear emission of THz pulses is a result of the difference frequency mixing of the frequency components of the optical pulse in the nonlinear medium which induces nonlinear polarization, $\mathbf{P}^{NL}$ and results in oscillating currents that emit THz radiation. For a 50 fs pulse centered at $\omega_0 = 2\pi c/800$ nm the frequency bandwidth is $\Delta\omega/2\pi \sim 10$ THz. If we neglect the diffraction of the optical pulse and take all of the near-infrared frequency components to be collinear then the nonlinear polarization in the medium as a function of distance z is,

$$\begin{aligned} P^{NL}(\Omega, z) &= \epsilon_0 \chi^{(2)}(\Omega) \int_{\omega_0 - \Delta\omega/2}^{\omega_0 + \Delta\omega/2} E(\omega + \Omega) e^{ik_1(\omega+\Omega)} E^*(\omega) e^{-ik_2(\omega)} d\omega \\ &= \epsilon_0 \chi^{(2)}(\Omega) e^{i\Omega z/v_g} I_{opt}(\Omega) \end{aligned} \tag{2.7}$$

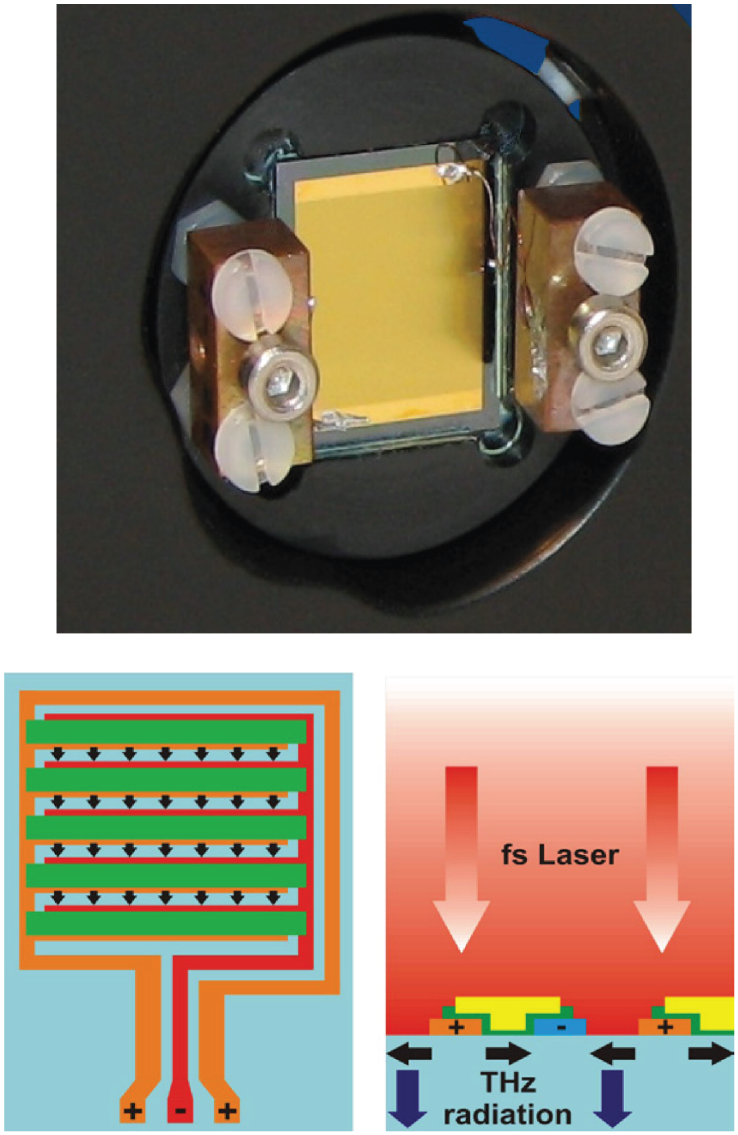

Figure 2.4: Illumination side image (top) and schematic (bottom) of the Tera-SED emitter. Taken from [41].

where $\chi^{(2)}$ is the nonlinear susceptibility, $E(\omega)$ are the frequency components of the optical pulse, v_g is the optical group velocity and $I_{opt}(\Omega)$ is the frequency spectrum of the optical pulse envelope. The second equality follows from the fact that $\Delta\omega \ll \omega_0$ and $k_1(\omega+\Omega) - k_2(\omega) \approx \Omega \frac{dk}{d\omega}|_{\omega_0} = \Omega/v_g$. Thus the near-infrared pulse induces a propagating nonlinear polarization that travels with the group velocity of the pulse and acts as a source of THz waves. From this we will see that for optimum conversion efficiency the velocity of the pulse must match the velocity of the THz wave such that constructive interference can occur. Assuming that the pump does not get depleted, the terahertz field that is generated will be governed by the single vector wave equation, [43]

$$\nabla \times \nabla \times \mathbf{E}(\Omega) - \frac{n^2(\Omega)\Omega^2}{c^2}\mathbf{E}(\Omega) = \mu_0 \Omega^2 \mathbf{P^{NL}}(\Omega) \tag{2.8}$$

where the nonlinear polarization acts as the driving term at the terahertz frequency. This problem has been solved generally for the case of plane-waves in a slab of material, taking into account multiple-reflections and backward propagating waves. [44, 45] However, in practice it is important to focus the pump beam tightly into the nonlinear crystal which allows enhancement of the incident intensity and the resulting THz emission. For this reason, the plane approximation is not appropriate since the optical source is often comparable to or smaller than the THz wavelength. The problem of difference frequency generation in a nonlinear slab, taking into account the size dependence of the optical beam has been solved in [46] using a Green-function formalism. The configuration of the generation set-up is shown in Fig. 2.5 and the optical pulse is incident from the bottom. Based on the above discussion the induced polarization density is given by,

$$\mathbf{P}^{NL}(\Omega, \mathbf{K}; z) = \hat{x} 2\epsilon_0 \chi^{(2)} I_f(\Omega) I_s(K) \exp[(ik_0 n_g - 2\alpha)(z+D)], \tag{2.9}$$

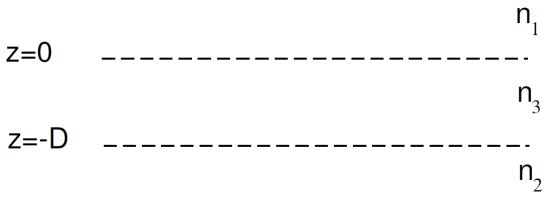

Figure 2.5: Three layer geometry with polarization source in medium with index n_3. Taken from [46].

where $k_0 = \Omega/c$, α is the field absorption coefficient of the optical pulse, $I_s(K) = \exp(-K^2\sigma_0^2/4)$ is the K-space intensity profile of the beam (normalized so that the total power is independent of the spot size), and $I_f(\Omega) = I_0\sqrt{\pi}\tau_0 \exp(-\Omega^2\tau_0^2/4)$ is the optical intensity envelope. The spot size σ_0 and pulse duration τ_0 are the 1/e half-widths. The polarization density in Fourier space is defined by $\mathbf{P}^{NL}(\mathbf{r},t) = \int_0^\infty \frac{d\Omega}{2\pi} \int \frac{d\mathbf{K}}{(2\pi)^2} \mathbf{P}^{NL}(\Omega,\mathbf{K}) \exp(i\mathbf{K}\cdot\mathbf{R})$, where $\mathbf{r} = x\hat{x} + y\hat{y} + z\hat{z} = \mathbf{R} + z\hat{z}$.

The solution for the $\hat{x}$-component of the electric field generated at the exit of the slab is,

$$\begin{aligned}
\hat{x}\cdot\mathbf{E}(\Omega,\mathbf{K}) &= \tfrac{ik_0^2}{w_3}\chi^{(2)}(\Omega) I_f(\Omega) I_s(K) [L_+(\Omega,K) \\
&\times (\tfrac{1}{2}C^s - \tfrac{1}{2}C^s\cos 2\phi + \tfrac{w_1 w_3}{2v_1 v_3}C^p + \tfrac{w_1 w_3}{2v_1 v_3}C^p \cos 2\phi) \\
&+ \exp(2iw_3 D) L_-(\Omega,K) \\
&\times (\tfrac{1}{2}r_{32}^s C^s - \tfrac{1}{2}r_{32}^s C^s \cos 2\phi + \tfrac{w_1 w_3}{2v_1 v_3} r_{32}^p C^p + \tfrac{w_1 w_3}{2v_1 v_3} r_{32}^p C^p \cos 2\phi)]
\end{aligned} \tag{2.10}$$

where

$$L_\pm(\Omega,K) = \frac{\exp(ik_0 n_g D - 2\alpha D) - \exp[\pm iw_3 D]}{[ik_0 n_g - 2\alpha \mp iw_3]} \tag{2.11}$$

are the phase matching factors, $v_i = n_i k_0$, $w_i = (v_i^2 - K^2)^{1/2}$, r_{ij}^s, r_{ij}^p are the reflection coefficients and C^s, C^p are the Fabry-Perot factors for the s- and p-polarization states as defined in [46]. Although the solution is quite complicated, we will see in Chapter 3 that in the phase matched configuration it simplifies considerably. In actual experiments, the angles are small and the beam propagates close to the optical axis.

Due to the critical angle losses, the non-paraxial components of the THz wave do not reach the detector because they cannot couple to free space from the emitter. For this reason, the $K \approx 0$ approximation in the amplitude factors gives very accurate results. However, in the phase factors $L_{\pm}(\Omega, K)$ the full K-dependence must be taken into account so that the internal diffraction effects may be included.

2.5 Terahertz detection

The two detection techniques employed–photoconductive and EO-sampling–are the reverse versions of the generation methods. In the photoconductive case, the dipole antenna of Fig. 2.3 is used without the bias field in order to detect the propagating THz field. The current in the photoswitch will be generated when the probe pulse gates the dipole gap thereby generating free carriers and the acceleration field is provided by the incident THz pulse. Thus the analysis of Eq. 2.6 applies except that $v(t)$ will be a function of $E_{THz}(t)$ instead of E_b. In order to simulate the detected $j(t)$, Eq. 2.4 will have to be solved for some prescribed function of the incident $E_{THz}(t)$.

In the case of EO-sampling, it is easiest to understand the detection concept in terms of the static electro-optic effect. The application of a DC field in an electro-optic crystal produces a change in the refractive index. For (1 1 0)-oriented zinc-blende crystals which includes the GaP and ZnTe slabs that were used, the largest EO effect occurs for the DC field being applied parallel to (1 $\bar{1}$ 0) direction in which case the directions (1 $\bar{1}$ $\sqrt{2}$) and ($\bar{1}$ 1 $\sqrt{2}$) at 45° to the DC field develop the largest difference in the refractive index. [45] Let $\hat{x}$, $\hat{y}$ be the (1 $\bar{1}$ $\sqrt{2}$) and ($\bar{1}$ 1 $\sqrt{2}$), respectively. The induced phase difference between these axes is,

$$\Gamma = \frac{2\pi l}{\lambda_o} n_o^3 r_{41} E_{DC} \tag{2.12}$$

where l is the length of the EO crystal, λ_o is the visible wavelength, n_o is the visible

refractive index, r_{41} is the coefficient of the electro-optic tensor and E_{DC} is the applied field. Thus the induced phase difference is proportional to the applied electric field. If the optical probe beam is also polarized along $(1\ \bar{1}\ 0)$ then after passing through the EO crystal and $\lambda/4$-plate with slow and fast axes aligned along $\hat{x}$, $\hat{y}$ the field components of the probe are,

$$\begin{aligned} E_x &= a_0 \cos(kz - \omega t - \Gamma/2) \\ E_y &= a_0 \cos(kz - \omega t + \Gamma/2 + \pi/2) \end{aligned} \tag{2.13}$$

which describes an elliptical state of polarization with principal axes given by

$$\begin{aligned} a &= a_0(1 + \Gamma/2) \\ b &= a_0(1 - \Gamma/2). \end{aligned} \tag{2.14}$$

The Wollaston prism is oriented with its axes at 45° relative to $\hat{x}$, $\hat{y}$. It follows that the difference signal between the photodiodes is,

$$S = I_a - I_b = \frac{|a|^2}{2} - \frac{|b|^2}{2} = |a_0|^2\Gamma. \tag{2.15}$$

We see that the measured signal with balanced detection $S \propto I_{opt}\chi^{(2)}E_{DC}$ is proportional to the applied DC field. In the experiment, the DC field will be the incident THz pulse that we are measuring which is much slower compared to optical frequencies. In the full analysis the velocity mismatch between the optical group velocity and the THz phase velocity must also be included. We have considered the DC response whereas in fact at every displacement of the delay stage the measurement will be made up of a spectral contribution of THz frequencies each of which experiences a slightly different phase mismatch with respect to the optical pulse. The final result is, [47]

$$S(\tau) \propto \int_{-\infty}^{+\infty} E_{THz}(\Omega) f(\Omega) \exp(-i\Omega\tau) d\Omega, \tag{2.16}$$

where

$$f(\Omega) = I_{opt}(\Omega)\chi^{(2)}(\Omega)\Big[\frac{\exp(i\Omega(n(\Omega) - n_g)l/c) - 1}{i\Omega(n(\Omega) - n_g)l/c}\Big] \tag{2.17}$$

where the last term in $f(\Omega)$ is the phase matching factor as seen earlier in the emission derivation.

2.6 Ceramic fabrication

The composites of Nickel Oxide and Strontium Titanate are made into ceramics from commercially available powders. The four different types of powders are: 1) Nickel (II) Oxide, green, -325 mesh, average size of particle $\sim 5\ \mu m$ (Sigma Aldrich, 399523) 2) Nickel (II) Oxide, nanopowder, less than 50 nm (Sigma Aldrich, 637130) 3) Strontium Titanate, classified as 5 μm but average size based on SEM of $\sim$ 800 nm (Sigma Aldrich, 396141) 4) Strontium Titanate, nanopowder, less than 100 nm (Sigma Aldrich, 517011). The theoretical density of STO is 4.81 g/mL and the density of NiO is 6.67 g/mL. These values were used in order to obtain the proper mixing fraction by volume. Thus, the 85% NiO-15% STO mixture was weighed at 88.7% NiO-11.3% STO by mass. We show in Figs. 2.6 and 2.7 the starting, large-grain powders of STO and NiO, respectively.

The procedure for the ceramic preparation is as follows. Mixing: 1) The powders are mixed in a plastic container with aluminum balls, filled with isopropanol and sealed. 2) Set to mill at $\sim$ 60 revolutions per minute for 24 hours in order to achieve uniform mixing. 3) Extracted into a beaker from the plastic container used for ball milling with a combination of isopropanol and sieve for filtering out the aluminum balls. 4) The beaker is covered and set to dry for at least half a day in an oven at

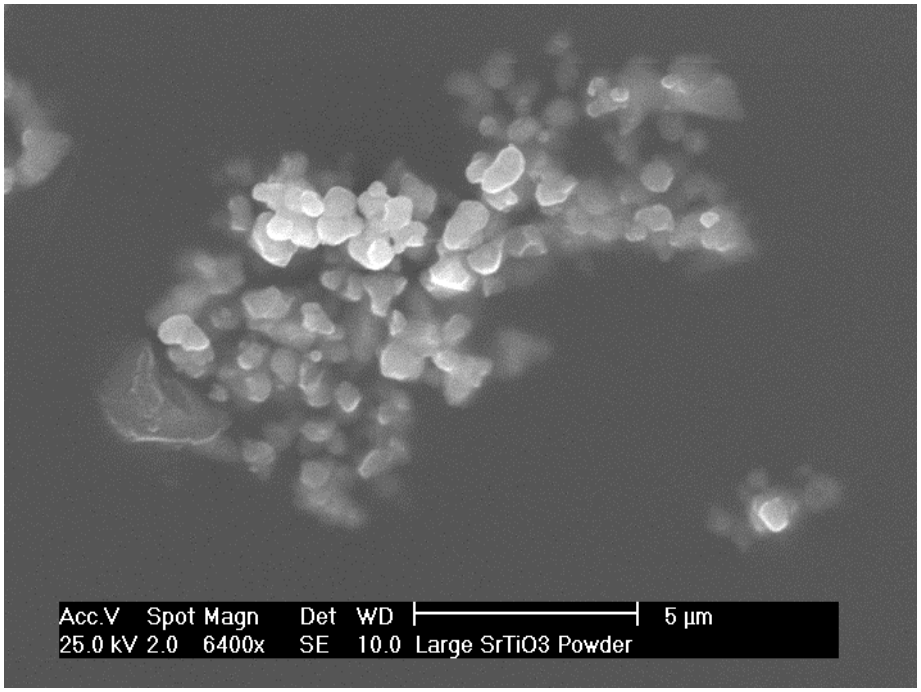

Figure 2.6: Strontium Titanate powder, large grain size.

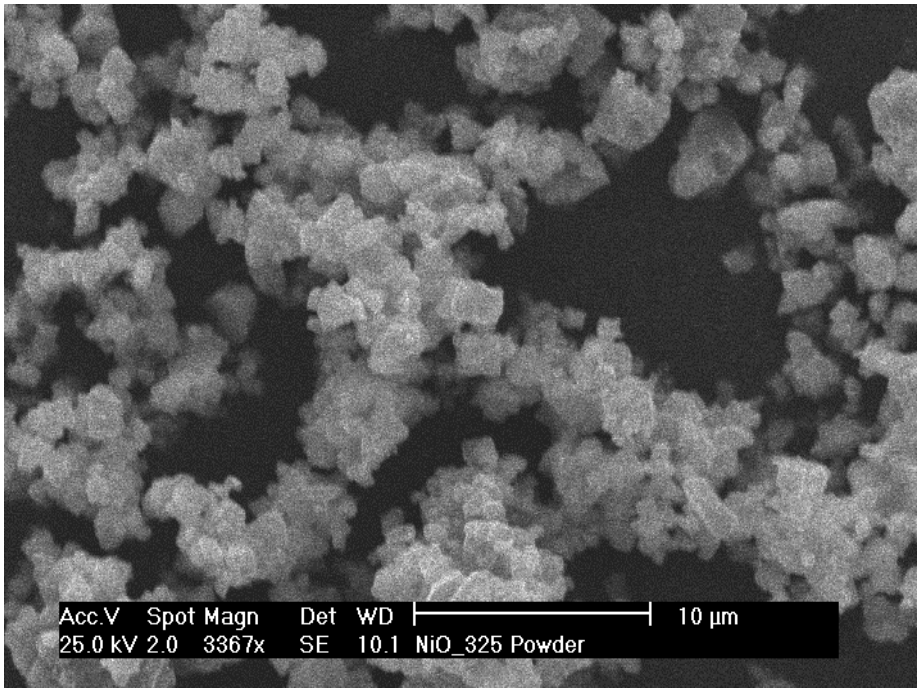

Figure 2.7: Nickel Oxide powder, large grain size.

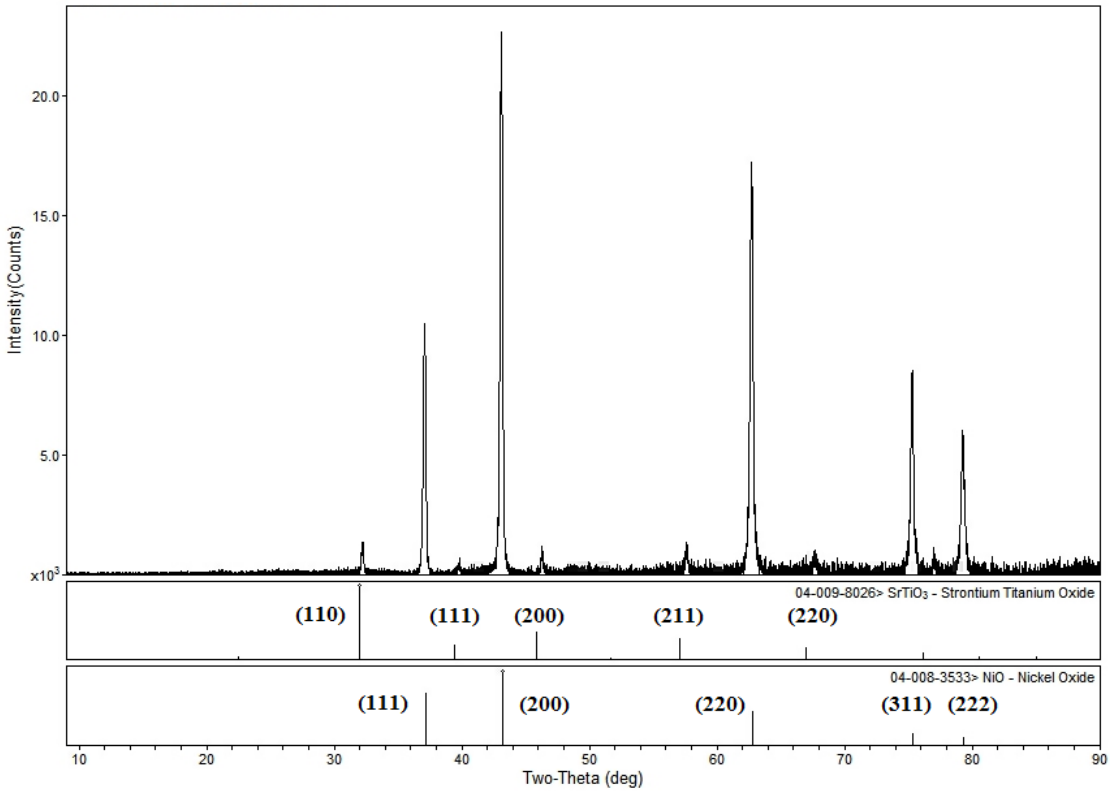

Figure 2.8: XRD results for the sintered 95% NiO-5% $SrTiO_3$ composite.

100°C. 5) The dried and mixed powder is scraped out of the beaker, ground with mortar and pestle, and collected into a vial. Pressing: 1) A mixture of stearic acid and acetone is used to lubricate the die before pressing. 2) 1.5 g of mixed powder is measured, placed into a 0.5 inch diameter die and pressed at 1650 pounds. 3) The crucible is lined with NiO powder and the pressed sample is placed on top in order to avoid contact with the crucible. Sintering: 4) The crucible with the pressed sample is placed into a furnace and ramped from room temperature to 1450°C in 290 minutes. 5) 60 minutes at 1450°C 6) Furnace is shut off and cooled for over 8 hours back to room temperature.

As a last step, the sintered samples are polished in a succession of paper grit sizes from 400 to 1200 followed by 3 μm diamond paste, 1 μm diamond paste and 0.06 μm silica slurry as the final polishing step.

We have evaluated the resulting composites for compatibility with x-ray diffrac-

tion and Raman scattering. Since it is important to retain the two pure phases in the ceramic we must confirm that no chemical reaction takes place between NiO and STO during sintering. Fig. 2.8 shows the x-ray diffraction (XRD) pattern of the 95-5 composite which confirms the two pure phases. No change in the lattice parameter occurs and we do not see additional lines. The relative intensity of the lines confirms the mixing fraction. Raman scattering produces similar results at higher STO concentrations as will be shown in Chapter 4. These results agree with the original findings in [23].

Next, we evaluate the free surface and bulk properties of the composite using SEM. Figs. 2.9-2.11 show a free, as-fired surface of the 95-5 composite in the vicinity of a fracture as well as a magnified version of a void. The small grains are STO inclusions which are slightly less than 1 μm on average and the large grains are NiO on the order of 5 μm. In the 1000x version, we see the fine STO powder scattered over the surface as well as large clusters of STO within the voids in the magnified images.

The optically polished surface is shown in Figs. 2.12-2.14 and is more representative of the bulk. The surface roughness is on the order of several nanometers in the flat areas. The images show some white, powdered streaks which is the residue of the final polishing compound made up of 60 nm silica slurry. There are some deep pits which correspond to pores between the grains as well as shallow pits which could be due to chipping of the inclusion grains on polishing. The total volume of the pits agrees approximately with the theoretical estimate of porosity of 5-10% based on sample density. The darker regions represent the STO inclusions which make up 5% of the volume. The average distance between the inclusions agrees with the theoretical estimate based on Eq. B.1 as is discussed in Appendix B and Chapter 4. Based on the images, we estimate the STO inclusion size in the bulk of 2-3 μm in the 95-5 composite which is larger than the starting particles due to clustering.

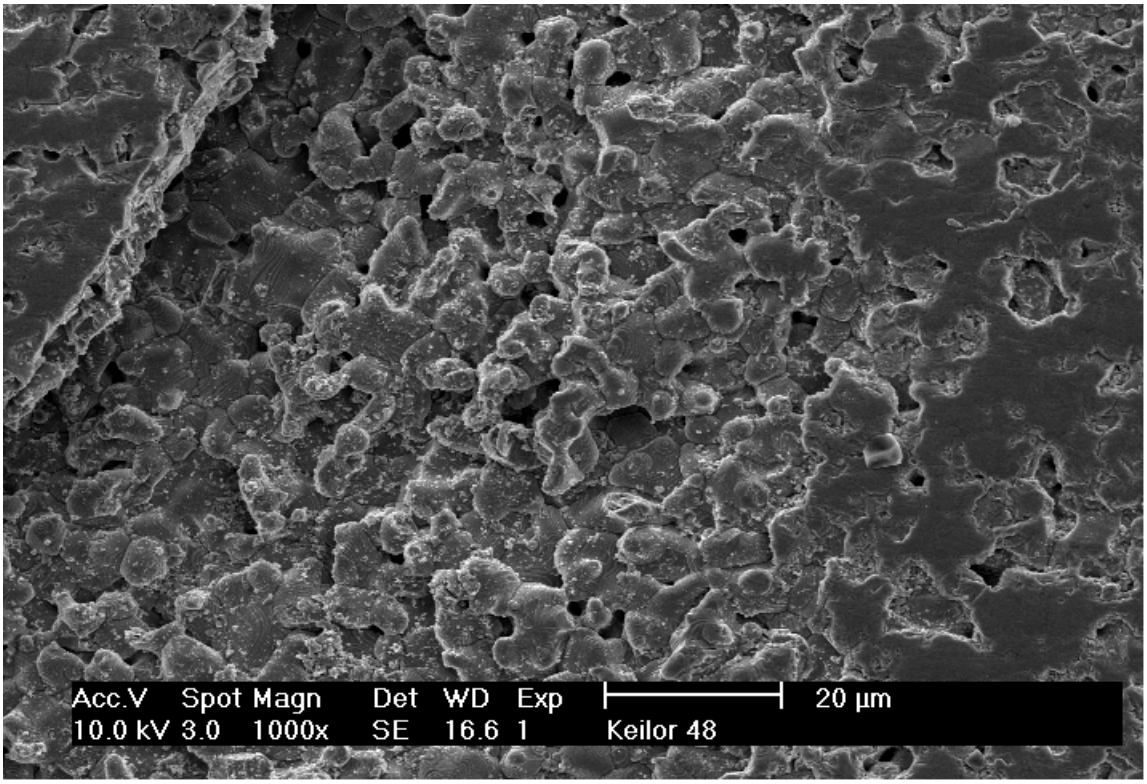

Figure 2.9: 95% NiO-5% $SrTiO_3$ (large grains) at 1000x magnification of a free surface after sintering.

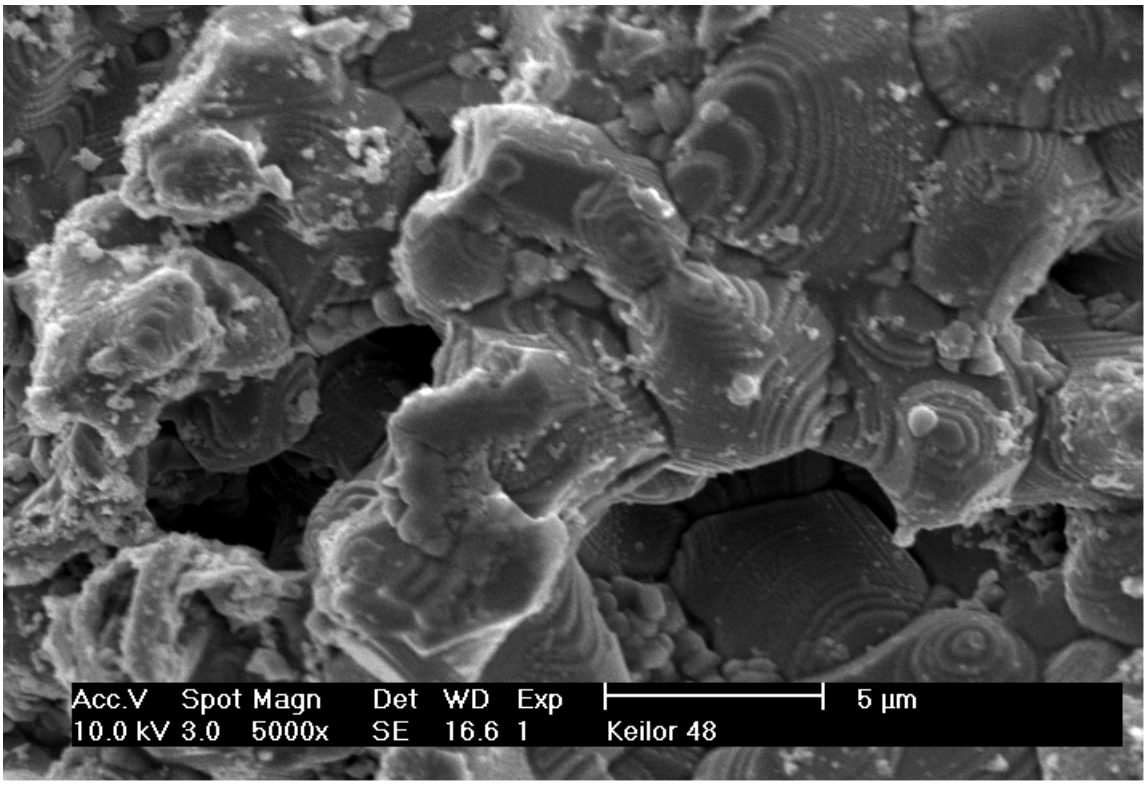

Figure 2.10: 95% NiO-5% $SrTiO_3$ (large grains) at 5000x magnification inside a void of free surface.

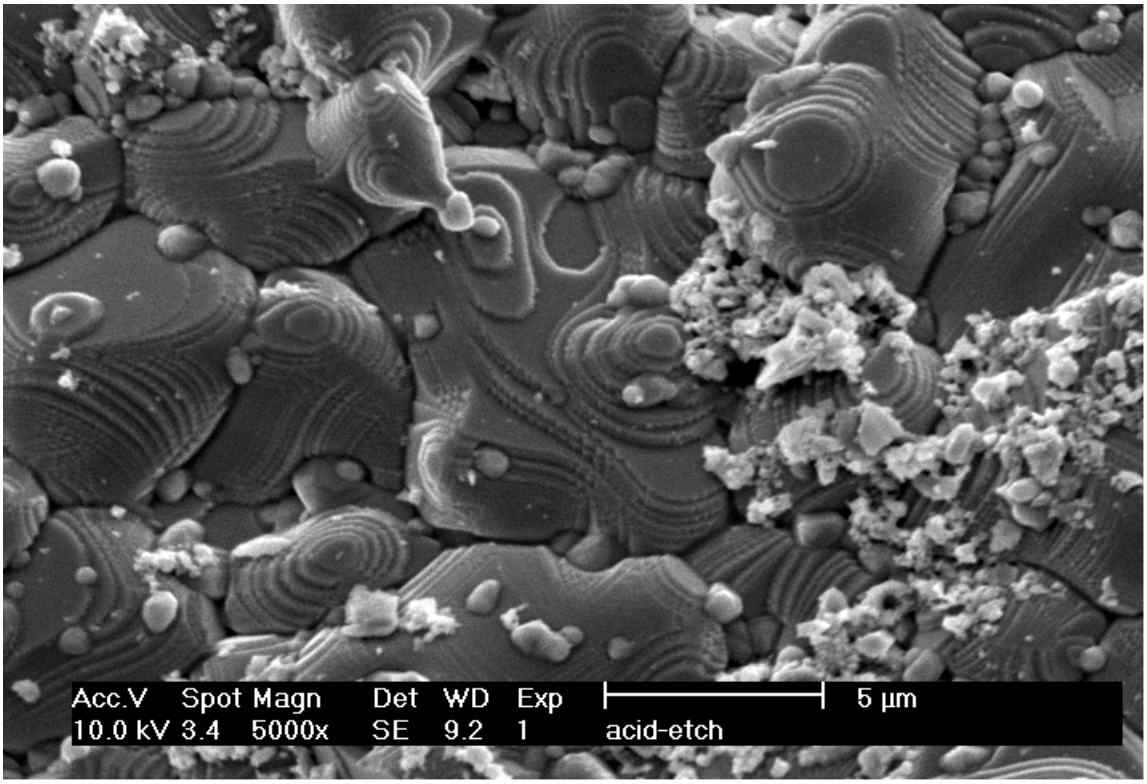

Figure 2.11: 95% NiO-5% $SrTiO_3$ (large grains) at 5000x magnification, acid-etched.

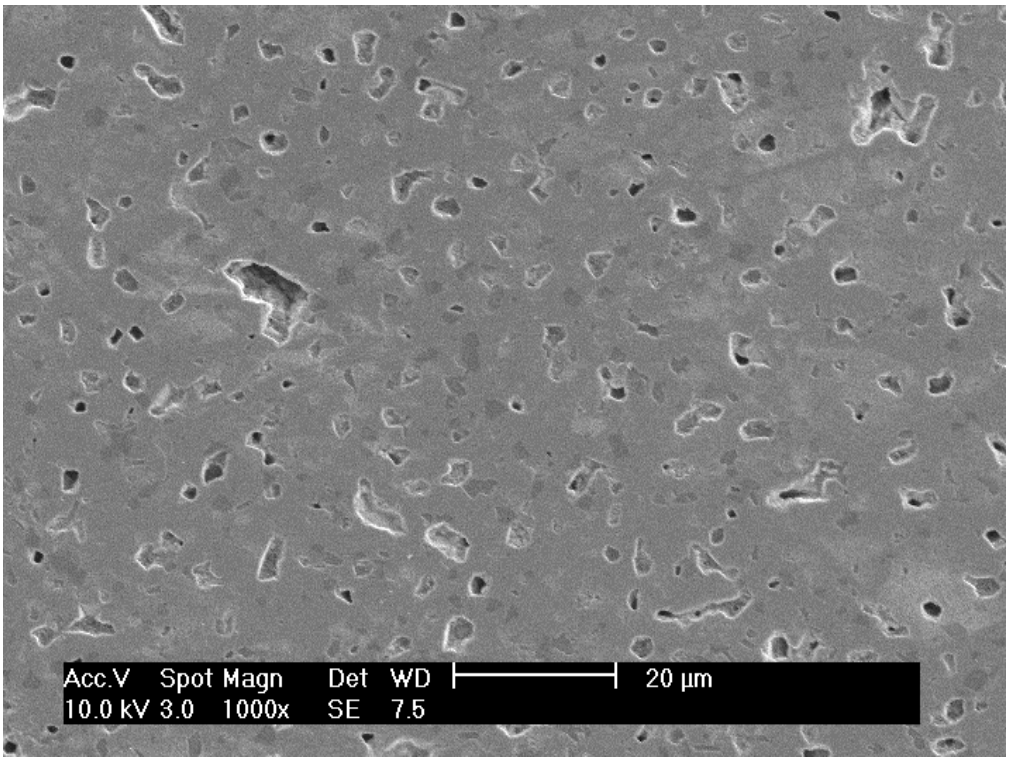

Figure 2.12: 95% NiO-5% $SrTiO_3$ (large grains) at 1000x magnification, optically polished surface.

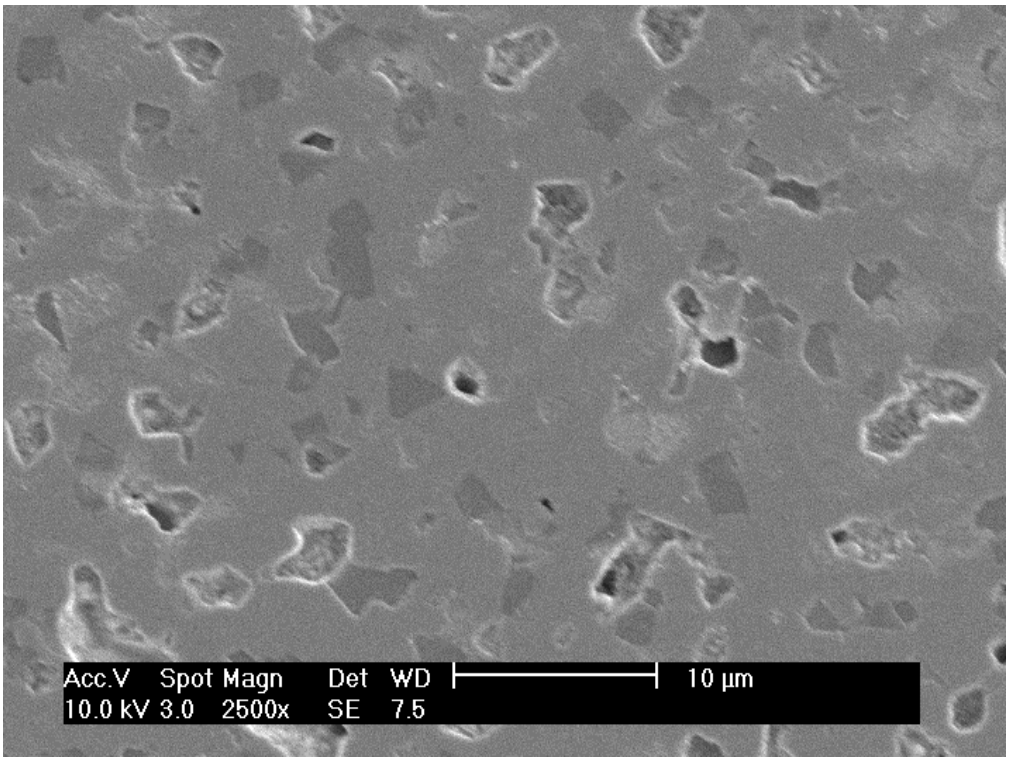

Figure 2.13: 95% NiO-5% $SrTiO_3$ (large grains) at 2500x magnification, optically polished surface.

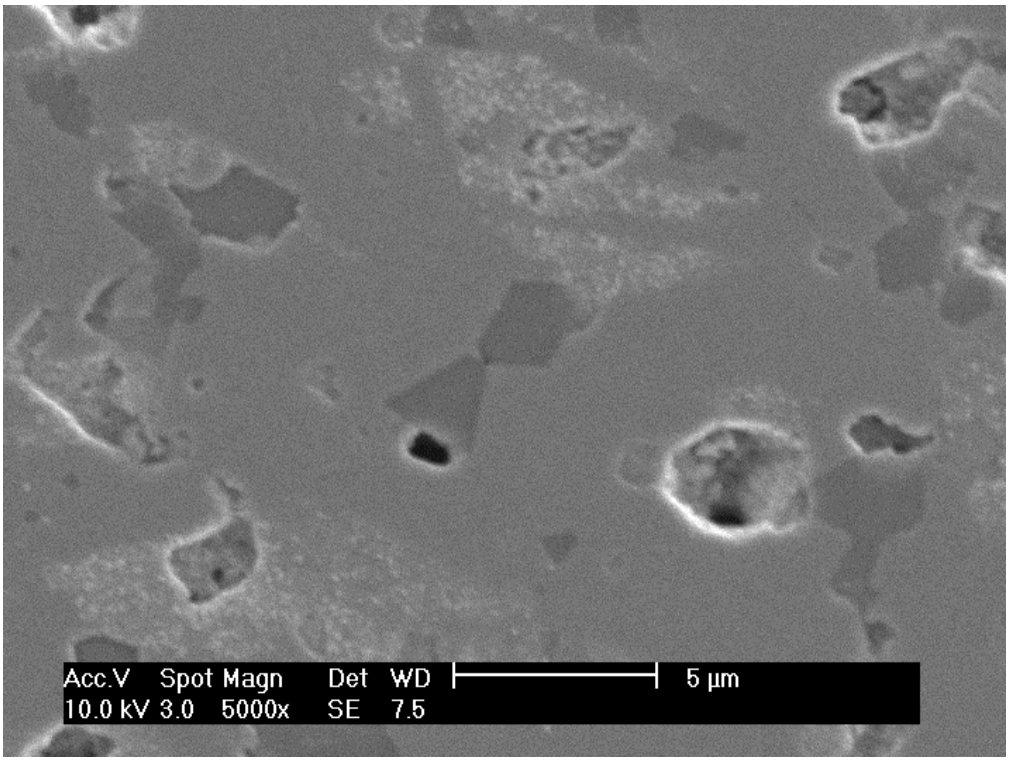

Figure 2.14: 95% NiO-5% $SrTiO_3$ (large grains) at 5000x magnification, optically polished surface.

CHAPTER III

GaP based terahertz time-domain spectrometer optimized for the 5-8 THz range

3.1 Introduction

In this chapter we present a technique of using GaP to generate terahertz pulses via optical rectification in a collinear phase-matched configuration relying on the dispersion of the refractive index. The GaP-based time-domain system operates up to 8 THz and is especially well suited at high frequencies, where it has high signal-to-noise ratio and power conversion efficiency ~ 30 times greater than those of commercial photoconductive emitters. These characteristics are demonstrated in measurements of ZnTe in the reflection geometry. We also discuss the power output and describe theoretically the observed THz field generation by nonlinear mixing, the field's free space propagation and its detection.

3.2 Motivation

Terahertz time-domain spectroscopy (THz-TDS) has become a popular tool for materials research. [1] Its popularity stems from the widespread availability of Ti: sapphire lasers with which a THz time domain emitter and detector pair can be coupled. The convenience of this approach, its high signal-to-noise ratio (SNR) and

ability to measure the time evolution of the field have made it competitive with conventional FTIR techniques. [2] Unfortunately, one of the main drawbacks of THz-TDS is that the spectral response is typically limited to frequencies below 6 THz. [3, 4] This leaves many interesting phenomena at higher frequencies out of reach. In spectroscopic studies there is often a minimum dynamic range requirement for overcoming losses, which decreases the usable bandwidth further [5] and renders some thin generator/detector layer wideband approaches untenable. [48]

In the past several years, a few methods have been shown to be effective in tackling this problem. These include photoconductive (PC) systems based on low-temperature GaAs, driven by 15 fs Ti:sapphire oscillators, [49] four-wave mixing in self-induced plasma driven by amplified kHz systems [50] and phase-matched nonlinear generation using GaSe, [51] the organic crystal DAST [52] and other electro-optic (EO) materials. [45] However, these approaches are not in widespread use due to the added cost of special laser systems (e.g., having 15 fs pulse width or additional laser amplifiers), the difficulty in working with organics and procuring properly grown PC materials [53] or the presence of gaps in the generated spectrum. As a result, spectroscopic measurements using THz-TDS in the 5-10 THz range and above are still hard to achieve.

3.3 Conceptual idea and data

Here we present a THz-TDS system based on optical rectification in GaP driven by a 50 fs Ti:sapphire laser oscillator. The dispersion of the refractive index due to the infrared-active phonon in GaP allows for collinear phase matching over a wide frequency range, from 0.5 to 8 THz. [54, 55] Free-space EO sampling [45] is used in a second crystal of GaP for detecting the field-resolved signal generated by the emitter. The phase matching condition in collinear processes involving the nonlinear susceptibility $\chi^{(2)}$, where a THz wave interacts with two waves within the bandwidth

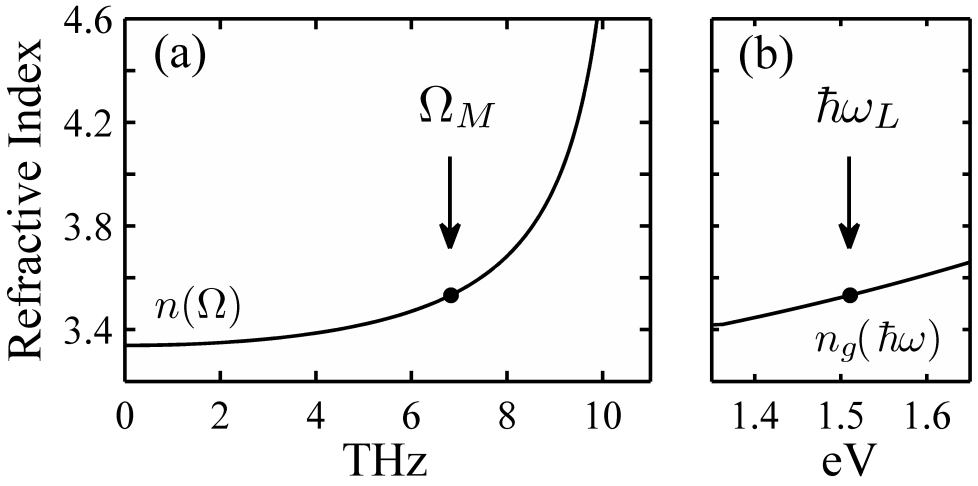

Figure 3.1: Refractive index of GaP in (a) the THz regime and (b) group index in the near-infrared.

of an ultrafast optical pulse, is $n_g \approx n_{THz}$, where n_{THz} is the THz refractive index and n_g is the group index in the visible. [54, 55, 56] The behavior of the permittivity of GaP below 10 THz is defined by the coupling to the transverse optical mode at 11 THz. Fig. 3.1 shows the refractive index of GaP below the phonon resonance and in the range $\hbar\omega_L$ =1.35-1.65 eV (920-750 nm) corresponding to the Ti:sapphire laser [57]. As illustrated in the figure, for a given excitation frequency ω_L, phase matching is exactly met at the frequency Ω_M in the THz range. Moreover, since the coherence length $L_c = \pi c/(\Omega_{THz}|n_g - n_{THz}|)$ [56] is at least several hundred microns within the band, phase matching in GaP is nearly satisfied over the entire range, up to 8 THz. This, combined with a high nonlinear coefficient [4] and transparency at visible wavelengths, lays the groundwork for attaining significant power conversion efficiencies.

The laser system we employed is a mode-locked Ti:sapphire oscillator producing 800 mW of average power at the repetition rate of 82 MHz. The beam is split into separate pump and probe pulse trains and a delay stage is used for mapping the subpicosecond time evolution of the THz pulses. At the point of generation, a 400-μm-

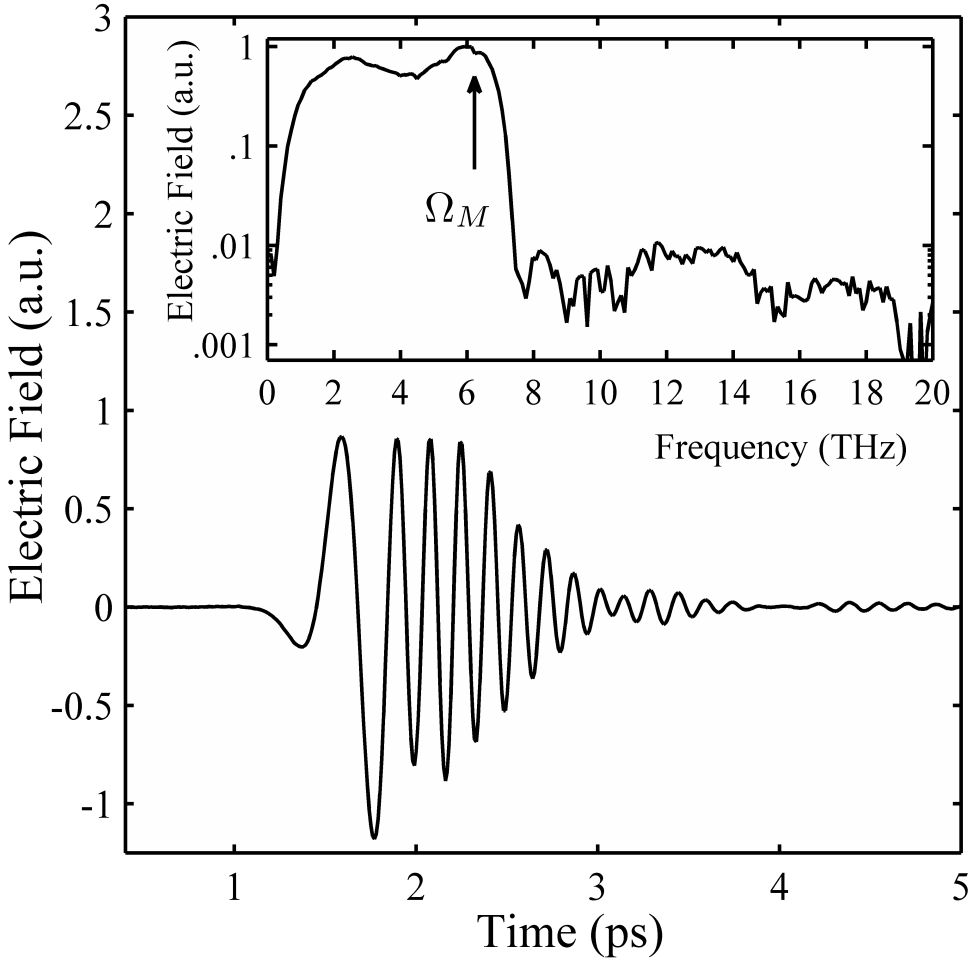

Figure 3.2: Temporal signal and associated amplitude spectrum for GaP generation (400 μm thick crystal) and EO detection (340 μm thick crystal) using 60-fs laser pulses.

thick single-crystal semi-insulating (110) GaP slab (MTI Corp.) is illuminated with 60 fs pulses in a beam initially having average powers up to 370 mW before being reduced to half this value due to modulation by an optical chopper. The THz pulses are generated in the transmission geometry by difference-frequency mixing of the near-IR beam with itself. The pump beam is focused to a 45-μm-diameter spot onto the GaP sample, and THz radiation is collected and focused onto the sample or the reference reflector by two parabolic mirrors, the first of which is $f/1$, which allows collection at a wide emission angle. A second set of parabolic mirrors is used to re-image the THz beam from the sample/reference position onto the detection crystal. The entire THz beam path is enclosed and purged with dry nitrogen to avoid water-vapor absorption. We employed EO detection for probing the THz pulses using a second 340-μm-thick, (110) GaP slab and 20 mW of incident probe power. A commercial dual-diode photodetector (Nirvana, New Focus Inc.) with an auto-balancing feature was used to help avoid drift between channels over extended scanning times as it detects the orthogonal polarizations transmitted through the GaP EO-sensing crystal. The probe power reaching each channel was 1.4 mW, after being cut-down with irises for eliminating noise, which yields an optimal, near shot-noise-limited signal that was recorded using a lock-in amplifier.

A typical time-domain signal and the associated frequency spectrum are shown in Fig. 3.2, where three scans acquired using a 300-ms time constant were averaged. The frequency response corresponding to $\hbar\omega_L = 1.51$ eV shows a peak at $\Omega_M = 6.2$ THz and, noticeably, it extends to 7.5 THz. The dynamic range is 2000:1 in time-domain and 400:1 in frequency domain at 6-7 THz, [58] where the response of typical systems tails off. This is one of the highest signals reported in this frequency range. For our conditions, the shot noise limit set by the photodetector is 2.2 $\mu\text{V}/\sqrt{\text{Hz}}$ and the measured noise is 3.1 $\mu\text{V}/\sqrt{\text{Hz}}$, which is 40% above the shot noise floor. Some prominent features in Fig. 3.2 include chirp and a discernible beating in the time

domain. The frequency spectrum is oscillatory and fades at 8 THz.

3.4 Simulation

To interpret the data we must consider THz emission, free space propagation from the emitter to the detector, and EO sampling response in a single framework. Difference frequency generation in a slab of nonlinear material has been treated by Côté et al. [46] taking into account the spot dependence of the optical beam. The problem amounts to adding up the emitted THz field from every point along the length of the crystal due to the pump-induced nonlinear polarization source, which propagates in the $\hat{z}$ direction. At a given z, its spatial Fourier transform can be expressed as $\mathbf{P}^{NL}(\Omega, \mathbf{K}) = \hat{x} 2\epsilon_0 \chi^{(2)}(\Omega) I_f(\Omega) I_s(K) \exp(ik_0 n_g z - 2\alpha z)$, where Ω is the THz frequency, $k_0 = \Omega/c = 2\pi/\lambda_{THz}$, α is the field absorption coefficient of the optical pulse, $I_s(K) = \exp(-K^2\sigma_0^2/4)$ is the K-space intensity profile of the beam (normalized so that the total power is independent of the spot size), and $I_f(\Omega) = I_0\sqrt{\pi}\tau_0 \exp(-\Omega^2\tau_0^2/4)$ is the optical intensity envelope. The spot size σ_0 and pulse duration τ_0 are the 1/e half-widths. Let $E(\Omega, \mathbf{R}) = \int \frac{d\mathbf{K}}{(2\pi)^2} E(\Omega, \mathbf{K}) \exp(i\mathbf{K} \cdot \mathbf{R})$ be the $\hat{x}$-polarized THz electric field at the slab exit ($z = d$), where $\mathbf{R} = (x, y)$ and d is the thickness of the slab. Following Ref. 46, its Fourier transform is

$$E(\Omega, \mathbf{K}) = T(\Omega, \mathbf{K}) \frac{ik_0^2}{w(K)} \frac{\exp(ik_0 n_g d - 2\alpha d) - \exp[iw(K)d]}{[ik_0 n_g - 2\alpha - iw(K)]} \chi^{(2)}(\Omega) I_f(\Omega) I_s(K) \tag{3.1}$$

where $w(K) = \sqrt{(k_0 n_{THz})^2 - K^2}$ and $T(\Omega, \mathbf{K})$ is a linear combination of s- and p-polarization transmission coefficients at the exit interface. Eq. 3.1 is a simplified version of the full solution, [46] which excludes the backward propagating wave (of a much smaller amplitude) and multiple reflections, which we avoid by using a short temporal window.

We model the pulse propagation by considering a single lens that collects the emit-

ted radiation and refocuses it onto the EO sampling crystal. It is known from Abbe's theory of imaging that the limited aperture of the lens serves as a low-pass spatial frequency filter, with the cut-off in the paraxial approximation, ignoring aberrations, given by $K_c = k_0 \tan\theta$, where θ is the collection half angle of the first lens ($f/1$, 25.4 mm diameter, $\theta = 26.6°$). [46, 59] Thus, the THz field in the detection crystal is a magnified replica of the emitted field, which has passed through a low-pass filter. The THz field is detected on the optical axis yielding

$$E_{meas}(\Omega) = \frac{f(\Omega)}{M} \int_0^{2\pi} d\varphi \int_0^{K_c} \frac{K dK}{(2\pi)^2} E(\Omega, \mathbf{K}), \tag{3.2}$$

where M is the magnification and $f(\Omega)$ is the EO sampling response based on Eq. 62 of Ref. 47.

For a qualitative understanding, we can consider the dominant axial component of the solution, $E(\Omega, 0)$, which is represented by two pulses–propagating with velocities c/n_g and c/n_{THz}. For a fixed crystal length, the two pulses become mismatched in a time $\tau = (n_{THz} - n_g)d/c \sim 210 - 230$ fs. This causes modulation in frequency away from Ω_M with a dip at 4.5 THz reflecting the greatest phase mismatch. Due to the monotonically increasing n_{THz} we observe chirp, which is experienced by one of the two pulses contributing to the solution. The detection mechanism has a similar phase matching response thereby enhancing the frequency oscillations. Finally, it is important to account for the dispersive nature of $\chi^{(2)}(\Omega)$ for GaP which significantly modifies the frequency spectrum due to its resonant minimum at 8 THz, [60] which is responsible for the upper bandwidth limit in our data. For a fixed optical power, it is possible to enhance $E_{meas}(\Omega)$ by tighter pump focusing until $\sigma_0 \sim \lambda_{THz}$ after which point the signal saturates due to internal and aperture diffraction. [61] This allows for a significant enhancement of the higher frequencies of the spectrum for which the saturation transition occurs for smaller σ_0. In Fig. 3.3 we compare the measured

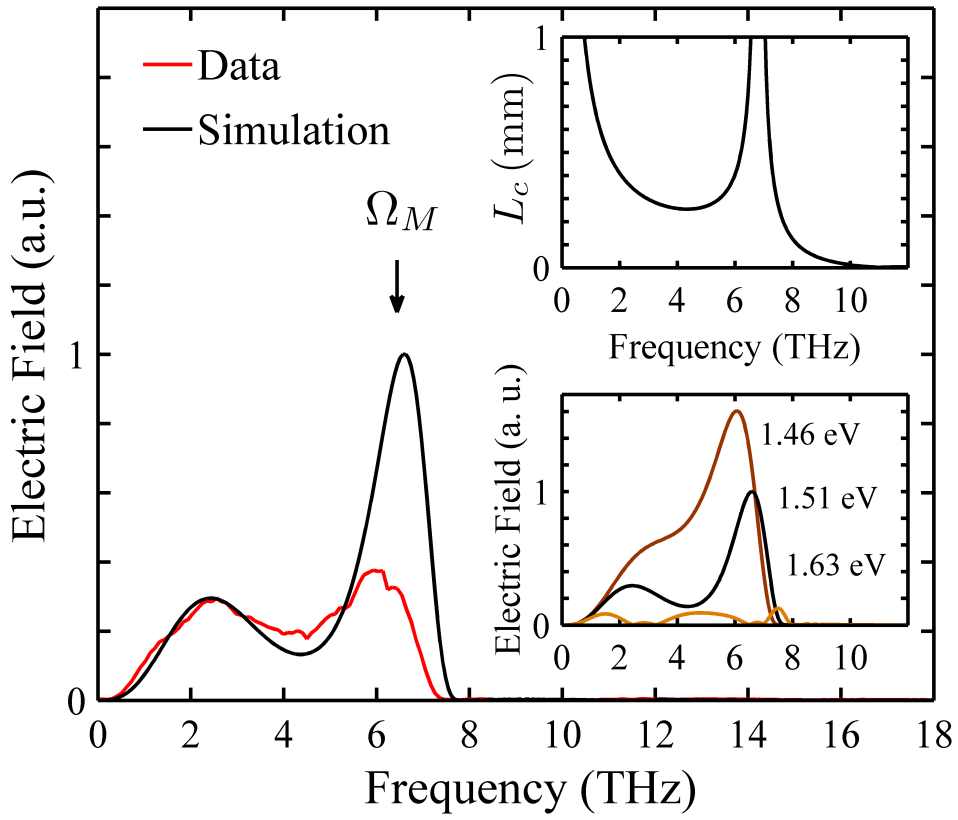

Figure 3.3: Simulation of THz generation, mirror aperture diffraction, and EO sampling. The simulation parameters were $\hbar\omega_L = 1.51$ eV, $\sigma_0 = 20$ μm, $\tau_0 = 65$ fs, $d = 400$ μm, and a 340-μm-thick detection crystal. Top inset: Coherence length. Bottom inset: Simulation as a function of excitation energy, $\hbar\omega_L$.

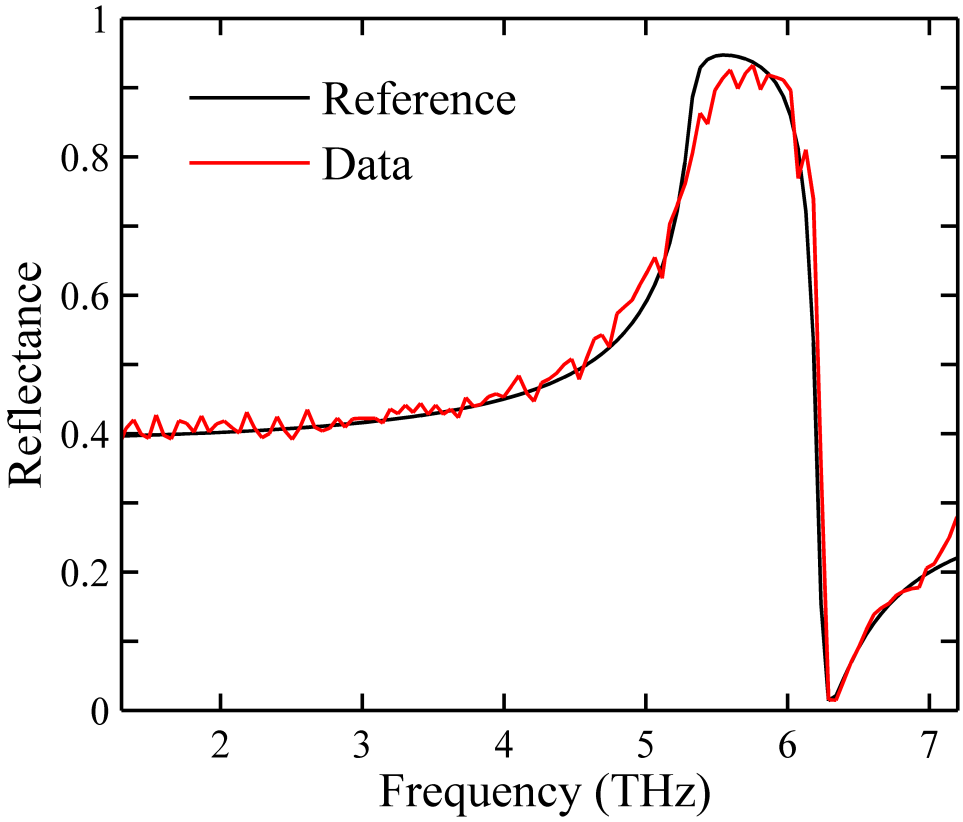

Figure 3.4: Reflectance of ZnTe (45° angle of incidence, *s*-polarization) compared with calculations using harmonic oscillator parameters from Refs. 62 and 63.

signal with the simulation based on Eq. 3.2 using experimental parameters. The peak at 6.2 THz is lower than that predicted by the simulation, which could be due to imaging errors (e.g., aberrations, misalignment) or the presence of other nonlinear effects. In the insets, we include the dependence of the signal on the excitation energy, $\hbar\omega_L$, which provides some bandwidth tunability, and the coherence length function L_c, which is a good predictor of the signal profile for a fixed crystal thickness.

3.5 Evaluation of performance

To test our system, we performed first a spectroscopic measurement on ZnTe at room temperature. The reflectance, together with calculations based on a harmonic-

oscillator fit to the experimental data, [62] are shown in Fig. 3.4. The value for the linewidth $\gamma/2\pi = 0.032$ THz was taken from Ref. 63. The main feature in the reflectance is due to the reststrahlen band, with the TO-phonon at 5.3 THz. The oscillations in the data below 6 THz are not random noise, but are caused mainly by multiple reflections within the emitter/detector crystals. These can be avoided either by using a shorter time window (at the expense of resolution) or by matching the emitter/detector to a substrate that would delay reflections. In addition, we note that the most prominent water vapor lines are also visible in the experimental data (e. g., 4.52, 5.1, 6.08, 6.25, 6.84 THz). [64] The available bandwidth and high SNR allows reflectance measurements up to 7.2 THz, in good agreement with previous work.

As a second test, we compared our system's signal to that of a PC emitter under similar conditions. Here, we used a commercial device (TeraSED3, GigaOptics, GmbH) designed for high bandwidth and high average power performance, with a rated output of 54 μW at optimal conditions. [42, 65] This particular structure employs an interdigitated array pattern fabricated on semi-insulting GaAs with a spacing of 5 μm between electrodes. A bias field of 30 KV/cm was applied and the excitation laser beam was focused to a 90-μm-diameter spot. The emitted radiation was collected in the backward geometry (from the front, illuminated face of the PC emitter) in order to minimize losses in the GaAs substrate. This yields a greater than two times emitted-field improvement above 5 THz. The incident power used for both methods was 250 mW before chopping. There was a $\sim$ 10% difference in the THz spot size on the detector between the two generation methods, due to different optics that were employed, and for which the data was corrected. The amplitude spectra for identical detection conditions are plotted in Fig. 3.5. The power from the TeraSED was measured at 2 μW using EO sampling in a 50-μm-thick (110) ZnTe plate. Based on a previous pyroelectric detector measurement, [42] the power for our conditions

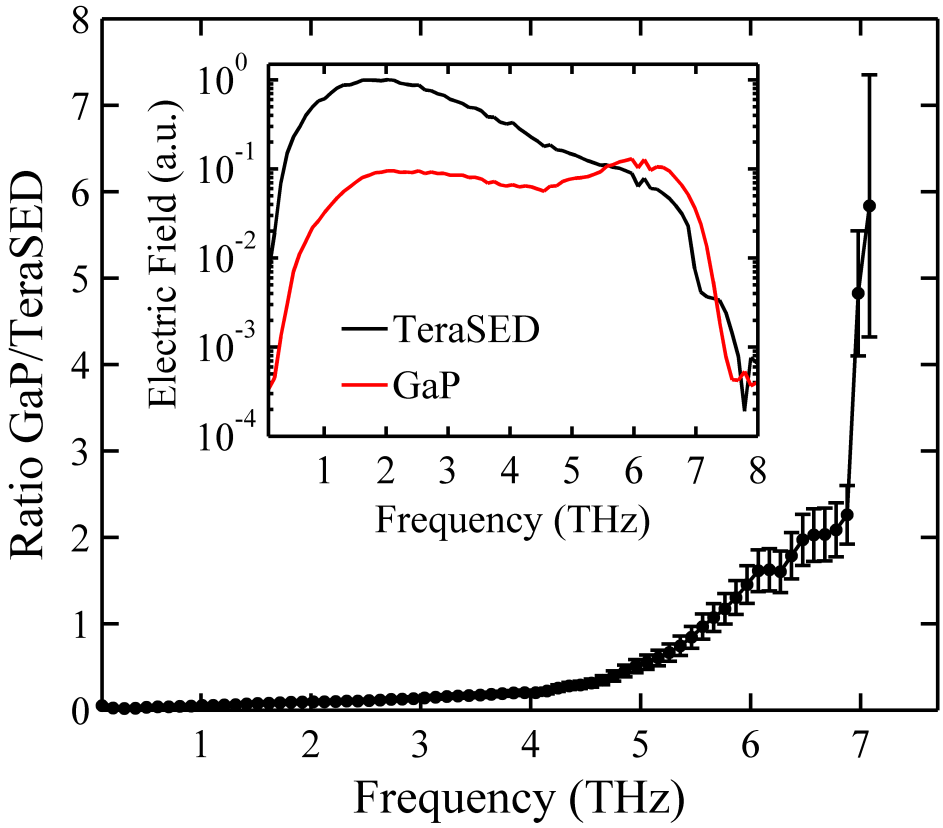

Figure 3.5: Ratio of GaP to TeraSED signals as a function of frequency. Inset: Uncorrected amplitude spectra, as measured in the EO detector.

is 4 μW. This gives for GaP a power estimate of 0.2 μW, obtained by integrating $|E_{GaP}(\Omega)|^2$ and $|E_{TeraSED}(\Omega)|^2$, after correcting for the response of the 340 μm GaP detector. Even though the total GaP power is $\sim$ 7% that of the TeraSED emitter, the efficiency of the former improves considerably at high frequencies. Specifically, the GaP source has a higher signal above 5.5 THz, and the field is 5.5 times higher at 7 THz, yielding a factor of 30 improvement to power conversion efficiency. It is worth noting that the amplitudes shown in the inset of Fig. 3.5 are fields modified by the response of the detector, whereas the ratio of the two is quite accurate due to similar experimental conditions. The signal merges with the noise at $\sim$ 7.5 THz due to the vanishing $\chi^{(2)}(\Omega)$ for GaP and TO-phonon absorption for GaAs, [65, 49] both occurring at 8 THz. The GaP-to-TeraSED ratio in the main plot is shown up to 7.1 THz, beyond which point the uncertainty becomes significant. Simulations show that the ratio can be made even higher by using thicker GaP or by tuning $\hbar\omega_L$. More importantly, PC generation operates near its threshold in terms of peak excitation power, bias field and dissipation. On the other hand, the power output from GaP is expected to scale with excitation power, and GaP has been applied successfully to this end in fiber laser systems possessing up to 14 W of pump power. [66] The THz power can be scaled up by increasing either the incident pump intensity or the active area of the generation crystal at a fixed pump intensity. The more efficient former case leads to a quadratic increase in the THz power, [67] but is limited by the multi-photon saturation threshold of the nonlinear medium. Using the available power and tighter focusing, we were able to increase the peak pump intensity by a factor of $\sim$ 20 from the above experimental value. We find a sub-quadratic increase in the THz pulse energy with an average exponent of 1.54 in the pump peak intensity range of 10 to 200 GW/cm^2 (fluence of 0.3 to 6.5 mJ/cm^2). Based on these values, we estimate an output from GaP of 20 μW for a pump power of 5 W for otherwise identical conditions. Further increase in intensity may be limited by the damage

threshold of the crystal. Under similar operational conditions, the latter has been measured to be 4.3 mJ/cm^2. [68]

3.6 Summary

In summary, we have shown that GaP-based generation and detection of THz pulses can be used as a THz-TDS spectrometer optimized for high frequency operation, in the 5-8 THz range. We anticipate this system to be useful with 50 fs Ti:sapphire oscillator lasers as well as for scaling to higher peak and average powers.

CHAPTER IV

Nickel Oxide–Strontium Titanate Ceramics

4.1 Introduction

This chapter focuses on the NiO-$SrTiO_3$ ceramics made of sintered nano-to-micron sized grains of each constituent. The original motivation for this research was to investigate the feasibility of constructing a bulk metamaterial NIM in the THz range. As is known from Veselago's famous paper [1], a negative index material must have $\mathrm{Re}\{\epsilon\}$, $\mathrm{Re}\{\mu\} < 0$ over some frequency range and unfortunately there are no known natural substances that satisfy this property, although there is no fundamental reason to make this impossible. However, there are many substances that possess magnetic and electric behavior individually which induce regions of either negative permittivity or negative permeability–such as for example in metals below the plasma frequency for the electric case and ferromagnets in the magnetic case. Most approaches to develop NIMs have focused on using artificial materials (meta-materials) composed of arrays of metallic structures engineered to have sharp magnetic and electric responses in the same frequency range in order to make $n < 0$ [14]. The first and best known such structure was an array of split ring resonators (SRRs) and metal wires, which was experimentally verified to possess negative refractive index in the microwave region [18]. The SRRs provided the magnetic resonance to drive effective permeability negative, whereas the metal wires provided the negative electric permittivity. How-

ever, this metamaterial operated at low frequencies and was not a true bulk structure, due to the finite number of layers in the design. In order to improve its operation it is important to reduce it to nanometer dimensions in order to operate at visible frequencies which has proved challenging, but doable for 2D structures. [19] However, the design of 3D metamaterials at either terahertz or visible frequencies has proved even more challenging due to the existing limitations in the fabrication methods. For this reason, the interests of various researchers are shifting toward alternative approaches of designing and controlling 3D structures such as nanoparticle self-assembly and improvements to conventional lithographic techniques. [10] Another important requirement in this context is to understand the complex optical behavior in random, truly 3D metamaterials which are typically based on plasmonic properties.

The individual constituents that make up the composite in this project are known to possess electric and magnetic resonances in the far-infrared frequency range and the simple idea proposed previously [23] was to obtain a homogeneous random medium that would possess the combined properties of both constituents. Thus if the interactions were turned off and simple volume averaging of bulk properties applied, this composite would possess negative refractive index. Based on our measurements using THz-TDS and FTIR spectroscopy, the interaction picture turned out to be more complicated with the spectral features being dominated by surface phonon-polaritons of the nano-sized STO inclusions which define the dielectric behavior. The magnetic resonance of the NiO was also measured in the composite and was found to have an effect in a very narrow frequency region–a small fraction of one wavenumber–such that a precise determination of the magnetic permeability presents technical challenges in itself. Thus our attention has shifted mainly to understanding the dielectric properties of the composites, on which this chapter is focused. The ability to control the effective dielectric properties through the geometry of the STO inclusions is critical for designing a successful bulk NIM using the ceramic approach. The observation of

single-particle dipolar surface-plasmon resonance (Fröhlich mode) as will be shown for the present composite makes it possible to achieve controlled resonances in the effective dielectric constant which is an important step forward. The second half of the job is to obtain the desired magnetic behavior, and it will be shown that NiO behaves nearly as a bulk material in the composite due to the fact that it is present at large volume fractions. Based on transmission measurements, we show that the oscillator strength of the AFMR of NiO as measured at room temperature is not likely to produce negative permeability, with the critical factor being the temperature dependent linewidth of the magnetic resonance. However, other antiferromagnets with more pronounced magnetic-dipole active resonances may be used in place of NiO as will be discussed in the concluding chapter.

In what follows we will describe the resonant behavior of the individual constituent materials and how they are formed into composites which has been described in greater detail in the experimental section. This will be followed by the reflectance and transmission data taken with THz-TDS and FTIR techniques, for several classes of ceramics involving different sizes of particles. The data will be interpreted within the context of several effective medium theories. The Clausius-Mosotti equation forms the framework for going from the characteristics of individual, finite sized ionic scatterers to forming an effective medium which is dominated by individual effects at low filling fractions. The appearance of dominant low frequency and high frequency modes leads to the interpretation of two distinct inclusion sizes–one being due to individual STO particles and a larger effective mean size for clusters of STO particles. The clusters are treated as single unit, larger particles and interactions between particles is accounted for through the local field of the Clausius-Mosotti approach. The variation of shape and size in the agglomerate clusters is treated as a distribution of ellipsoids. Finally, the dependence of the surface modes on the size of the inclusion is discussed and related to the data.

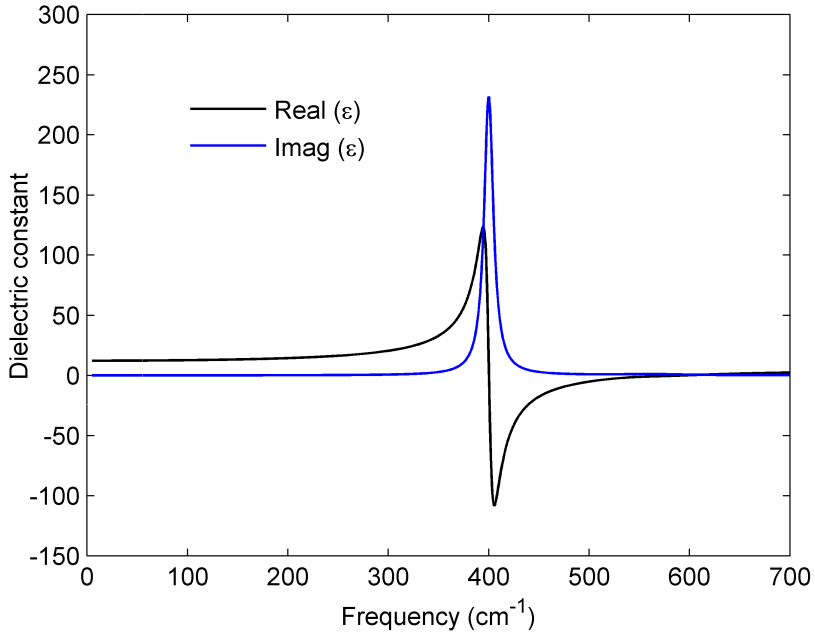

Figure 4.1: Real and imaginary part of the electric permittivity of Nickel Oxide in the far-infrared range at room temperature.

4.2 Nickel Oxide

Nickel Oxide, which in micro- and nano-particle form is one of the two constituents, is an antiferromagnetic insulator with a transition temperature of $T_N = 522$ K [69]. Above the Néel temperature, NiO crystallizes in a cubic, rock-salt (NaCl) crystal structure with two atoms per primitive unit-cell [70, 71]. Below the Néel temperature, the antiferromagnetic ordering does not significantly distort the structure to have an effect on the vibrational properties and thus the crystal is considered of quasi-NaCl type. The dielectric properties are determined by the infrared-active, triply degenerate optical mode at 400 cm^{-1}. The optical constants have been measured at room temperature in the spectral region from 250 cm^{-1} to 3000 cm^{-1} and a two-oscillator model has been found to give the best fit [71]. The real and imaginary parts of the electric permittivity are shown in Fig. 4.1.

In order to confirm the purity of the NiO nanoparticles, we measured Raman scattering with the 5145-Å line of an Argon-ion laser serving as the exciting source.

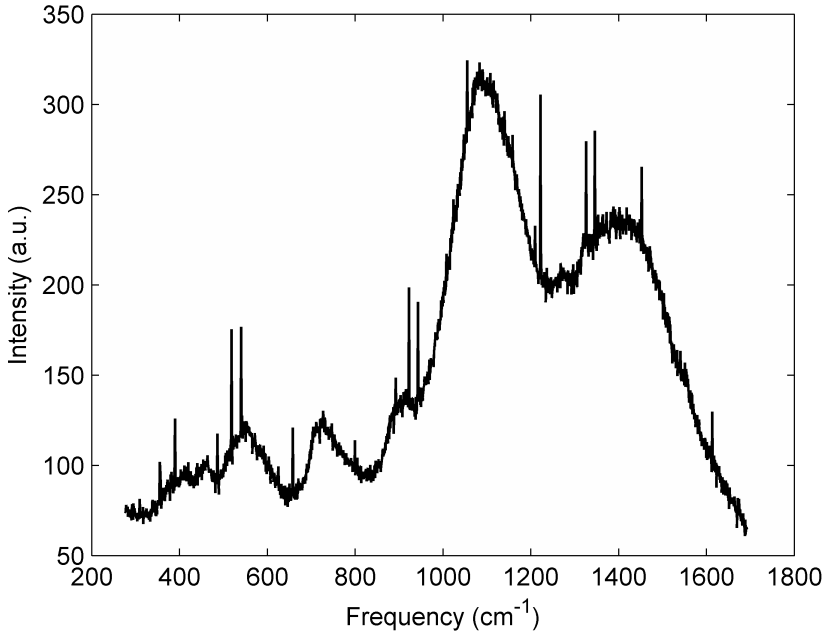

Figure 4.2: Raman spectrum of NiO powder (-325 mesh) taken at room temperature. The incident power is 10 mW at 5145-Å.

The results agree closely with the data available in the literature [72] and are shown in Fig. 4.2.

Due to its magnetic properties, NiO also possesses a magnetic-dipole active antiferromagnetic resonance (AFMR) in the THz range which is temperature dependent and occurs at approximately 1 THz [73]. The transmission of nano- and large-grained ceramics was measured using THz-TDS as shown in Fig. 4.3, with the behavior matching quite well with previous studies. The resolution of this particular measurement was $\sim$1 cm^{-1} as determined by the length of the temporal window of the scan. Other measurements with improved resolution show significant narrowing of the linewidth to less than 0.5 cm^{-1} at T = 50 K. Based on these measurements, the $\mu(\omega)$ at room temperature is shown in Fig. 4.4 with the linewidth FWHM of 1.2 cm^{-1}. At low temperatures only an upper bound on the linewidth is known and thus the low temperature value of $\mu(\omega)$ is indeterminate although it is expected that it would show significant enhancement due to the narrowing. In principle, THz-TDS is

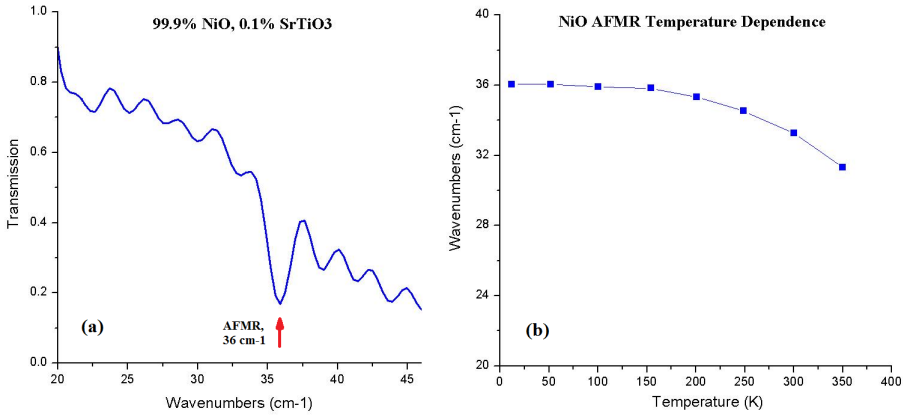

Figure 4.3: Transmission of the large grain NiO ceramic taken at (a) T = 50 K showing the AFMR and (b) showing the temperature dependence.

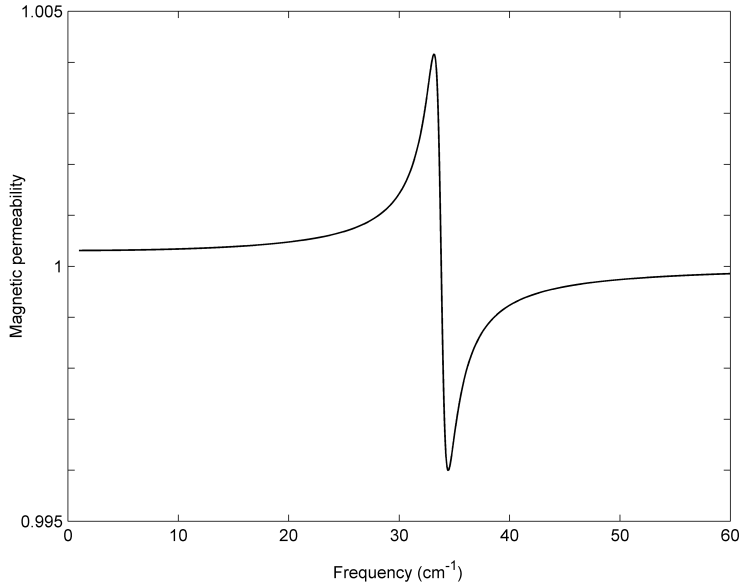

Figure 4.4: An oscillator fit of the magnetic permeability of ceramic NiO (1.85 mm thickness) based on transmission measurement at T = 300 K.

well positioned to do a high resolution measurement with precision of less than 0.1 cm^{-1} for temporal scans of 400 ps. This is an interesting future research direction as it would complement the far-infrared measurements available currently in the literature all of which are inconclusive due limitations in the resolution [73]. Since the magnetic behavior occurs in a very narrow frequency range, the location of which is known, we will assume in what follows that $\mu = 1$ and concentrate on the dielectric properties.

4.3 Strontium Titanate

Strontium Titanate (STO) is a ferroelectric crystal (of ABO_3 type) with a cubic perovskite structure above 110 K which renders it optically isotropic. It has five atoms per unit cell leading to four triply degenerate optical modes, three of which are infrared active [74]. The signature behavior of such ferroelectrics is the high value of electric permittivity which depends on temperature according to the Curie-Weiss law [75, Ch. 13],

$$\epsilon_0 \propto 1/(T - T_C) \tag{4.1}$$

where ϵ_0 is the static dielectric constant. The extrapolated Curie temperature is $T_C \simeq 40$ K although STO is an incipient ferroelectric which means that it never actually undergoes a ferroelectric transition and the Curie-Weiss dependence only applies for $T > 50$ K [76]. In close connection to the Curie-Weiss law is the temperature dependent behavior of the lowest frequency vibrational mode known as the "soft mode" which decreases in frequency as the temperature is lowered. In ideal circumstances, the ferroelectric transition occurs at the Curie point temperature when the soft mode frequency vanishes and the resulting lack of restoring force on the lattice leads to a displacement of the ions and the creation of a permanent dipole moment within the

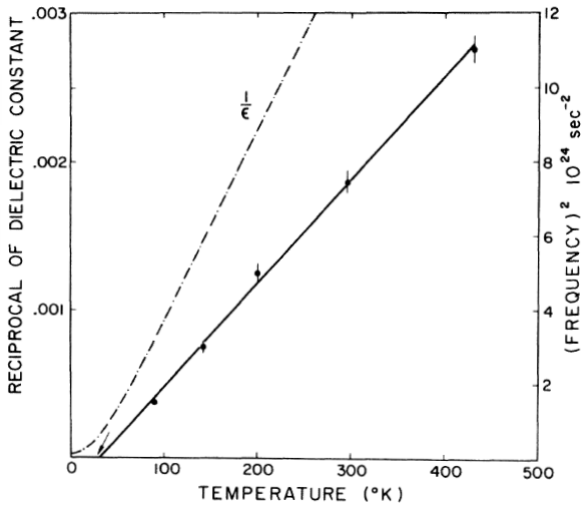

Figure 4.5: The figure shows a plot of the square of the frequency of the zone-center transverse optic mode against temperature. The solid line is a linear regression line through the points and gives a Curie temperature of 32±5 K. The other line represents the reciprocal of the dielectric constant. Taken from [77].

unit cell. The temperature dependence of the low frequency mode follows [77],

$$\omega_{TO1} \propto (T - T_C) \tag{4.2}$$

where ω_{TO1} is the lowest frequency transverse optical phonon. The connection between Eqs. 4.1 and 4.2 is established through the Lyddane-Sachs-Teller relation, assuming that the higher frequency modes do not depend significantly on temperature. We show temperature dependence of the soft mode in $SrTiO_3$ in Fig. 4.5.

The real and imaginary parts of the dielectric constant have been measured at low temperatures [78] and are shown in Fig 4.6 for two temperature points. As seen from the figure, the values of the dielectric constant on resonance reach tens of thousands which is two orders of magnitude above the typical values in ionic dielectrics as seen, for example, in Fig 4.1 for Nickel Oxide. No magnetic behavior is known for $SrTiO_3$ and so the magnetic permeability is taken as $\mu = 1$. The purity of the constituent material was once again confirmed using Raman scattering measurements. A typical

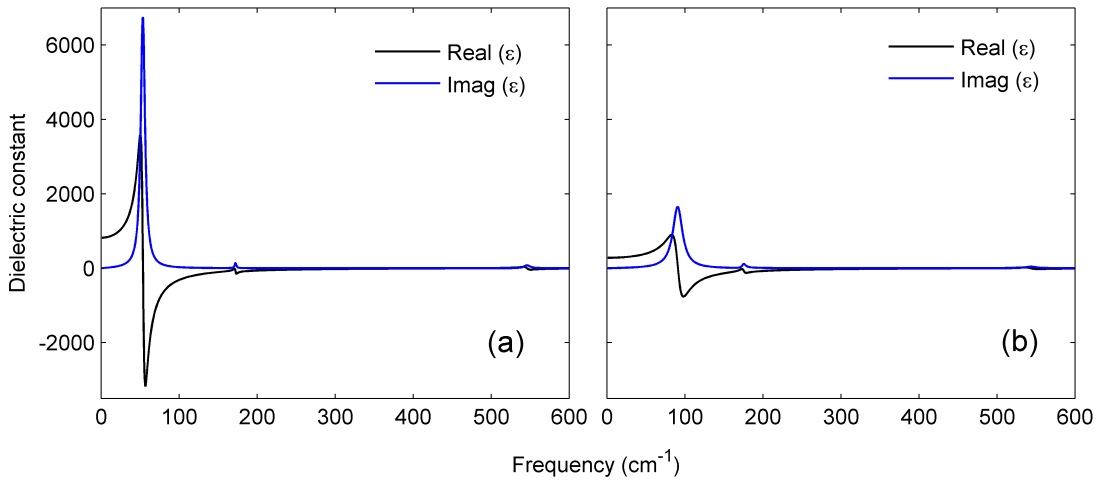

Figure 4.6: The real and imaginary parts of the dielectric constant of $SrTiO_3$ for (a) $T = 130$ K and (b) $T = 300$ K.

fingerprint spectrum which agrees with previous data in the literature [74] is shown in Fig. 4.7. The Raman scattering was taken with 5145-Å argon-ion laser line.

It is worth noting that the above properties have been described for bulk $SrTiO_3$, whereas in the composite $SrTiO_3$ will be present in localized, nano-particle form as inclusions. Thus the phonon-polariton modes of the bulk will be transformed into vibrational modes of finite crystals as will be discussed in the following sections.

4.4 Ceramics

The above constituents are mixed in powder form in desired proportions where $SrTiO_3$ serves as the inclusion and makes up a small fraction of the total, from 0 to 15% by volume. The mixed powder is ball milled for 24 hours in order to minimize clustering and achieve uniform mixing. The fabrication of ceramics is achieved by cold pressing the mixture into 1-2 cm discs and sintering at 1400 °C. A scanning electron microscope image of a 95% NiO-5% $SrTiO_3$ (95-5) sample is shown in Fig. 4.8, where the larger particles are NiO grains and the smaller ones are $SrTiO_3$. One can see a number of well separated $SrTiO_3$ inclusions as well as clusters of $SrTiO_3$

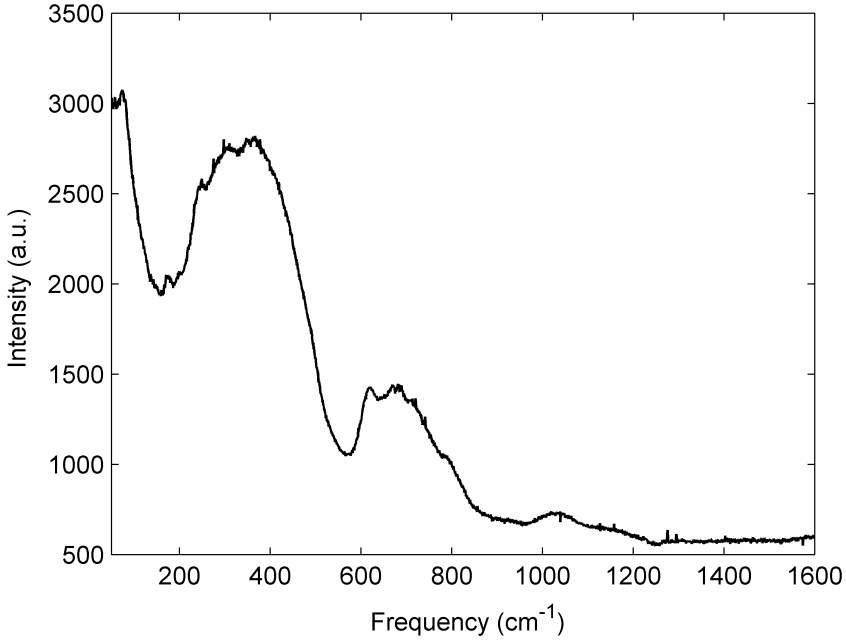

Figure 4.7: Raman spectrum of $SrTiO_3$ powder taken at room temperature. The incident power is 19 mW at 5145-Å.

that tend to form larger aggregates of varying geometries.

Raman data was taken on a 50-50 ceramic composite in which the features of STO and NiO are seen (Fig. 4.9) as superimposed on each other.

Three different types of composites were fabricated involving the nano-sized and micron-sized variations of the constituent grains. The particle sizes for NiO were nearly spherical ∼800 nm diameter for the regular size grains and less than 100 nm diameter for the nano particles. For the Nickel Oxide, the standard grains were on the order of 5 μm and less than 50 nm for the nano-particles. The three different types of ceramic samples were: nano-NiO/STO, nano-NiO/nano-STO, NiO/STO. In all samples, STO was present in small concentrations as the inclusion. The different grain sizes were used to evaluate the effect on inclusion clustering and correlations in the case when the large NiO particles tended to form channels for the smaller inclusion grains. These aspects will be discussed later in detail in the context of infrared data analysis and effective medium theories.

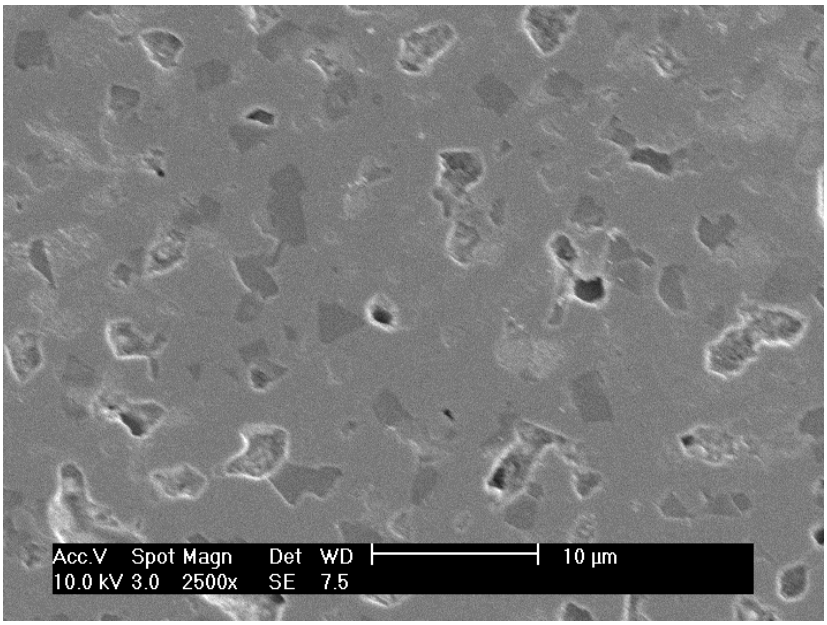

Figure 4.8: SEM image of a 95% NiO-5% $SrTiO_3$ ceramic composite with an optically polished surface. The starting NiO is -325 mesh and the starting $SrTiO_3$ is ∼800 nm diameter.

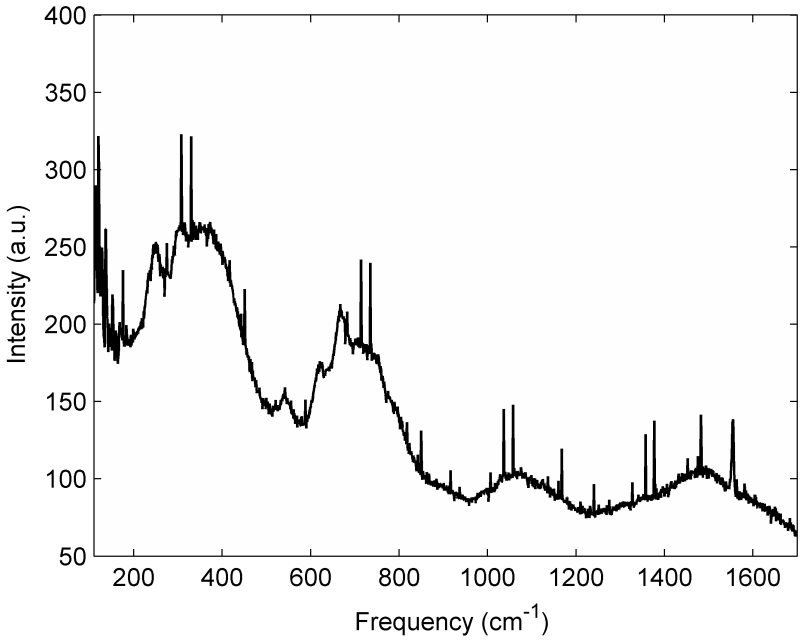

Figure 4.9: Raman spectrum of 50% NiO-50% $SrTiO_3$ composite ceramic. The incident power is 40 mW at 5145-Å.

4.4.1 Simple model for the effective optical constants

Our composite is a randomly distributed mixture of two phases with dielectric constants ϵ_i, μ_i representing the STO inclusion and ϵ_h, μ_h representing the NiO host. As discussed above we will assume that $\mu_i = \mu_h = 1$ so that the magnetic properties need not be considered. If we assume that the the scale over which $\epsilon(\mathbf{r})$ varies is small compared to the wavelength of light then we can say that the effective parameter ϵ_{eff} exists which describes the composite medium. As a first order approximation, we can take the effective dielectric constant to be the weighted average of the constituent phases,

$$\epsilon_{eff} = f\epsilon_i + (1-f)\epsilon_h \tag{4.3}$$

where f is the volume fraction of the inclusion. In this case ϵ_{eff} becomes as shown in Fig. 4.10 for mixtures of varying mixing fraction at T= 20 K. The two dominant features are the STO TO_1 soft mode at 30 cm^{-1} and the TO phonon of NiO at 400 cm^{-1}. In addition, the weaker TO_2 and TO_3 modes of STO are visible. Now that the effective dielectric constant is known, it is possible to model the reflectance of the sample at normal incidence,

$$R = \left|\frac{n-1}{n+1}\right|^2 \tag{4.4}$$

where $n = \sqrt{\epsilon\mu}$ is the refractive index. A simulation of the reflectance for the effective medium of Fig. 4.10 is shown in Fig. 4.11. Each of the IR modes contributes a reststrahlen region of high reflection in the spectrum. In the 30-100 cm^{-1} region of the f=0.15 sample we see a region of nearly perfect reflectance corresponding to the region of negative permittivity. This is the frequency range where the index of refraction is expected to turn negative at $\sim$ 35 cm^{-1} where the magnetic resonance occurs [73] according to weighted average mixing.

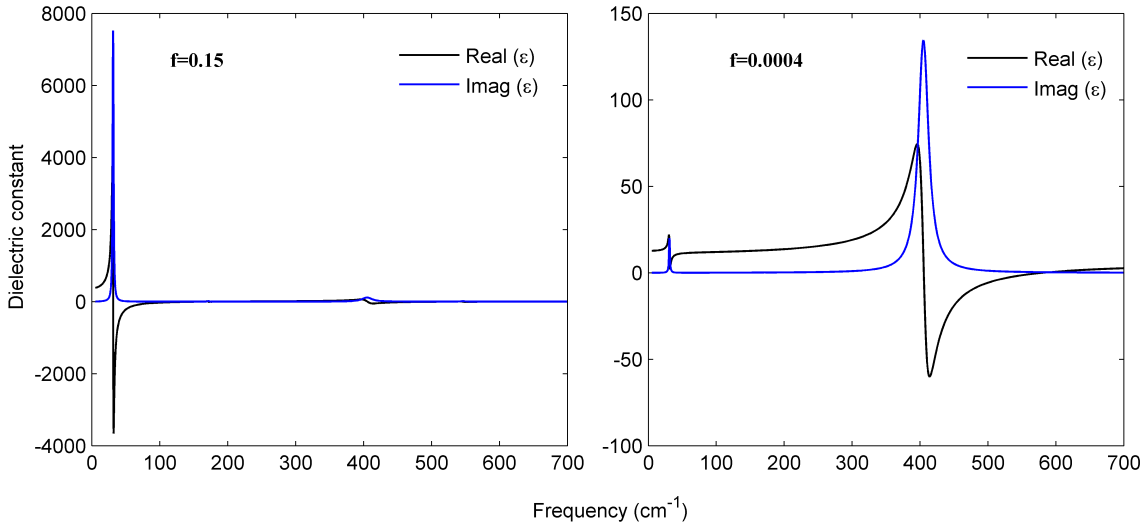

Figure 4.10: Effective dielectric constant using Eq. 1.3 for f=0.15 and f=0.0004 at T = 20 K.

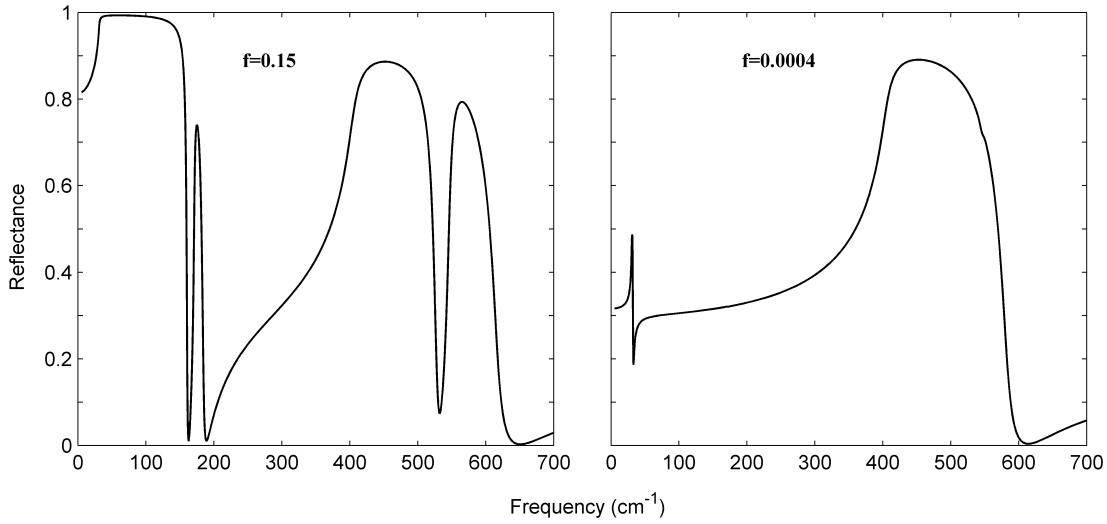

Figure 4.11: Simulation of reflectance using Eq. 1.4 for f=0.15 and f=0.0004 at T= 20 K.

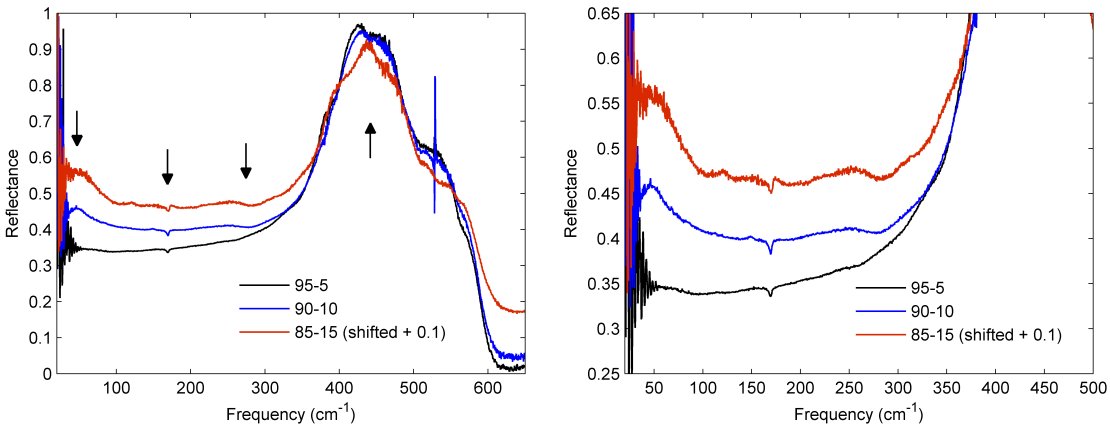

Figure 4.12: Measured ceramic reflectance at 80 K. The arrows indicate the prominent modes in the spectrum. The value of the 85-15 data was shifted up by 0.1 along the y-axis for clarity.

4.5 Data

A Fourier Transform Infrared (FTIR) spectrometer was used to measure far-infrared reflectance in the range 10-650 cm^{-1}. The spectra for the 95-5, 90-10 and 85-15 samples are shown in Fig. 4.12 at T= 80 K and in Fig. 4.13 at T= 295 K. Fig. 4.14 shows the detailed temperature dependence of the 85-15 sample. Based on this set of data we do not see the expected region of negative permittivity in the composite as required for negative refraction which would manifest itself in the reststrahlen region as seen in Fig. 4.11. For the 95-5 sample, the reflection shows virtually no difference compared to the pure NiO, also in contrast with the simulation. Thus we have embarked on investigating the interaction effects that lead to the effective optical constants we observe.

There are four prominent modes seen in the data and marked with arrows in Fig. 4.12. In the order of increasing frequency they are: 1) A temperature dependent feature in the range 50-100 cm^{-1} that decreases in frequency on lowering the temperature and appears to behave similarly to the bulk STO soft mode. However, it is considerably broadened in the composite, appears at lower frequencies (90 cm^{-1} at

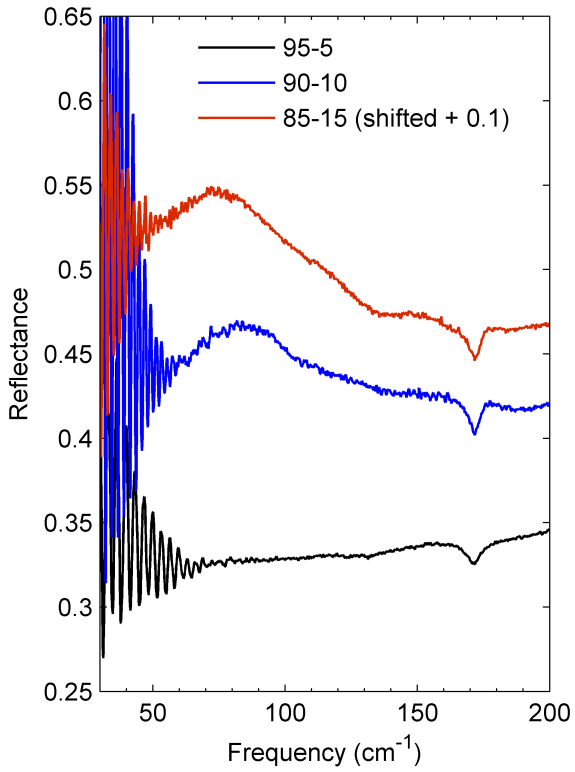

Figure 4.13: Measured ceramic reflectance at 295 K. The value of the 85-15 data was shifted up by 0.1 along the y-axis for clarity.

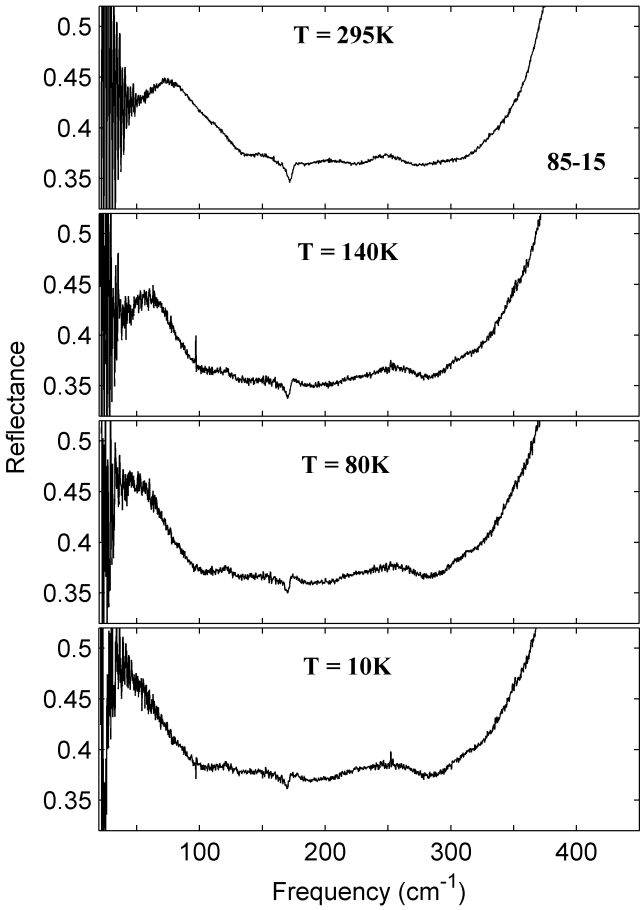

Figure 4.14: Temperature dependence of the reflectance of the 85-15 composite.

room temperature in bulk STO versus 75 cm^{-1} for the 85-15 sample), and is dependent on the inclusion concentration (90 cm^{-1} in bulk, 84 cm^{-1} in the 90-10, 75 cm^{-1} in 85-15 at room temperature). 2) A feature at 172 $cm^{-}1$ which we ascribe to the bulk TO_2 mode of STO. 3) A feature at $\sim$260 cm^{-1} that does not correspond to any bulk modes of the constituents and is therefore a new collective mode. This is the confined soft mode of the nearly spherical STO nano-particles known as the Fröhlich mode which will be discussed in the analytical section. 4) A broad feature between 400-600 cm^{-1} corresponding to the reststrahlen region of NiO. Finally, we see a broad increase in reflection in between (1) and (3) corresponding to 50-300 cm^{-1} which is also a nano-particle feature.

Comparing the data with the reflectance simulation of Fig. 4.11 based on the simple proportional mixing rule, we see a correspondence between features (1), (2), (4) of the data and the peaks in the simulation. The soft mode at 90 cm^{-1} is significantly stronger in the simulation and its position does not depend on the mixing fraction. The features (2) and (4) are almost identical with the simulation. Neither the Fröhlich mode (feature (3)) nor the broad increase in reflection from 50-300 cm^{-1} are visible in the simulation due to the fact that they are finite-size particle modes.

4.6 Clausius-Mosotti equation

So far in our interpretation of the data in Figs. 4.12-4.14 we have considered only the simplest case of weighted averaging which results in a resonant feature in the composite at the bulk STO soft mode frequency of 90 cm^{-1} at room temperature. We also know based on the discussion in Appendix A, that this case represents a spectral bound on the resonant features of an arbitrary ionic-inclusion composite at low filling fractions, where the electrostatic resonances can occur anywhere in the region of negative permittivity of ϵ_i/ϵ_h, between 90 and $\sim$500 cm^{-1} at room temperature for the STO/NiO combination. Let us now consider the most realistic geometry of our

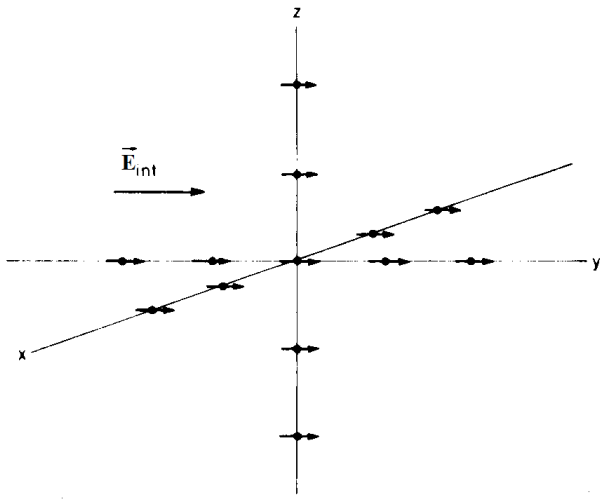

Figure 4.15: Schematic diagram of the simple cubic lattice used in the derivation of the Clausius-Mosotti relation, with $\mathbf{E}_{int}$ as the applied field. Taken from [82].

mixtures which is the case of well distributed, nearly spherical STO particles present at less than 15% volume fractions in the NiO host. The particle sizes are 0.5-1 μm for the large STO grains and less than 100 nm for the nano-grains, which renders them significantly smaller than the wavelength of light up to $\sim$300 cm^{-1}. This is the domain of the quasi-static geometry based on the Clausius-Mosotti equation [82, 85]. The Clausius-Mosotti equation relates the polarizability of individual dipoles dispersed in space in the presence of an applied field to the polarization and macroscopic fields of the effective solid. The traditional derivation is done for the geometry of a cubic lattice although the framework can be applied to random/uncorrelated systems [86, 87, 88]. We proceed with the traditional derivation first. As in the case of previous geometries considered, the approach we will take in deriving the effective dielectric constant of the current structure will be a microscopic calculation of the fields in all of space, under given approximations, and then taking the average to obtain $\epsilon_{eff} = \frac{<D>}{<E>}$. Consider a cubic lattice of small dielectric spheres which are approximated as perfect dipoles suspended in free space in the presence of an applied field $\mathbf{E}_{int}$. Later, the derivation will be modified to add polarizable background material. The points of

polarizability α are arranged at positions $\mathbf{r} = \mathbf{R}_i$ corresponding to a simple cubic lattice extending to infinity as shown in Fig. 4.15. The local field at each site will induce a dipole $\mathbf{p}_i = \alpha \mathbf{E}(\mathbf{R}_i)$, where $\mathbf{E}(\mathbf{R}_i) = \mathbf{E}_{loc}$ is the same at all sites by symmetry and $\mathbf{E}_{loc}$ is yet unspecified. The solution for the field $\mathbf{E}(r)$ in all of space is a function of the applied field and the surrounding dipoles,

$$\mathbf{E}(\mathbf{r}) = \mathbf{E}_{int} + \sum_i \mathbf{E}(\mathbf{p}_i, \mathbf{r} - \mathbf{R}_i), \tag{4.5}$$

where the sum extends over all $\mathbf{R}_i$ and $\mathbf{E}(\mathbf{p}, \mathbf{r})$ is the electric field of a dipole located at the origin,

$$\begin{aligned} \mathbf{E}(\mathbf{p}, \mathbf{r}) &= -\nabla(\frac{\mathbf{p} \cdot \mathbf{r}}{4\pi\epsilon_0 r^2}) & (4.6) \\ &= \frac{3(\mathbf{p} \cdot \mathbf{r})\mathbf{r} - r^2\mathbf{p}}{4\pi\epsilon_0 r^5}, & (4.7) \end{aligned}$$

where Eq. 4.7 is valid for $r > 0$ [85, Ch. 4]. Similarly, $\mathbf{p}(\mathbf{r})$ is a function of the dipoles located at all lattice sites,

$$\mathbf{p}(\mathbf{r}) = \sum_i \alpha \mathbf{E}(\mathbf{R}_i)\delta(\mathbf{r} - \mathbf{R}_i). \tag{4.8}$$

We may find the local field by evaluating Eq. 4.5 at the origin,

$$\mathbf{E}_{loc} = \mathbf{E}(0) = \mathbf{E}_{int} + {\sum_i}' \mathbf{E}(\alpha \mathbf{E}_{loc}, -\mathbf{R}_i), \tag{4.9}$$

where the prime denotes exclusion of the site $\mathbf{R} = 0$ in the sum. We may evaluate Eq. 4.9 by considering the $\hat{z}$ component of the local field $\mathbf{E}_{loc} = \mathbf{E}(0)$ within an expanding shell,

$$\mathbf{E}_{loc} \cdot \hat{z} = \mathbf{E}_{int} \cdot \hat{z} + \frac{\alpha E_{loc}}{4\pi\epsilon_0} {\sum_i}' \frac{3z_i^2 - r_i^2}{r_i^5} = \mathbf{E}_{int} \cdot \hat{z} + \frac{\alpha E_{loc}}{4\pi\epsilon_0} {\sum_i}' \frac{2z_i^2 - x_i^2 - y_i^2}{r_i^5}. \tag{4.10}$$

Since the x, y, z directions are equivalent due to the symmetry of the lattice and the shell, we get

$$\sum_i{}' \frac{x_i^2}{r_i^5} = \sum_i{}' \frac{y_i^2}{r_i^5} = \sum_i{}' \frac{z_i^2}{r_i^5},$$

and the sum of Eq. 4.10 evaluates to zero. The same logic applies to the $\hat{x}$, $\hat{y}$ components of $\mathbf{E}_{loc}$. From this we get the exciting local field at each dipole site,

$$\mathbf{E}_{loc} = \mathbf{E}(0) = \mathbf{E}_{int}. \tag{4.11}$$

The sum of all the surrounding dipoles vanishes due to symmetry of the lattice so that the local field is just the applied field. The complete solution for $\mathbf{E}(\mathbf{r})$, $\mathbf{p}(\mathbf{r})$ for all $\mathbf{r}$ in terms of the applied $\mathbf{E}_{int}$ is:

$$\mathbf{E}(\mathbf{r}) = \mathbf{E}_{loc} + \sum_i \mathbf{E}(\alpha \mathbf{E}_{loc}, \mathbf{r} - \mathbf{R}_i), \tag{4.12}$$

$$\mathbf{p}(\mathbf{r}) = \sum_i \alpha \mathbf{E}_{loc} \delta(\mathbf{r} - \mathbf{R}_i), \tag{4.13}$$

$$\mathbf{E}_{loc} = \mathbf{E}_{int}. \tag{4.14}$$

Now that the microscopic fields have been derived, we must implement the averaging procedure in order to relate the average macroscopic fields to the effective dielectric constant. The volume average over a spherical cavity centered at the origin for the dipole moment per unit volume is,

$$< \mathbf{P} > = \frac{1}{V} \int_V d^3 r \mathbf{p}(\mathbf{r}) = \frac{1}{V} \sum_i \mathbf{p}_i = n\alpha \mathbf{E}_{loc} \tag{4.15}$$

where n is the number of points per unit volume. In order to calculate $< \mathbf{E} >$, we will employ a general result for the integral of the electric field due to an arbitrary

charge distribution within a spherical volume [85, Ch. 4],

$$\int_V \mathbf{E}(\mathbf{r}) d^3r = -\frac{\mathbf{p}_{in}}{3\epsilon_0} \tag{4.16}$$

where $\mathbf{p}_{in}$ is the internal electric dipole moment with respect to the center of the sphere. Applying this result to Eq. 4.12 we have,

$$< \mathbf{E} >= \mathbf{E}_{loc} - \frac{1}{3\epsilon_0} n\alpha \mathbf{E}_{loc} = \mathbf{E}_{loc} - \frac{1}{3\epsilon_0} < \mathbf{P} > . \tag{4.17}$$

The above result represents the famous Lorentz relation for the local field in a dense medium, and is known as the "first solve/then average" method due to Lorentz [87] since we first derived a microscopic solution for the fields and then averaged to obtain the macroscopic quantities. The second known derivation, also due to Lorentz, is the "first average/then solve" problem which relies on a fictitious cavity that mathematically separates the near and far contributions of dipoles to the local field [75, Ch. 13]. The first derivation is more rigorous, whereas the second has the advantage of treating finite-sized objects. By eliminating $\mathbf{E}_{loc}$ from Eqs. 4.15, 4.17 to obtain an expression for $\epsilon - 1 = \chi = \frac{1}{\epsilon_0}\frac{<P>}{<E>}$ and then solving for $n\alpha$ we arrive at the Clausius-Mosotti (CM) relation,

$$\frac{\epsilon_{eff} - 1}{\epsilon_{eff} + 2} = \frac{n\alpha}{3\epsilon_0}, \tag{4.18}$$

which connects the macroscopic dielectric constant to the density and polarizability of the inclusion. We can simply extend the above derivation by considering a mixture made up of several phases of inclusions of different polarizabilities, as for the ionic crystal NaCl, for example, where each of the Na^+ and Cl^- ions has a simple cubic symmetry. In this case, Eq. 4.15 is modified to $< \mathbf{P} > = \sum_i n_i \alpha_i \mathbf{E}_{loc}$, where i

designates the atom type. Thus, the multi-phase CM relation becomes,

$$\frac{\epsilon_{eff}-1}{\epsilon_{eff}+2}=\frac{1}{3\epsilon_0}\sum_j n_j\alpha_j. \tag{4.19}$$

4.7 Examples of geometries

If we consider a mixture made up of two phases, $\epsilon_i(\omega)$ for the STO inclusion and $\epsilon_h(\omega)$ for the NiO host, then the effective dielectric constant for a dilute mixture is described by the Maxwell-Garnett (MG) formula, as shown in Appendix B, which is an extension of the CM relation given by Eq. 4.19 with the added property of having finite-size inclusions as opposed to point dipoles,

$$\epsilon_{eff}=\epsilon_h+\frac{\frac{1}{3}\sum_i f_i(\epsilon_i-\epsilon_h)\sum_{k=1}^{3}\frac{\epsilon_h}{\epsilon_h+N_{ik}(\epsilon_i-\epsilon_h)}}{1-\frac{1}{3}\sum_i f_i(\epsilon_i-\epsilon_h)\sum_{k=1}^{3}\frac{N_{ik}}{\epsilon_h+N_{ik}(\epsilon_i-\epsilon_h)}}. \tag{4.20}$$

This relation takes into account the general ellipsoid geometry of inclusion for which the sphere is a special case. The ellipticity is described by the depolarization factor N_{ik}, where i corresponds to the inclusion phase and k being one of the principal axes. For the case of a sphere: $N_{i1}=N_{i2}=N_{i3}=1/3$. The main assumption in Eq. 4.20 regarding the size of inclusions is the quasi-static approximation. Moreover, as discussed in Appendix B, this relation holds either for a cubic lattice or for uncorrelated distribution of inclusions in which case the local field at any inclusion site is identical. Thus clustering effects may not be included unless the clusters are dense and may be regarded as single particles. The shape of the particle determines the exact electrostatic resonance behavior within the region of negative permittivity of the inclusion (see Appendix A).

To show how the electrostatic resonances of the inclusions affect the absorption spectra in the effective mixture we will consider several different inclusion geometries–

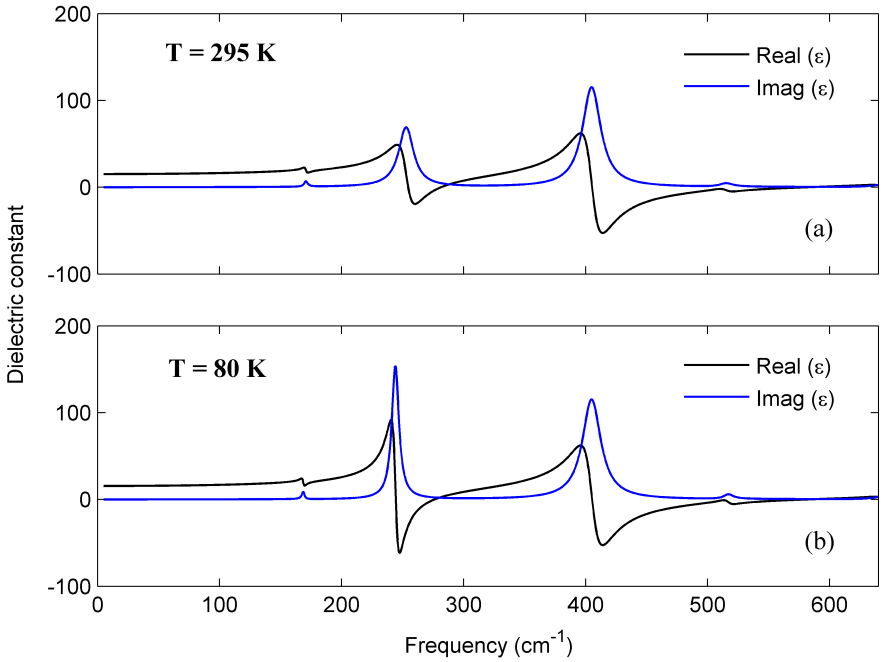

Figure 4.16: Simulation of the effective dielectric constant of a 90-10 mixture of NiO-$SrTiO_3$ containing spherical inclusions for (a) T = 295 K and (b) T = 80 K.

sphere, ellipsoid, and a distribution of ellipsoids–all of which are incorporated in Eq. 4.20. First we consider a 90-10 mixture of single phase spherical inclusions, with the results for the effective dielectric constant and reflectance using the generalized MG formula shown in Figs. 4.16 and 4.17.

Despite having a significant fraction of STO, the mixture no longer shows a resonance at the bulk TO_1 frequency of the inclusion. Instead, the resonance shifts to 260 cm^{-1} corresponding to $\epsilon_i(\omega_0) = -\epsilon_h(2+f)/(1-f) \approx -2\epsilon_h$ in the limit of small f, which is the electrostatic resonance of a sphere in a dielectric host background also known as the dipolar surface plasmon, excited by a uniform electric field. The frequency ω_0 where this condition is satisfied is the the Fröhlich resonance frequency. A perturbation expansion of Eq. 4.20 in orders of f_i gives ($f_i \ll 1$),

$$\epsilon_{eff} \approx \epsilon_h + \frac{1}{3}\sum_i f_i(\epsilon_i - \epsilon_h)\sum_{k=1}^{3}\frac{\epsilon_h}{\epsilon_h + N_{ik}(\epsilon_i - \epsilon_h)}. \tag{4.21}$$

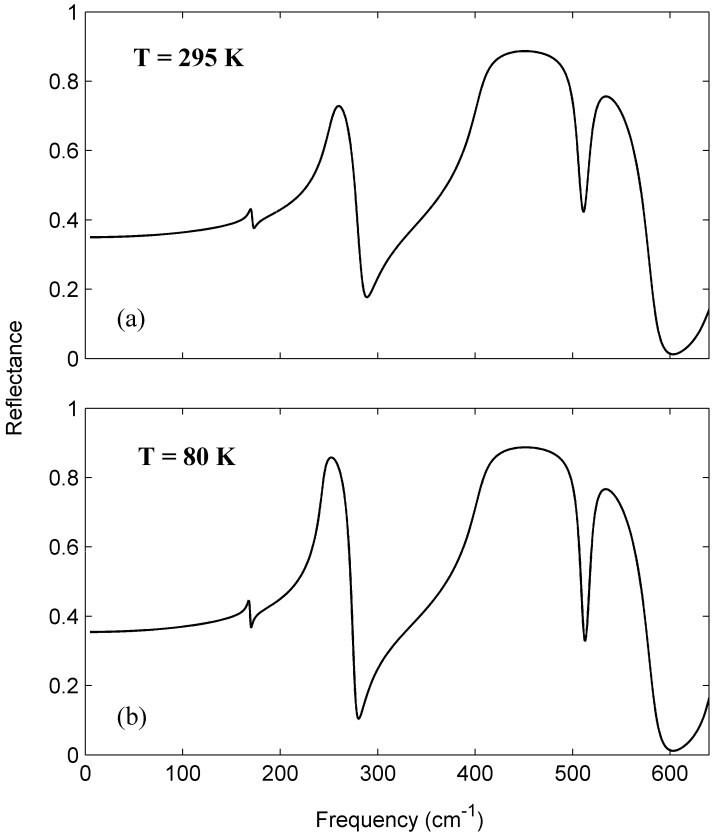

Figure 4.17: Simulation of reflectance of a 90-10 mixture of NiO-$SrTiO_3$ containing spherical inclusions for (a) T = 295 K and (b) T = 80 K.

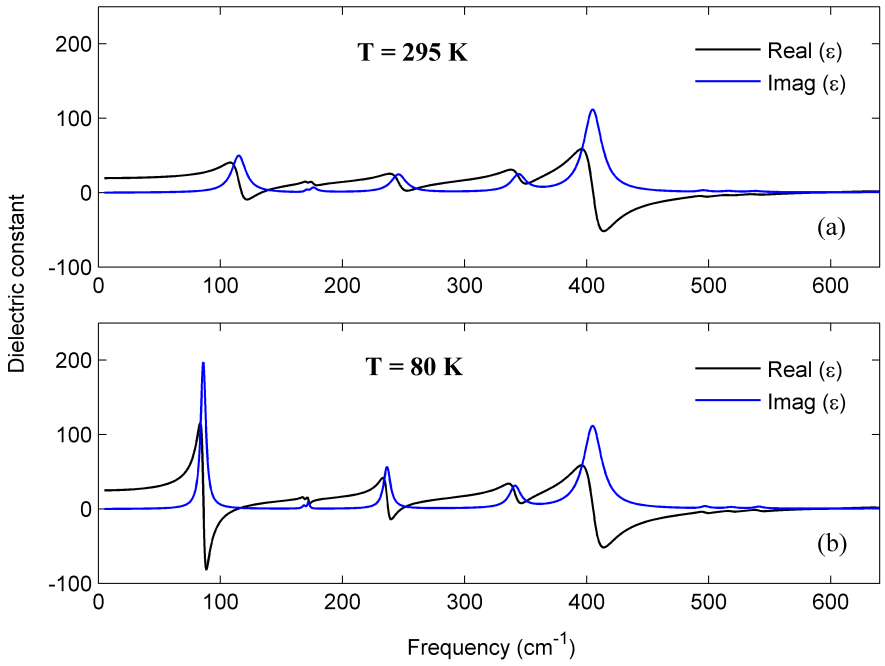

Figure 4.18: Simulation of the effective dielectric constant of a 90-10 mixture of NiO-$SrTiO_3$ containing ellipsoidal inclusions having axial ratio of 11.5 : 2.3 : 1 for (a) T = 295 K and (b) T = 80 K.

Thus the behavior of a dilute CM-type of mixture is dominated by the resonance of individual inclusions. We see a dominant feature in the reflectance data at ∼260 cm^{-1} corresponding to the spherical resonance. This provides an explanation of the feature (3) in our data of Figs. 4.12, 4.14 which could not be understood using simple volume averaged mixing. We note that this feature had not been observed in previous measurements of an identical ceramic mixture [23] due to the fact that the composites contained 50% of inclusion by volume which we believe interferes with the single particle effect. As noted above, the CM approximation is only valid for dilute mixtures, otherwise clustering dominates and the inclusion/host phases may no longer be distinguished.

For the case of ellipsoidal inclusions, the poles now depend on the depolarization factors, N_k, with the resonance condition being $\epsilon_i(\omega_0) = -(1/N_k - 1)\epsilon_h$. When the orientation is averaged, an ellipsoid contributes three modes corresponding to the

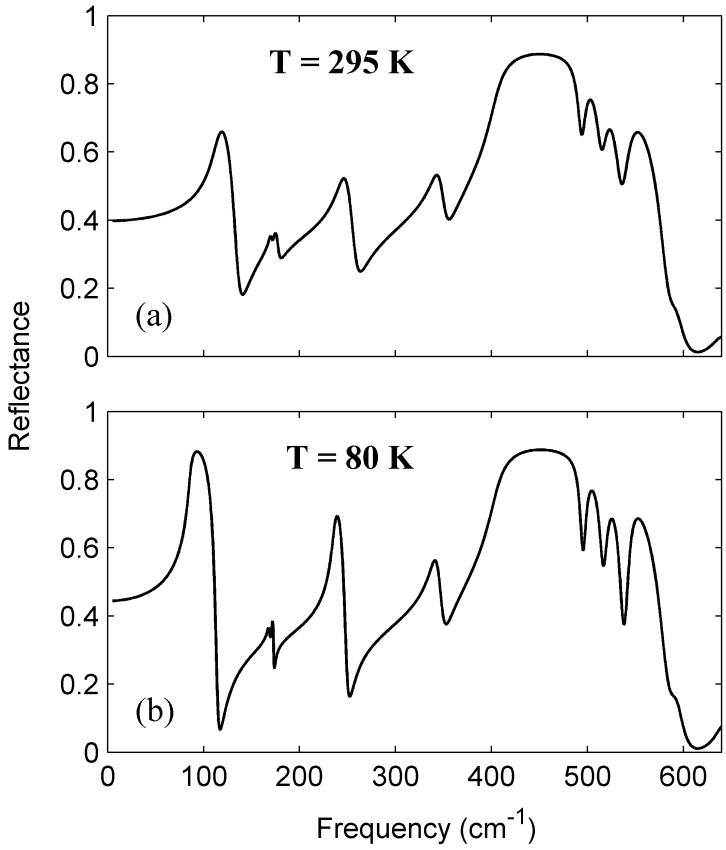

Figure 4.19: Simulation of the reflectance of a 90-10 mixture of NiO-$SrTiO_3$ containing ellipsoidal inclusions having axial ratio of 11.5 : 2.3 : 1 for (a) T = 295 K and (b) T = 80 K.

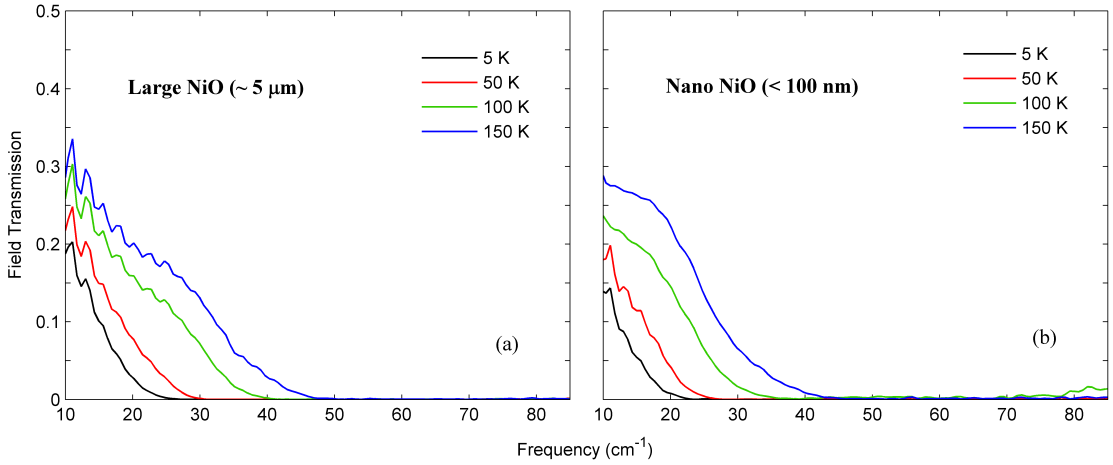

Figure 4.20: Comparison of measured transmission as a function of temperature of a 90-10 mixture of NiO-$SrTiO_3$ for (a) large particle NiO host, 470 μm sample thickness and (b) nano-particle NiO, 405 μm sample thickness

three principal axes, as seen in Figs. 4.18, 4.19 which show the effective properties of a mixture with ellipsoidal inclusions having axial ratio of 11.5:2.3:1. In addition to the NiO mode at 400 cm^{-1} and TO_2, TO_4 modes of STO, we see strong peaks at ∼100, 240, 340 cm^{-1} due to the ellipsoid. In fact, each of the TO modes of STO splits into three peaks, although the splittings of the TO_2 and TO_4 are significantly weaker. The modes of the ellipsoid are determined solely by the geometry; the orientation with respect to the incident field determines the relative intensity. For the case of highly elongated, needle-like inclusions, $N_k \to 0$ and $\epsilon_i(\omega_0) \to \infty$ which shifts the resonance toward the bulk TO frequency. Thus a possible explanation for the dominant feature (1) in Figs. 4.12-4.14 is the formation of needle-like channels of STO inclusions. Such behavior has been observed previously for needle-like composites [98] and the concept of elongated chains has been called upon to explain the presence of unusually large absorption at the bulk TO frequency of MgO smoke and other ionic powders [99, 100, 101]. It was determined later that clustering was responsible for the absorption at the ω_T frequency [102], however, no consensus was reached with regard to the importance of chains [101, 103]. Due to the presence of larger NiO grains in our samples (see

Fig. 2.11) which could serve as a matrix for the formation of nano-channels of the smaller STO grains along the grain boundaries, we investigated this problem further by fabricating composites containing nano-particle (<100 nm) NiO host. This should in principle remove any bias toward the macroscopic preponderance of STO channels or needle-like inclusions. The transmission data up to 85 cm^{-1} in the region of the bulk mode is shown in Fig. 4.20 for a range of temperatures for both nano-NiO host and micron-sized NiO. The transmittance is lower for the nano-NiO sample which could be due to the difference in the density of the synthesized nano-particles as compared to the bulk or differences in porosity, both of which would affect the STO inclusion volume fraction. However, the roll-off in transmission and the shifting of the absorption edge toward low frequency with temperature is quite similar which suggests that the bulk STO feature at the soft mode frequency is present in both samples independently of the NiO grain size. If the low frequency mode depended on the presence of channels due to large NiO grains, then the transmission should have stayed flat at ∼0.3 in Fig. 4.20 (b). For this reason we do not think that the needle effect is significant in our samples. Since the starting inclusion geometry of the constituent particles is nearly spherical, for which the resonance is far removed from the bulk TO frequency, we must look to particle clustering to explain the strong feature in the reflectance range of 20-100 cm^{-1}.

We now consider a uniform distribution of ellipsoidal inclusions of varying axial ratios. As discussed previously, we can approximate dense clusters of STO inclusions as larger ellipsoids of a given ellipticity. Since the distribution, geometry and orientation of the clusters is random, we consider a uniform distribution of ellipsoids [104]. We assume a large number of different dense clusters or elongated particles, each corresponding to a fixed ellipsoid geometry, which in sum add to the total inclusion fraction. For a fine enough distribution, the sum over i in Eq. 4.20 is transformed

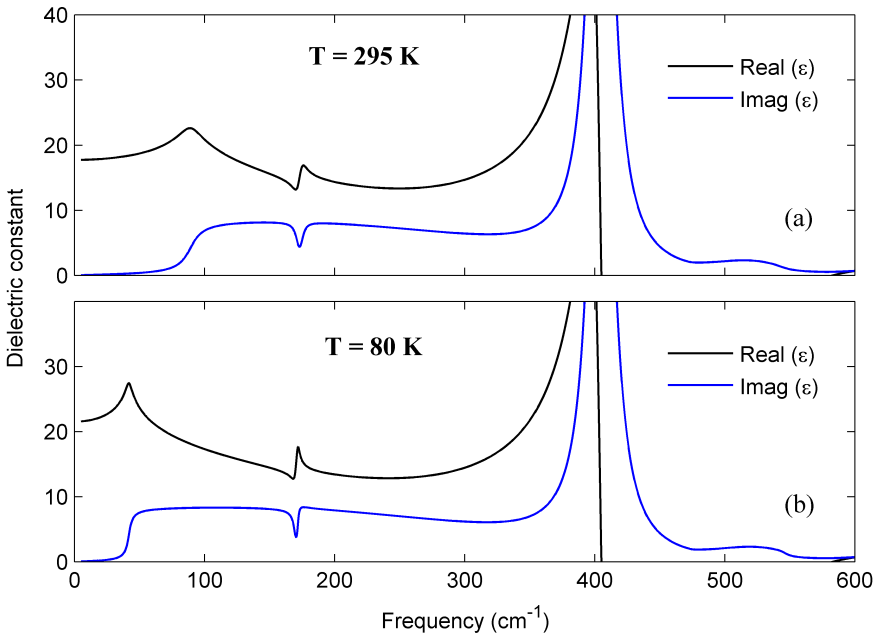

Figure 4.21: Simulation of the effective dielectric constant of a 90-10 distributed ellipsoid mixture of NiO-$SrTiO_3$ for (a) T = 295 K and (b) T = 80 K.

into an integral,

$$\sum_i f_i \rightarrow \int_0^1 dN_x \int_0^{1-N_x} dN_y \, f_i(N_x, N_y, 1 - N_x - N_y), \tag{4.22}$$

where $f_i(N_x, N_y, 1 - N_x - N_y)$ is the probability density for an ellipsoid of dielectric constant ϵ_i having depolarization factors $\{N_x, N_y, 1 - N_x - N_y\}$. The current framework does not allow intermixing of particles with different dielectric constants within the same dense cluster that is approximated as an ellipsoid. Thus if there are particles or clusters present having different dielectric constants, ϵ_i, they will have an associated f_i that must be integrated separately. For the case of a continuous distribution, $f_i(N_x, N_y, 1 - N_x - N_y) = f_i/2$ [105]. The results for the effective dielectric constant and reflectance of a distributed composite are shown in Figs. 4.21 and 4.22.

The main feature that we see is a broad absorption band in between the TO and LO frequencies of the bulk STO soft mode, corresponding to the region of negative

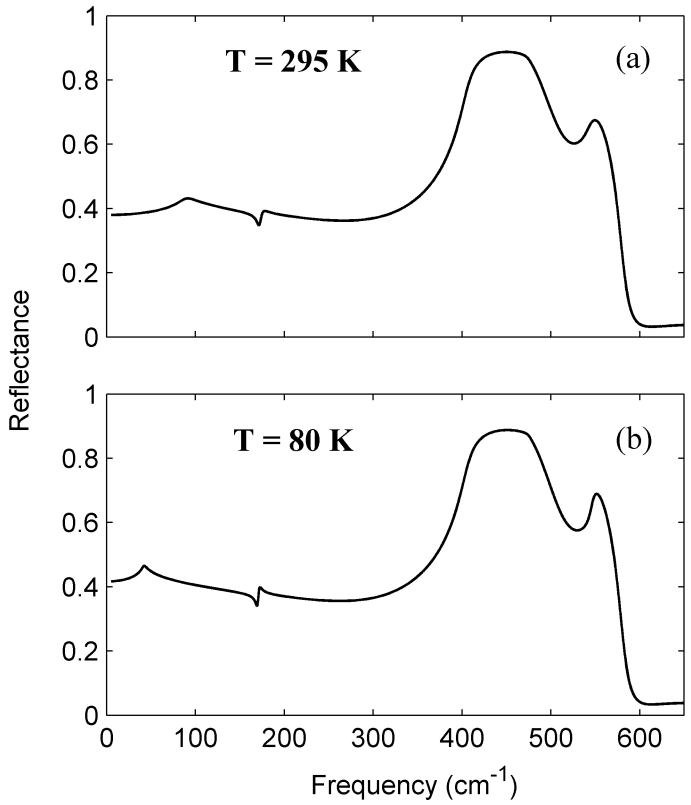

Figure 4.22: Simulation of the reflectance of the 90-10 distributed ellipsoid mixture of NiO-$SrTiO_3$ for (a) T = 295 K and (b) T = 80 K.

permittivity of the inclusion. The TO frequency is temperature dependent and thus the rising edge moves from 90 cm^{-1} at T= 295 K to 50 cm^{-1} for T= 80 K. In both cases the absorption band tails off at $\sim$550 cm^{-1}, which is the nearly temperature independent LO frequency. Thus for a uniform distribution we see a continuum of poles allowed by the Bergman spectral representation as is intuitively obvious for a random mixture. Even though the details of each particular pole will be different for our sample containing clusters of spheres as opposed to ellipsoids, the band is expected to be filled nevertheless with a continuous distribution. Finally, we see a peak in the real part of the dielectric constant at the TO frequency. However, this is not the bulk TO mode, which has transformed into a wide band, but an indication of where the band starts. From Kramers-Kronig analysis, a rise in absorption at the TO frequency of the Im$\{\epsilon\}$ will be associated with a peak in the Re$\{\epsilon\}$. Thus in the reflectance simulation we see a temperature dependent peak at the bulk TO frequency indicating the onset of the absorption band. We also see complementary information in the transmission data of Fig. 4.20 which shows the onset of asymmetric absorption.

4.8 Comparison of data and simulation

In order to obtain a fit with the reflectance data, we combine the features of ellipsoidal distribution and the isolated spherical resonance as described above. We assume that the total inclusion fraction is made up of two dominant terms, $f = f_e + f_s$, one corresponding to ellipsoidal inclusions which result from inclusion particle clustering or from unusually elongated single particles and the fraction of inclusions that are nearly spherical. We use the following probability density in the extended MG formula,

$$f_i(N_x, N_y, 1 - N_x - N_y) = \frac{f_e}{2} + f_s \delta^2 (N_x - \frac{1}{3}, N_y - \frac{1}{3}). \tag{4.23}$$

Table 4.1: Best fit inclusion fractions for NiO-$SrTiO_3$ composites with inclusion volume up to 15%.

f	f_e	f_s
0.05	0.0475	0.0025
0.1	0.095	0.005
0.15	0.1425	0.0075

For now we ignore the dependences of f_e and f_s on the inclusion concentration and take the spherical inclusion fraction as $\frac{1}{20}$th of the total inclusion volume at all concentrations. The best fit parameters under these assumptions for data of varying inclusion concentration are shown in Table 4.1.

In Figs. 4.23-4.25 we show the reflectance simulations using the parameters of Table 4.1 for T=80 K, T=295 K, and the temperature dependence of the 85-15 sample, respectively. These simulations are in comparison to the data of Figs. 4.12-4.14. We see good agreement in regard to the presence of all observed spectral features (1)-(4) as discussed in Section 4.5. The fit for the 90-10 concentration is closest to the simulation, whereas the 95-5 and 85-15 show some deviations in the low frequency region. The spherical resonance in the simulation has a narrower linewidth which results in the more pronounced peak in the reflectance, which we ascribe to broadening due to deviations of the f_e fraction of the inclusion particles from spherical shape. Lastly, we show the measured electric permittivity of the 85-15 composites containing nano- and micron-sized NiO host in Fig. 4.26 compared to the simulation of Fig. 4.27. The measured values are obtained from the transmission measurement data in Fig. 4.20. The values of $\epsilon_{eff} \sim 25-40$ in this frequency range amount to a large reduction compared to weighted average mixing of Eq. 4.3, which predicts $\epsilon \approx 400$ in the same frequency range at 20 K (Fig. 4.10). The reduction in the effective permittivity by one order of magnitude further supports our model which describes the transformation of the bulk soft mode into a distributed feature at higher frequencies leading to the reduction of the static effective dielectric constant.

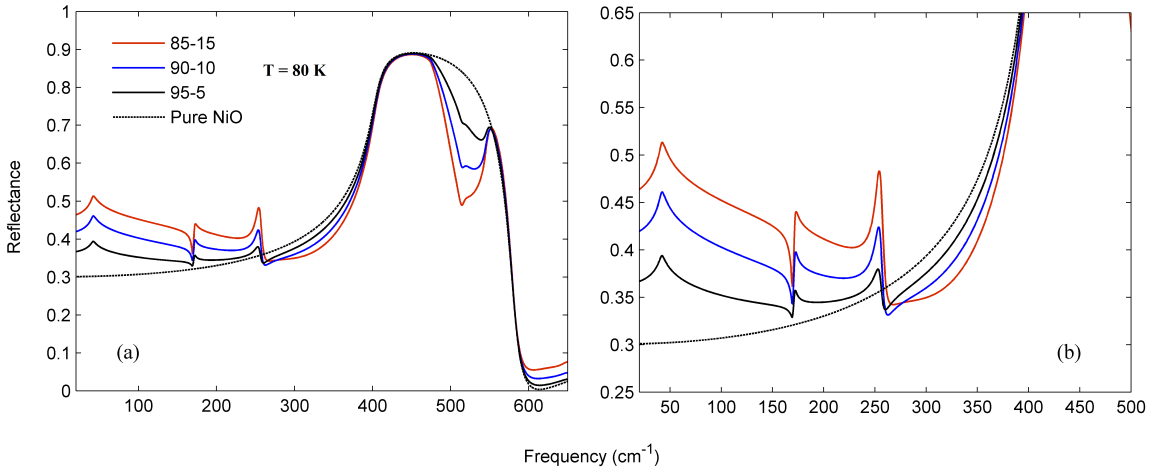

Figure 4.23: Simulation of reflectance of the NiO-$SrTiO_3$ mixture for different inclusion concentrations at T= 80 K using best fit f_e, f_s. Part (a) shows the full scale and (b) enlarges the low frequency behavior.

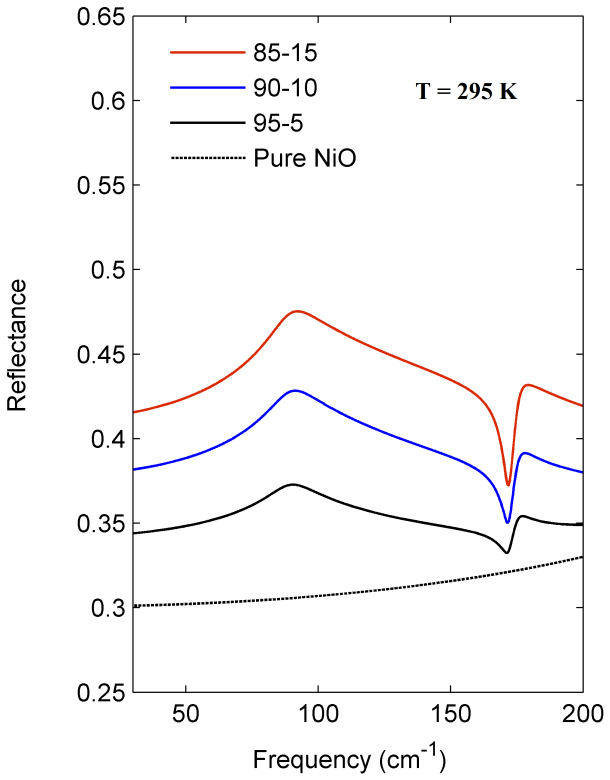

Figure 4.24: Simulation of reflectance of the NiO-$SrTiO_3$ mixture for different inclusion concentrations at T= 295 K using best fit f_e, f_s.

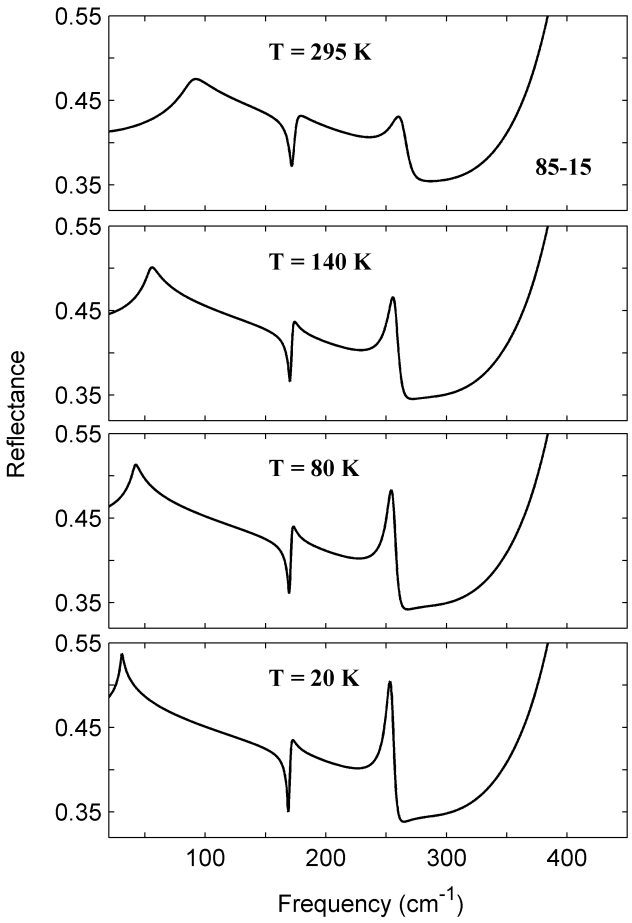

Figure 4.25: Simulation of reflectance of the 85-15 NiO-$SrTiO_3$ mixture as a function of temperature using best fit f_e, f_s.

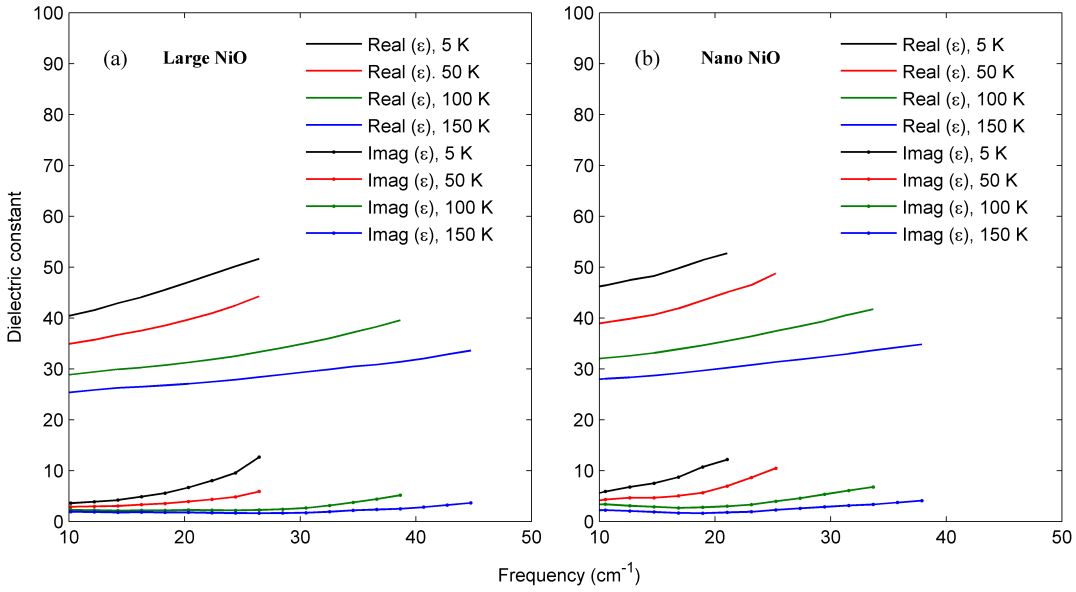

Figure 4.26: Real and imaginary parts of the dielectric constant as measured for the 85-15 NiO-$SrTiO_3$ mixtures as a function of temperature for (a) large particle NiO host and (b) nano-particle NiO

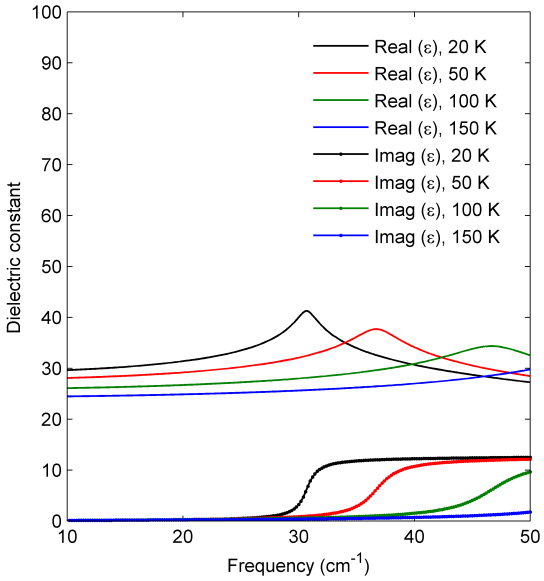

Figure 4.27: Simulation of the dielectric constant of the 85-15 NiO-$SrTiO_3$ mixture as a function of temperature using best fit f_e, f_s.

Now we discuss some of the discrepancies between the data and model. With regard to the low frequency feature (1) in the data of Figs 4.12-4.14, we see for the case of the 95-5 composite that the peak is barely visible, but makes a significant increase when the inclusion concentration goes up to 10%. In the simulation the increase of the low frequency mode as a function of inclusion fraction happens uniformly within the 0-15% range, in contrast to the measurement. We suspect this discrepancy is a result of not including the dependence of f_s/f_e on total inclusion fraction. The low frequency feature which is described by the onset of the ellipsoidal distribution is dependent on the presence of clusters. However, for low enough inclusion concentrations, we expect less clustering and thus the inclusion type of nearly spherical geometry will be more prevalent. For this reason, at low inclusion concentrations the low frequency peak will tend to decrease for two reasons: 1) the disappearance of clusters and 2) the general decrease in the inclusion concentration. The Fröhlich mode, on the other hand, will decrease only as a function of decreasing inclusion fraction. Thus we expect a stronger decrease in the low-frequency mode as compared to the Fröhlich mode at low concentrations.

For the high values of inclusion, we see a noticeable dependence of the low frequency peak position on the inclusion concentration which becomes especially clear for the 85-15 data at T= 295 K where the peak appears at 75 cm^{-1} as compared to 84 cm^{-1} for the 90-10 sample. Since the frequency of this feature, corresponding to the onset of the TO-LO absorption band occurs at the TO soft mode frequency of STO, its dependence on the inclusion fraction as well as the shifting to frequencies below the TO soft mode is difficult to explain within the current framework. Continuing with the previous line of thinking, if at low inclusion fractions ellipsoidal clusters tend to disappear then at high inclusion fractions they should get larger and become more prevalent. In order to understand this behavior, we need to consider the dependence of the geometrical resonance on particle size, which requires us to take into account

retardation effects.

4.9 Inclusion size dependence

So far the underlying assumption for all effective properties has been the quasi-static approximation of particle radius $a \ll \lambda$. However, at high enough inclusion concentrations we expect to see this assumption break down as more aggregation of STO particles begins to take place. In this section we abandon the electrostatic approximation and consider the full set of Maxwell equations in order to understand the behavior of particles with sizes comparable to the wavelength of light.

If we consider an infinite ionic solid, with the dielectric constant as given in Eq. A.2, then any allowed electric or magnetic field $\mathbf{F}(\mathbf{r})$ must be a solution in all of space to the full set of four Maxwell equations. If we assume $\exp(-i\omega t)$ dependence, then the two curl equations $\nabla \times \mathbf{E} = i\frac{\omega}{c}\mathbf{H}$, $\nabla \times \mathbf{H} = -i\frac{\omega}{c}\mathbf{E}$ lead to the vector wave equation,

$$\nabla \times (\nabla \times \mathbf{F}) - (\omega^2\epsilon/c^2)\mathbf{F} = 0, \tag{4.24}$$

where $\mathbf{F}$ represents either the electric or magnetic field. For the case of an infinite solid geometry, the general solution for any field component is satisfied by plane waves of the form $\sim \exp(i\mathbf{k}\cdot\mathbf{r} - i\omega t)$ which must be one of two types–longitudinal or transverse–which follows from $\nabla\cdot\mathbf{D} = 0$. The longitudinal plane waves can only exist for $\epsilon = 0$ and have all their fields parallel to the propagation vector. The transverse plane waves have field components perpendicular to the direction of propagation and must satisfy the dispersion relation,

$$k^2 = \epsilon(\omega/c)^2, \tag{4.25}$$

where c is the speed of light. This is the well known phonon-polariton of an infinite solid which has the combined properties of lattice vibration and electromagnetic wave

[75, 106].

An analogous solution exists for finite-sized particles, although the frequencies of oscillation and the form of the solution will now depend on the specific geometry. We consider the general problem of a finite-sized spherical particle of radius a and dielectric constant $\epsilon_i(\omega)$ given by Eq. A.2 embedded in a dielectric host ϵ_h which is assumed constant. The solution taking into account retardation for an arbitrary dielectric function has been given by Mie [92, 107, 108, 109]. Due to the spherical geometry, plane waves are no longer the modes of the problem. The fields must again satisfy the full set of four Maxwell equations as well as Eq. 4.24. Three independent and complete vector solutions to Eq. 4.24 for arbitrary ϵ_i can be constructed from the solutions of the corresponding scalar equation,

$$\nabla^2\psi + k^2\psi = 0, \tag{4.26}$$

which are

$$\psi_{lm} = z_l(kr)Y_{lm}(\theta,\phi), \quad l = 1, 2, ..; \quad m = 0, \pm 1, .., \pm l, \tag{4.27}$$

where $z_l(kr)$ stands for the spherical Bessel function $j_l(kr)$ inside the sphere, or the Hankel function $h_l(kr)$ which applies outside of the sphere. The Y_{lm} are the usual spherical harmonics. The three solutions of Eq. 4.24 are:

$$\mathbf{L}_{lm} = \nabla\psi_{lm}, \tag{4.28}$$

$$\mathbf{M}_{lm} = \nabla \times (\mathbf{r}\psi_{lm}) = \mathbf{L}_{lm} \times \mathbf{r}, \tag{4.29}$$

$$\mathbf{N}_{lm} = k^{-1}\nabla \times \mathbf{M}_{lm}, \tag{4.30}$$

which are also related by $\mathbf{M}_{lm} = k^{-1}\nabla \times \mathbf{N}_{lm}$. The full solution again separates into longitudinal and transverse parts. The longitudinal solution is $\mathbf{E} = A_{lm}\mathbf{L}_{lm}$ which

satisfies $\nabla \times \mathbf{E} = 0$ and exists only for $\epsilon(\omega_L) = 0$ corresponding to the longitudinal natural frequency. The fields $\mathbf{F}$ for $r > a$ are all zero and $\mathbf{H} = 0$ everywhere. Inside the sphere, the electric field is arbitrary and determined by the initial conditions, with the restriction that the boundary conditions for the tangential and normal field components must be satisfied at $r = a$, which leads to the requirement that $j_l(ka) = 0$ from which the allowed spatial frequencies k_n can be determined. This solution is not observed experimentally since it does not couple to external fields.

For the case of transverse solutions, k is given by $k_i = \sqrt{\epsilon_i(\omega)}\omega/c$ for $r < a$ and $k_o = \sqrt{\epsilon_h}\omega/c$ for $r > a$. The transverse modes split into two independent components–the transverse-electric (TE), $\mathbf{E} = B_{lm}\mathbf{M}_{lm}$ and the transverse-magnetic (TM), $\mathbf{E} = C_{lm}\mathbf{N}_{lm}$. The associated magnetic fields are found from $\mathbf{H} = (c/i\omega)\nabla \times \mathbf{E}$. Both the TE and the TM modes satisfy $\nabla \cdot \mathbf{E} = 0$, which characterizes the transverse solution. Thus for each pair of l, m we have two unknowns inside and outside of the sphere: B^i_{lm},B^o_{lm} for the TE modes and C^i_{lm},C^o_{lm} for the TM modes. These unknowns may be found by imposing the continuity conditions at $r = a$, where it is sufficient to consider just the tangential field components. For the TE case we get,

$$B^i_{lm} j_l(k_i a) = B^o_{lm} h_l(k_o a) \tag{4.31}$$

$$B^i_{lm}\sqrt{\epsilon_i(\omega)}[k_i a j_l(k_i a)]'/k_i a = B^o_{lm}\sqrt{\epsilon_h}[k_o a h_l(k_o a)]'/k_o a \tag{4.32}$$

where the prime denotes differentiation with respect to the argument, ka. By setting the determinant for the system of Eqs. 4.31, 4.32 equal to zero we obtain,

$$j_l(k_i a)[k_o a h_l(k_o a)]' - h_l(k_o a)[k_i a j_l(k_i a)]' = 0, \tag{4.33}$$

which is the characteristic equation for the TE phonon-polaritons of a sphere. This equation yields the natural frequencies of oscillation for which non-trivial field solu-

tions exist without an applied external field.

Similarly for the TM case, we obtain the two equations for the coefficients C^i_{lm}, C^o_{lm} from the boundary conditions at $r = a$,

$$C^i_{lm}\sqrt{\epsilon_i(\omega)}j_l(k_i a) = C^o_{lm}\sqrt{\epsilon_h}h_l(k_o a) \tag{4.34}$$

$$C^i_{lm}[k_i a j_l(k_i a)]'/k_i a = C^o_{lm}[k_o a h_l(k_o a)]'/k_o a \tag{4.35}$$

from which follows the characteristic equation for the TM resonances,

$$\epsilon_h h_l(k_o a)[k_i a j_l(k_i a)]' - \epsilon_i(\omega) j_l(k_i a)[k_o a h_l(k_o a)]' = 0. \tag{4.36}$$

To relate this to the quasi-static derivation of Section 4.7.1, we can take Eqs. 4.33, 4.36 in the limit $k_i a, k_o a << 1$. We use the Hankel and Bessel function approximations for small arguments: $j_l(x) \sim x^l$, $h_l(x) \sim x^{-(l+1)}$. In this approximation, there are no solutions for the TE case and the TM case becomes,

$$\epsilon_i(\omega) = -\epsilon_h(l+1)/l, \quad l = 1, 2, 3... \tag{4.37}$$

Thus we see resonances corresponding to the multipolar order of the field solutions, which are known as surface modes because the field profiles for the higher order terms are confined to the surface of the sphere. The $l = 0$ term corresponding to the monopole is absent due to the absence of net charge inside. The dipolar case yields $\epsilon_i(\omega) = -2\epsilon_h$ which is the condition we derived using the electrostatic approximation and is the single particle feature that we observe in reflectance at $\sim$260 cm^{-1}. The higher order resonances also exist, however, in the case of a constant external field they will not be excited.

For the general case of arbitrary sphere size [109], Eqs 4.33 and 4.36 describe three types of resonances: low frequency modes (LFM) which occur at $\omega < \omega_T$,

surface modes (SM) in the range of negative permittivity, $\omega_T < \omega < \omega_L$, and high frequency modes (HFM) at $\omega > \omega_L$. The LFM and HFM are bulk modes that vanish for small sphere size. In the limit $k_i a, k_o a << 1$, the LFM mode frequencies approach $\omega_{LFM} \to \omega_T$ whereas the frequencies of the HFM modes diverge $\omega_{HFM} \to \infty$. As the particle size increases all three types of modes shift to low frequencies and become mixed. Thus the three strict frequency ranges for LFM, SM, HFM apply only in the small particle limit.

In order to understand how these resonances enter the parameters observed in a typical experiment such as absorption and scattering, we must add an excitation field, which in this case is an incident plane wave [91, 108]. The incident plane wave is decomposed into spherical vector harmonics to match the geometry of the problem, and the continuity conditions at $r = a$ allow solution for the full set of incident, internal and scattered fields. Then using Poynting's theorem it is possible to solve for the amount of power that is taken from the incident wave by absorption and scattering, with total extinction being the sum of the two. In terms of the powers, P_{abs}, P_{sca}, P_{ext}, one can define the corresponding coefficients $\sigma_s = P_{sca}/(\pi a^2 I_{inc})$, $\sigma_a = P_{abs}/(\pi a^2 I_{inc})$ and $\sigma_e = P_{ext}/(\pi a^2 I_{inc})$, where I_{inc} is the incident intensity in the plane wave. The final expressions for the cross sections of scattering, extinction and absorption are given by,

$$\sigma_s = \frac{2}{(k_o R)^2} \sum_{l=1}^{\infty} (2l+1)(|a_l|^2 + |b_l|^2) \tag{4.38}$$

$$\sigma_e = -\frac{2}{(k_o R)^2} \sum_{l=1}^{\infty} (2l+1)\mathrm{Re}(|a_l| + |b_l|) \tag{4.39}$$

$$\sigma_a = \sigma_e - \sigma_s. \tag{4.40}$$

They are expressed in terms of a_l and b_l which are the Mie coefficients of the scattered

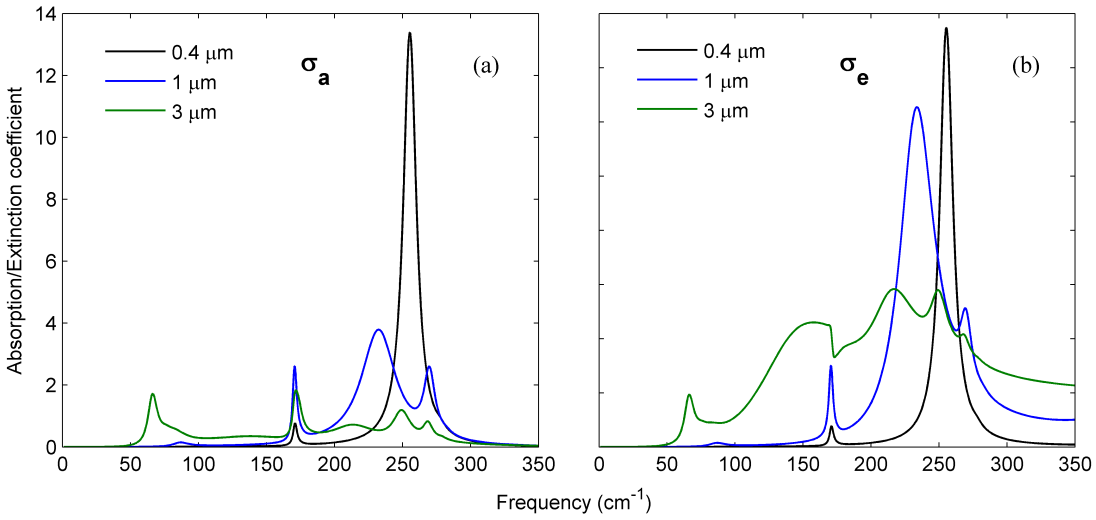

Figure 4.28: The coefficients of (a) absorption and (b) extinction for a spherical inclusion of $SrTiO_3$ of varying radius embedded in NiO host at T= 295 K. The dielectric constant of NiO is taken to be real which is a good approximation up to 350 cm^{-1}.

field for the $\mathbf{M}_{lm}$ and $\mathbf{N}_{lm}$, respectively, and are given by

$$a_l = -\frac{j_l(k_i a)[k_o a j_l(k_o a)]' - j_l(k_o a)[k_i a j_l(k_i a)]'}{j_l(k_i a)[k_o a h_l(k_o a)]' - h_l(k_o a)[k_i a j_l(k_i a)]'} \tag{4.41}$$

$$b_l = -\frac{\epsilon_h j_l(k_o a)[k_i a j_l(k_i a)]' - \epsilon_i(\omega) j_l(k_i a)[k_o a j_l(k_o a)]'}{\epsilon_h h_l(k_o a)[k_i a j_l(k_i a)]' - \epsilon_i(\omega) j_l(k_i a)[k_o a h_l(k_o a)]'}. \tag{4.42}$$

We plot the absorption and extinction coefficient for an STO sphere of different radii embedded in NiO in Fig. 4.28. For a radius of 0.4 μm which is approximately the mean size of the individual particles, the spectrum is dominated by the dipolar surface mode, with all of the power being lost to absorption inside the the sphere. As the particle size increases, the mode shifts toward lower frequencies and broadens. There is another peak that appears at $\sim$90 cm^{-1} for the 1 μm radius, increasing and shifting to lower frequencies with increasing particle size. This is the LFM bulk mode discussed above. Finally, a big fraction of the energy goes into scattering, which in the composite medium will differ from the behavior of individual particles due to interference.

The main size-dependent property that relates to our data is that with increasing particle or cluster size we expect to see additional bulk modes at or below the TO soft-mode frequency for a given temperature. We will also see the entire band between the TO and LO frequencies of the STO soft mode shift down in frequency. We believe we observe this behavior in the 15% in reflection of Fig. 4.13, where the low frequency feature shows dependence on inclusion concentration. For larger inclusion fractions, the STO particles form large clusters on the order of 2 μm (effective volume radius as compared to Fig. 4.28) which lead to the downshifting of the spectrum and possible appearance of bulk modes.

4.10 Summary

We have conducted detailed measurements and developed a model to describe the nano-particle behavior of STO inclusions embedded in NiO, in ceramic composites. The spectral features are dominated by the vibrational surface polaritons of the inclusion in a broad region of negative permittivity. Specifically, we see two dominant features: the Fröhlich mode at 260 cm^{-1} due to the nearly spherically shaped inclusions as well as a broad band in between the temperature dependent soft mode frequency and up to 500 cm^{-1}. At the onset of this band, we see a characteristic reflectance feature at low frequencies which is temperature dependent. The broadening and up-shifting of the bulk soft mode into a wide band leads to a drastic reduction in the values of static permittivity of the composite as measured at low frequencies as well as the vanishing of the reststrahlen region in reflection. Based on the analysis of inclusion fraction, it is possible to identify the effect of clustering and information about cluster size from the optical spectral features. The Fröhlich mode represents a well defined single-particle geometric resonance of the otherwise random composite which opens the way for structural engineering of ceramics for attaining desired spectral characteristics.

CHAPTER V

Conclusion

As is customary in the concluding chapter, we will present unique features and strengths of the findings of this dissertation as well as pose new questions that may be answered in future investigations. After having worked for a long time in a particular direction, one often discovers that the answers that were found are small in comparison to the number of additional questions that spring up on the basis of newly gained understanding. This was also true in this case and the findings of the previous chapters suggest new questions and research directions.

In the process of this dissertation we have found a method to extend the limited bandwidth of THz-TDS spectroscopy which often stops at frequencies below 5 THz, thereby limiting the range of investigation and the choices of materials that may be studied. The optimization of the time-domain spectrometer in the 5-8 THz range was motivated in large part by the interesting materials that we found that were outside of our previously accessible measurement range. As was mentioned before in the section on the NiO-STO composites where data was presented on the magnetic AFMR resonance of NiO, THz-TDS has unique advantages compared to incoherent measurement methods first because it allows measurement of both amplitude and phase which leads to the full optical constants directly as shown in Fig. 4.30 as opposed to performing a fit to the reflection or transmission data which relies on an

assumed model for the optical constants such as the single harmonic oscillator model. In FTIR studies, the approach to accomplish the same goal would be to employ Kramers-Kronig analysis for obtaining the phase information which is related to the amplitude, however this approach requires measurement in very wide frequency ranges and the joining of multiple data sets which is difficult to do in practice. Thus the direct extraction of the optical constants from the amplitude and phase information without making model assumptions is quite useful. The second advantage is in the resolution of the instrument which, in principle, is limited only by the temporal window of the scan. In practice, increasing temporal window will extend the duration of the scan and thus introduce additional noise which will eventually overwhelm the signal. In the case of FTIR, the resolution of the frequency domain measurement will depend on the mirror retardation of the interferometer in which case noise will also increase with resolution. In the end, the resolution of both methods will be limited by SNR and in this regard THz-TDS is known to have a significant advantage at lower frequencies. The bound on the resolution of data in Fig. 4.3 was determined by the 30 ps time window of the scan. By extending the temporal window to ~ 60 ps, we were able to see pronounced narrowing of the AFMR of NiO. Fig. 5.1 shows the transmission of 1.85 mm pure NiO ceramic at two temperature points with the higher resolution.

Although the narrowing is significant with temperature, and the width of the $T = 50$ K data may be limited by the temporal resolution of the instrument which in this case is ~ 0.6 cm^{-1}, it is unlikely that the value of μ would become stronger by greater than two orders of magnitude so that the magnetic permeability could attain negative values as is required based on the harmonic oscillator fit of Fig. 4.4. Regardless of the final answer to this question, the ultimate sharpness of the linewidth of the NiO AFMR is a fundamental question that would be interesting to investigate in its own right. However, with regard to the goal of searching for naturally occurring negative refraction there are other material candidates in the group of transition-

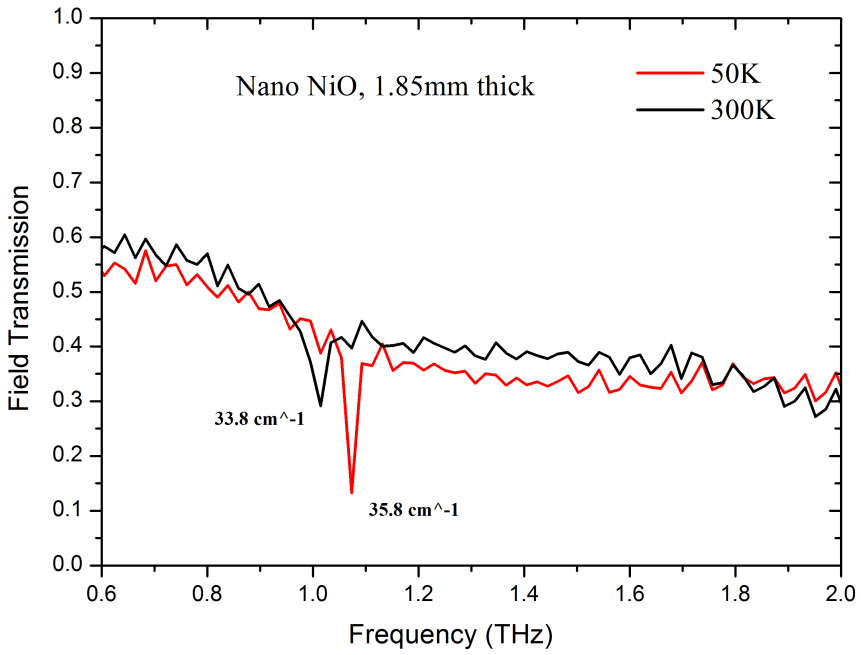

Figure 5.1: Transmission of the nano-grain NiO ceramic 1.85 mm thick taken at two temperature points. The temporal window of the scan is 55 ps.

metal fluorides that possess even stronger magnetic-dipole active spin wave resonances in the far-infrared range, the most promising of which to our knowledge is Cobalt Fluoride (CoF_2). An early far-infrared [110] study using FTIR technique measured the reflection of CoF_2 in the range of 100-300 cm^{-1} as is reproduced in Fig. 5.2.

The most noteworthy feature of this measurement is that the dip in reflectance corresponding to the magnetic mode occurs in the reststrahlen region of the vibrational mode of CoF_2 where the permittivity is negative to begin with as was pointed out by the author of the paper almost twenty years prior to Pendry's proposal of the perfect lens [16] that instigated the intensive research in this area and led to the eventual understanding of negative refraction. However, at the time of this measurement the understanding did not exist and the exact value of the magnetic permeability was not determined. Based on a fit to this data, the oscillator strength of the magnetic mode at 210 cm^{-1} is significantly larger in comparison to the NiO AFMR resonance which makes this an appealing candidate especially taking into account the fact that a composite material would not need to be fabricated for the sake of the electric permittivity. The THz time-domain technique, which is capable of scanning in the required frequency range, would also be advantageous for resolving the linewidth of this mode at lower temperatures.

With regard to the dielectric properties of STO composites, it was shown that the single-particle Fröhlich mode stands out in an otherwise arbitrary composite due to the fact that the initial inclusion geometry was nearly spherical. Although the spherical mode was far-removed from any magnetic behavior of NiO, it may be possible to engineer the spectral features of such composites to match the magnetic resonances of other materials, such as CoF_2, for instance. According to [110] CoF_2 also has a low frequency magnon at 40 cm^{-1} as well as a two-magnon magnetic-dipole resonance at 120 cm^{-1}. Thus, with a more careful fabrication of ceramics that emphasize elongated shapes of inclusion, it would be possible to shift the Fröhlich resonance to lower

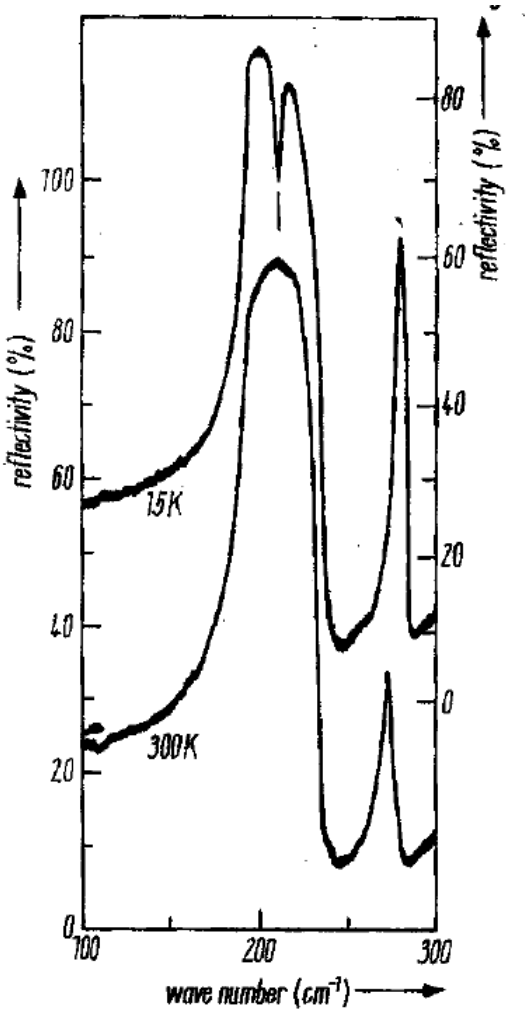

Figure 5.2: Observation of the magnetic dipole infrared active exciton in CoF_2 at (210±1) cm^{-1}. The magnetic field vector **H** is directed parallel to the optical axis c of the crystal, the electric field vector **E** is perpendicular to it. The left ordinate scale corresponds to the spectrum measured at 300 K, the right scale to that at 15 K. Angle of incidence α =40° , resolution 1.5 cm^{-1}. Taken from [110].

frequencies in order to overlap the magnetic features. There are a number of other antiferromagnets that may be used in place of NiO, with a good starting-point compilation in connection to NIM given in [111]. With regard to the dielectric resonance, it was found that only a small fraction of the total inclusion concentration, 1/20-th of the total, was responsible for the single particle resonance due to the strong clustering and interaction effects that resulted in a dominant wide band across the entire region of negative permittivity. With the engineering of ceramics or more careful selection of initial powder shape it may be possible to focus the spectral features into much narrower regions.

Finally, as a suggestion for an alternative metamaterial application, the reverse case of interpreting the topology and information about the internal statistical order may be done for resonant composites based on simple reflectance and transmittance measurements. There were a number of geometry and statistical features that we obtained from the experiments. Namely, that the fraction of interacting STO particles that lead to the broad absorption band relative to the isolated inclusions that cause the single particle feature is on the order of 20:1. Information regarding the statistical deviation from spherical shape of the starting inclusion particles is contained in the width of the Fröhlich mode. We derived information about the mean STO cluster size being on the order of 2 μm (effective volume radius) based on SEM images as well as the spectral behavior of the low frequency onset of the absorption band which depends on the particle size through the total inclusion fraction. Such information may be especially relevant in studying fracture formation and stress resistance that may depend on the homogeneity of the composite. Inclusions of resonant particles such as STO may be added to composites and mixtures intended for entirely different applications as an indicator for optical testing purposes.

APPENDICES

APPENDIX A

Effective medium theories

In the current section we cover several important aspects regarding composites of arbitrary microstructure with an emphasis on resonant ionic inclusions at low filling fractions. Without using any information about the specific arrangement of inclusions we show that a general mixture will have: 1) Upper and lower bounds for the effective dielectric constant with the exact dielectric value being determined by geometry. In the case of resonant inclusions, these bounds transform into bounds in frequency within which the effective resonance must occur. 2) A general representation for the effective dielectric function in terms of electrostatic resonance states, called the Bergman spectral representation. The specific geometry will determine the location of the poles and, as a result, the excitation frequencies of the composite within the region of negative permittivity as is the case for plasmonic structures. In Section 4.6 and Appendix B we will consider a more specific geometry based on the generalized Clausius-Mosotti equation which will behave within the limits of the general rules.

A.1 Bounds for arbitrary mixtures

The averaging approach that we used earlier (Eq. 4.3) is the simplest way of approximating an effective medium which also corresponds to an exact solution of

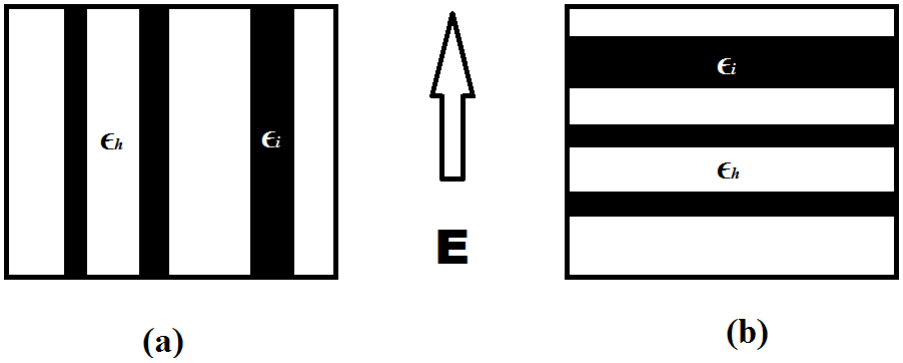

Figure A.1: Two component structure with layers (a) parallel and (b) perpendicular to the electric field.

the well known geometry of a stack of thin films parallel to the electric field in the quasi-static approximation [79, 80]. Consider two cases as shown in Fig. A.1 where the electric field is oriented either (a) parallel or (b) perpendicular to the component layers. This geometry is analogous to the problem of parallel-plate capacitors where the measurable effective capacitance can be used as the physical basis to define the effective dielectric constant [81]. It is assumed here that the scale of the structure is smaller than the wavelength of light as well as skin depths inside the component materials, such that the full set of Maxwell equations reduces to electrostatics. In the parallel case, $\mathbf{E}(\mathbf{r}) = \mathbf{E}$ is uniform throughout and $\mathbf{D}(\mathbf{r}) = \epsilon(\mathbf{r})\mathbf{E}$, whereas in the perpendicular case, $\mathbf{D}(\mathbf{r}) = \mathbf{D}$ is uniform and $\mathbf{E}(\mathbf{r}) = \mathbf{D}/\epsilon(\mathbf{r})$. Thus, the fields of the system are known exactly and it is possible to calculate the averages $< \mathbf{E}(\mathbf{r}) >$, $< \mathbf{D}(\mathbf{r}) >$ by using $\epsilon(\mathbf{r}) = \epsilon_i$ or ϵ_h and the corresponding volume fractions of each component. This results in the effective dielectric constant defined by $\epsilon_{eff} = < \mathbf{D}(\mathbf{r}) > / < \mathbf{E}(\mathbf{r}) >$ for the two configurations as follows,

$$\begin{aligned} \epsilon_{\parallel} &= f\epsilon_i + (1-f)\epsilon_h \\ \frac{1}{\epsilon_{\perp}} &= \frac{f}{\epsilon_i} + \frac{(1-f)}{\epsilon_h} \end{aligned} \tag{A.1}$$

In the case of a highly contrasting mixture where $\epsilon_i >> \epsilon_h$, case (a) will assume the properties of the inclusion in proportion to the volume fraction, whereas case

(b) will be resistant to acquire the high dielectric value of the inclusion even for high volume fractions. This is because in the parallel configuration there will be minimum screening (depolarization field) in the highly polarizable inclusion, but the perpendicular case will experience maximum screening such that the electric field inside the inclusion is reduced thereby diminishing the effect of the inclusion on the average dielectric constant [82, 79].

Because case (a) represents minimum screening and case (b) maximum screening, one can imagine that most randomly structured composites will fall somewhere in between. Indeed, Eq. A.1 represents two extreme bounds on the effective dielectric constant of a mixture with arbitrary topology, known as the Wiener bounds [80, 83]. The component dielectric constants may be complex as long as the effective medium is well defined, in which case Eq. A.1 results in a bounded region in the complex plane. Thus, if the dielectric properties of the inclusion and host are known, one can find a range of values within which the effective dielectric constant must lie. If the exact volume fractions are known, the allowed range is reduced significantly. By adding additional information regarding the microstructure, such as the presence of isotropy, it is possible to narrow this range even more with stricter bounds [80, 83].

If we consider resonant inclusions of STO inside NiO for the two extreme geometries of Eq. A.1, we can get a sense of the range of behavior within which our composite must fall. We take a 10% volume fraction of STO inclusions inside NiO at room temperature. In the parallel case, the situation is as expected with weighted average mixing, but in the perpendicular case the location of STO soft mode shifts up in frequency to 480 cm^{-1} in addition to experiencing a reduction in magnitude. This is due to the fact that the poles of the effective dielectric function are altered in case (b), as seen in Eq. A.1. To simplify the analysis, we consider an ionic inclusion

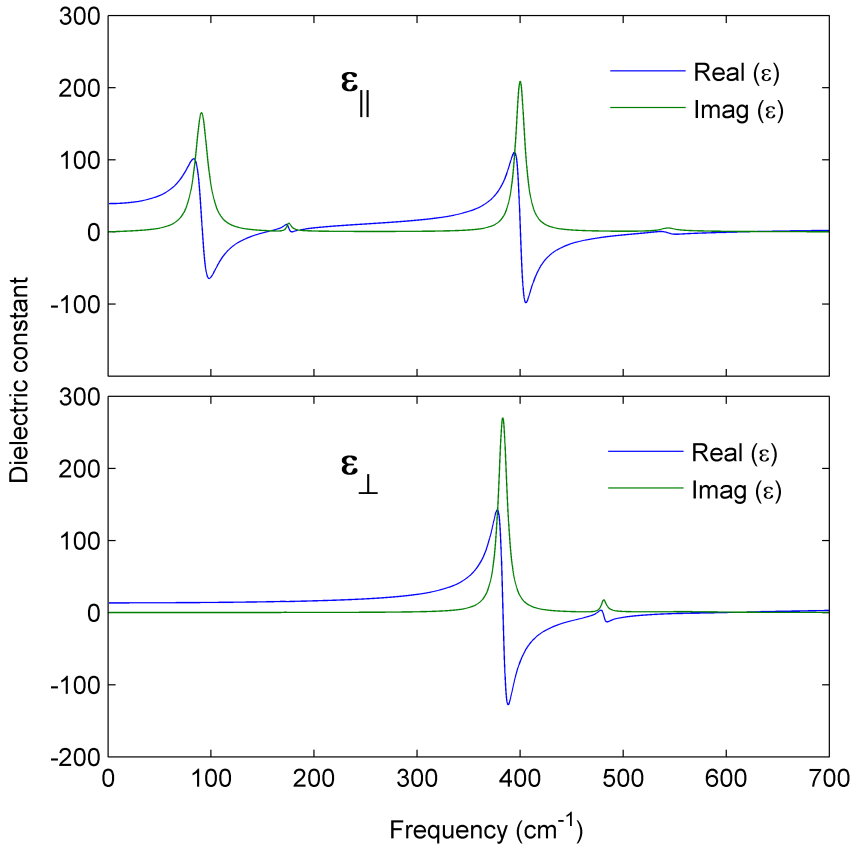

Figure A.2: Effective dielectric constant for the parallel and perpendicular thin-film configurations of the 90-10 mixture.

with a single infrared mode which has a dielectric function of the form [75, Ch. 10],

$$\epsilon_i(\omega) = \epsilon_\infty + (\epsilon_0 - \epsilon_\infty)\frac{{\omega_T}^2}{({\omega_T}^2 - \omega^2)} \tag{A.2}$$

where ω_T, ω_L are the zone-center transverse, longitudinal optical frequencies, respectively, and ϵ_0, ϵ_∞ are the static and electronic contributions to the dielectric constant. The four quantities are related by the Lyddane-Sachs-Teller relation, ${\omega_L}^2\epsilon_\infty = {\omega_T}^2\epsilon_0$. We take the host medium, ϵ_h, to be constant. Then Eq A.1 becomes,

$$\begin{aligned} \epsilon_\parallel &= [f\epsilon_\infty + (1-f)\epsilon_h] + f(\epsilon_0 - \epsilon_\infty)\tfrac{{\omega_T}^2}{({\omega_T}^2 - \omega^2)} \\ \epsilon_\perp &= \tfrac{\epsilon_h}{f\frac{\epsilon_h}{\epsilon_i} + (1-f)} \end{aligned} \tag{A.3}$$

The pole of $\epsilon_{\parallel}$ remains unchanged at $\omega_{\parallel} = \omega_T$ and for $\epsilon_{\perp}$ the new pole becomes,

$$\omega_{\perp} = \omega_T \sqrt{\frac{\epsilon_0 + \epsilon_h f/(1-f)}{\epsilon_\infty + \epsilon_h f/(1-f)}}, \tag{A.4}$$

which is restricted to the region, $\omega_T \leq \omega_{\perp} \leq \omega_L$. In the limit $f \to 0$, $\omega_{\perp} = \omega_T \sqrt{\epsilon_0/\epsilon_\infty} = \omega_L$. Thus the inclusion vibrational TO mode shifts toward the LO frequency for low mixing fractions as seen in Fig. A.2. For the case of $SrTiO_3$, which has three active infrared modes, the situation does not change significantly due to the fact the the soft mode is dominant.

A.2 The Bergman spectral representation

A more general way to understand the shifting of poles is to consider a composite of arbitrary geometry of which the above structures are special cases. The dielectric constant of an arbitrary effective medium can be represented in terms of a spectrum of electrostatic resonances that depend on the microgeometry and appear as poles in the effective dielectric function [81, 84]. Using the Bergman representation, the dielectric constant of an arbitrary mixture can be expressed as,

$$\epsilon_{eff} = \epsilon_h (1 - \sum_n \frac{F_n}{s - s_n}) \tag{A.5}$$

where

$$s = \frac{\epsilon_h}{\epsilon_h - \epsilon_i}, \quad 0 \leq s_n < 1, \quad 0 \leq F_n < 1. \tag{A.6}$$

This expression results from the fact that for a given composite microgeometry there exists a set of non-vanishing potentials ϕ_n that solve the Laplace equation with the corresponding boundary conditions. Since the electric field associated with these states is non-zero for a zero external field, the solutions are known as electrostatic resonances. Moreover, these resonant states form a complete and orthogonal set

of functions that can be used to describe an arbitrary electric field $\mathbf{E}(\mathbf{r})$ inside the composite. Since $\epsilon_{eff} =< \epsilon(\mathbf{r})\mathbf{E}(\mathbf{r}) > / < \mathbf{E}(\mathbf{r}) >$, there exists a general expansion of the effective dielectric constant in terms of these resonances once the necessary averaging has been applied. The structural information particular to the composite, including the filling fraction, determines the values of F_n, s_n. The poles of ϵ_{eff} can only occur for negative values of ϵ_i/ϵ_h and are thus dispersive (non-zero frequency) phenomena. The values of the poles determine the natural frequencies of the system through the dependence of the component dielectric constant on frequency. Here, we are not concerned with the theory of electrostatic resonances of arbitrary composites, which we leave to the references, but our interest is mainly in pointing out that such resonances exist, that they depend on the geometry, and that they are responsible for the general representation of the dielectric function as given by Eqs. A.5 and A.6. In Chapter 4 and Appendix B, we will deal in detail with the electrostatic resonances of specific geometries, such as the sphere and the ellipsoid, which are present in our samples and ultimately determine the resonant spectral features that we see.

For now we consider again the frequency dependent form of the dielectric constant of an ionic inclusion with a single vibrational mode as given by Eq. A.2. If such an inclusion is mixed in an arbitrary fashion into a host material with a static dielectric constant, ϵ_h, then the resonant frequencies must satisfy the pole condition of Eq. A.5,

$$\epsilon_i(\omega_n) = -\epsilon_h(1/s_n - 1), \tag{A.7}$$

which is satisfied only for negative values of $\epsilon_i(\omega)$. Thus for any type of system the resonance region will occur between $\omega_T \leq \omega_n < \omega_L$. The specific locations within this range will be determined by the geometry. We have already presented several special cases of the Bergman spectral representation in Fig A.1 and have solved for the resonant spectra. The parallel and perpendicular thin-film configurations, which

correspond to extreme bounds of the dielectric constant, also represent the extremes of pole behavior for the case of an ionic inclusion present at low filling fractions. The parallel layers will be associated with a resonance at the transverse-optical frequency whereas the perpendicular configuration of maximal field screening will shift the ionic resonance toward the longitudinal-optical frequency. Other features which occur in the middle of this range such as the surface modes of a spherical dielectric inclusion will be dealt with in Chapter 4.

APPENDIX B

The Maxwell-Garnett formula

In Section 4.6, the CM relation was derived which constructs a continuous, macroscopic medium out of a suspension of point dipoles. The density, n, and polarizability, α are the building blocks used to derive the macroscopic $< \mathbf{E} >$, $< \mathbf{P} >$ and the dielectric constant, ϵ_{eff}, for an arbitrary applied field. The symmetry of the medium eliminates interaction between the dipoles such that any one of them is excited by $\mathbf{E}_{loc} = \mathbf{E}_{int}$. In the macroscopic sense, each of the dipoles contributes a depolarizing "self-field" coming from within the dipole, which follows from Eq. 4.16, that results in a smaller $< \mathbf{E} >$ compared to $\mathbf{E}_{int}$ as seen from Eq. 4.17 [82, 87]. The CM equation has been experimentally confirmed and used to estimate the polarizabilities of atoms and ions from measurements of the refractive index of crystals, liquids and gases. Note, that the noncrystalline substances do not have cubic symmetry which has been assumed during the derivation of the local field, but the Lorentz relation is expected to hold as well for uncorrelated systems [86], [88, Ch. 2] where the surrounding particle interactions tend to average to zero at any inclusion site. Note also that the Lorentz field has been derived for point dipoles, whereas the atoms making up the solid have finite sizes and are relatively close-packed such that the far-field requirement for the applicability of the dipole approximation is not satisfied in gen-

eral. However, if the atoms or ions are assumed to be perfectly spherical then the electric potential outside of the sphere, within the statics approximation, is described solely by the point dipole potential and the atom behaves like a dipole at arbitrary separations. We will treat this problem in more detail in this section. Thus the main corrections to the CM equation will come from the removal of symmetry of either the lattice or the inclusion geometry which will lead to more complicated local exciting fields and higher multipole interactions. These problems have been studied theoretically for the case of ionic crystals with up to octupole order corrections and for finite-sized spherical metal inclusions in different lattice types and the agreement with the basic CM relation has been found quite accurate [89, 90]. Moreover, in the case of uncorrelated systems of inclusions, even irregularly shaped particles are not expected to cause significant deviations from CM results as long as the quasi-static approximation applies and the inclusions are well separated from each other such that the dipole fields are the dominant terms in the expansion.

In this section we will consider media with finite-sized, dilute systems of inclusions that are significantly smaller than the wavelength of light. First let us consider a medium with spherical inclusions of radius a, and volume fraction, f, mixed into a uniform host material. Assuming that the inclusions are well distributed, the volume taken by one particle is $(4/3)\pi a^3/f$ and the average inter-particle separation normalized by the radius of the particle can be estimated by:

$$S_{avg} = \frac{[(4/3)\pi a^3/f]^{1/3}}{a} = (\frac{4\pi}{3f})^{1/3}. \tag{B.1}$$

Thus for an inclusion volume fraction of $f = 0.1$, $S_{avg} = 3.5$ radii, if the particles are uniformly distributed.

Now we will derive the ϵ_{eff} for a medium with finite-sized spherical inclusions. Consider a sphere in free space, of dielectric constant ϵ_i, in a static electric field, $\mathbf{E}_0$,

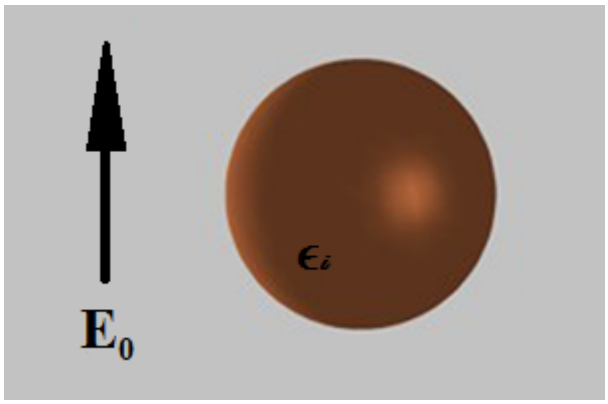

Figure B.1: Schematic of a sphere of dielectric constant ϵ_i being polarized by a uniform external field $\mathbf{E}_0$.

as shown in Fig. B.1. The external field will polarize the sphere and induce charges on the surface which will act to counter the external field. From symmetry, we can see that the internal fields and polarization must be parallel to $\mathbf{E}_0$. The standard statics solution [85, 91] proceeds by solving the Laplace's equation $\nabla^2\Phi = 0$ in the charge free regions, $r < a$, where the potential can be expressed as $\Phi_i = A_l r^l P_l(\cos\theta)$ and for $r > a$, where the potential is $\Phi_o = -E_0 r\cos\theta + B_l r^{-(l+1)} P_l(\cos\theta)$. The $P_l(x)$ are the Legendre polynomials. The boundary conditions at $r = a$ allow solution for the unknown coefficients. The internal electric field is found in terms of the applied field,

$$\mathbf{E}_{in} = \frac{3}{\epsilon_i + 2}\mathbf{E}_0. \tag{B.2}$$

Note that the denominator contains a pole, $\epsilon_i = -2$, which corresponds to a resonance condition for the spherical geometry. At this value of ϵ_i a nontrivial solution to the Laplace equation exists for a vanishing external field [92, 93], which represents one possible electrostatic resonance within the Bergman spectral representation as discussed in Appendix A. The polarization inside the sphere is $\mathbf{P} = \epsilon_0(\epsilon_i - 1)\mathbf{E}_{in}$ and the static polarizability is obtained from $\mathbf{p}_{in} = \alpha\mathbf{E}_0$ as follows,

$$\alpha_{sphere} = 4\pi a^3 \epsilon_0 \frac{\epsilon_i - 1}{\epsilon_i + 2}. \tag{B.3}$$

Now, considering a mixture of i different spheres of dielectric constants ϵ_i, polarizabilities α_i and volume fractions $f_i = n_i(4/3)\pi a^3$, we get the effective medium constant in the quasi-static approximation from Eq. 4.19,

$$\frac{\epsilon_{eff} - 1}{\epsilon_{eff} + 2} = \sum_i f_i(\frac{\epsilon_i - 1}{\epsilon_i + 2}), \tag{B.4}$$

which is the CM result modified to include finite spheres. We are interested in inclusions located in a host background ϵ_h which requires the following substitutions $\epsilon_{eff} \rightarrow \frac{\epsilon_{eff}}{\epsilon_h}$ and $\epsilon_i \rightarrow \frac{\epsilon_i}{\epsilon_h}$. This results from the fact that for an arbitrary composite geometry, the solution of the Laplace equation for the electric potential in all space is identical for the inclusion/host pairs $\{\epsilon_i,\epsilon_h\}$ and $\{\epsilon_i/\epsilon_h,1\}$. This produces identical $\mathbf{E}$ field for the two cases, but the displacement field is modified $\mathbf{D} \rightarrow \mathbf{D}/\epsilon_h$ from the case $\{\epsilon_i,\epsilon_h\}$ to $\{\epsilon_i/\epsilon_h,1\}$. Since $\epsilon_{eff} =< \mathbf{D} > / < \mathbf{E} >$ then ϵ_{eff} also requires the appropriate substitution. Carrying out the change and re-arranging for ϵ_{eff} results in,

$$\epsilon_{eff} = \epsilon_h + 3\epsilon_h \frac{\sum_i f_i \frac{\epsilon_i - \epsilon_h}{\epsilon_i + 2\epsilon_h}}{1 - \sum_i f_i \frac{\epsilon_i - \epsilon_h}{\epsilon_i + 2\epsilon_h}}. \tag{B.5}$$

This is the well known Maxwell-Garnett (MG) formula for multi-phase mixtures [79].

In our experiments, we have samples that are composed of nearly spherical STO particles at low volume fractions which means that the particles are fairly well dispersed. However, a large fraction of the particles tends to cluster and form larger, irregularly shaped aggregates (see Figs. 2.10-2.14). As an approximation, we can view the mixture as a dilute suspension if spherical particles as well as larger particle aggregates of varying shapes that are fused together on sintering. The irregular agglomerates are difficult to simulate exactly and would require a scattering solution for each particular shape of which there are an infinite number or an entirely different statistical approach of generating such shapes from the constituent spheres by assuming some form for the spatial correlation function. These approaches are involved,

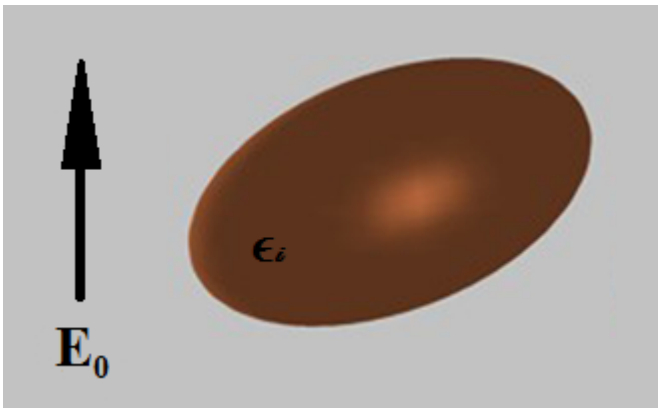

Figure B.2: Schematic of an ellipsoid of dielectric constant ϵ_i being polarized by a uniform external field $\mathbf{E}_0$.

would still be based on statistical assumptions and would not take advantage of the fact that we are dealing with a dilute CM type of mixture. For this reason, we will approximate the aggregated shapes by a range of ellipsoidal shapes of varying axial ratios for which exact solutions exist in the quasi-static limit. Thus we will model the mixture as made up of a fraction of well dispersed spheres corresponding to individual STO inclusions and ellipsoids which describe the clusters of varying geometries–from disks to needles and everything in between. The total volume fraction of the inclusion will be kept small in accordance with our samples. This should provide a reasonable first-order description of the random STO/NiO composites.

As was done for a sphere, it is possible to solve for the internal and external fields of a dielectric ellipsoid in an external static field. The approach is considerably more involved due to the loss of symmetry, such that the Laplace equation must be described in ellipsoidal coordinates for this problem [91, 94]. However, the approach of expressing the electric potential inside and outside of the object and matching the boundary conditions at the interface is analogous to the sphere. Again, the external field will polarize the ellipsoid and induce a constant internal electric field irrespective of the orientation although the field will not in general point in the same direction as the external field, unless aligned along one of the principal axes of the ellipsoid. Let

us take the principal axes to have half-lengths a_x, a_y, a_z. If $\mathbf{E}_0$ is aligned along one of these axes, such as $\hat{x}$, the internal field solution is,

$$\mathbf{E}_{in} = \frac{1}{1 + N_x(\epsilon_i - 1)}\mathbf{E}_0, \tag{B.6}$$

where N_x is the depolarization factor found from,

$$N_x = \frac{a_x a_y a_z}{2} \int_0^\infty \frac{ds}{(s + a_x^2)\sqrt{(s + a_x^2)(s + a_y^2)(s + a_z^2)}}. \tag{B.7}$$

The depolarization factors N_y (N_z) can be calculated similarly by interchanging a_y and a_x (a_z and a_x) in the integral. The three factors always satisfy $N_x + N_y + N_z = 1$ and for the case of a sphere $N_x = N_y = N_z = 1/3$, in which case Eq. B.6 leads to Eq. B.2. No closed form expression for Eq. B.7 exists for the general case of three different axes, however the depolarization factors may be expressed in terms of tabulated elliptic integrals [96] and simple equations exist for ellipsoids of revolution (spheroids) where two of the axes are equal [79]. From Eq. B.6, one can see that the ellipsoid will in general contain three poles $\epsilon_i = -(1/N_k - 1)$ for $k \in \{x, y, z\}$, which will lead to electrostatic resonances at the corresponding frequencies in the region of negative permittivity of the inclusion. The induced polarization will in general be anisotropic, with the dipole moment given by $\mathbf{p}_{in} = \sum_{k=x,y,z} \alpha_k(\hat{k} \cdot \mathbf{E}_0)\hat{k}$ and the polarizability derived as before,

$$\alpha_k = \frac{4\pi a_x a_y a_z}{3} \frac{\epsilon_0(\epsilon_i - 1)}{1 + N_k(\epsilon_i - 1)}. \tag{B.8}$$

Due to the polarization anisotropy, the CM relation must in general be expressed in vectorial form, however, since we are dealing with a random mixture where the orientation of the inclusions is uniformly distributed, the effective polarizability will be isotropic by symmetry. Thus we need to determine the magnitude of the isotropic

polarizability of an ellipsoid with a uniform probability density of orientation over 4π degrees of solid angle, Ω [91, Ch. 5]. We express the constant external field in spherical coordinates $\mathbf{E}_0 = E_0(\sin\theta\cos\phi, \sin\theta\sin\phi, \cos\theta)$ and assume that the frame of the ellipsoid rotates uniformly. To calculate the effective polarizability we calculate the contribution of each of the principal directions of polarization of the ellipsoid to the direction of the external field. Thus, taking the $\hat{z}$ component we get,

$$< \alpha_z >= \frac{\alpha_z}{4\pi} \int_0^{2\pi} \int_0^{\pi} \cos^2\theta \sin\theta \, d\theta \, d\phi = \frac{\alpha_z}{3}, \tag{B.9}$$

with the integrals for $< \alpha_x >$, $< \alpha_y >$ producing identical results. Thus the effective polarizability of a randomly oriented ellipsoid is,

$$\alpha_{ellipsoid} = \frac{1}{3}(\alpha_x + \alpha_y + \alpha_z). \tag{B.10}$$

In addition, the local field will be altered for the ellipsoidal inclusion due to the loss of spherical symmetry. In the derivation leading up to Eq. 4.17, the averaging of the electric field must be done over an ellipsoidal shell [94, 95] which leads to the modified Lorentz relation for electric field applied along one of the axes of the ellipsoid,

$$< \mathbf{E} >= \mathbf{E}_{loc} - \frac{N_k}{\epsilon_0} < \mathbf{P} >, \quad k = x, y, z \tag{B.11}$$

where N_k is the depolarization factor as defined previously. In the case of random orientation this relation will also be averaged in the three principal directions as derived for the polarizability. The final result for the effective dielectric constant of

a multi-phase mixture of finite-sized, randomly oriented ellipsoidal inclusions is [97],

$$\epsilon_{eff} = \epsilon_h + \frac{\frac{1}{3}\sum_i f_i(\epsilon_i - \epsilon_h)\sum_{k=1}^{3}\frac{\epsilon_h}{\epsilon_h + N_{ik}(\epsilon_i - \epsilon_h)}}{1 - \frac{1}{3}\sum_i f_i(\epsilon_i - \epsilon_h)\sum_{k=1}^{3}\frac{N_{ik}}{\epsilon_h + N_{ik}(\epsilon_i - \epsilon_h)}}. \tag{B.12}$$

We note that the spherical geometry as shown in Eq. B.5 is a subset of this more general formula.

BIBLIOGRAPHY

BIBLIOGRAPHY

[1] M. Tonouchi, Nat. Photonics **1**, 97 (2007).

[2] P. Y. Han, M. Tani, M. Usami, S. Kono, R. Kersting, and X.-C. Zhang, J. Appl. Phys. **89**, 2357 (2001).

[3] S. E. Ralph, S. Perkowitz, N. Katzenellenbogen, and D. Grischkowsky, J. Opt. Soc. Am. B **11**, 2528 (1994).

[4] J. Hebling, A. G. Stepanov, G. Almsi, B. Bartal, and J. Kuhl, Appl. Phys. B: Lasers Opt. **78**, 593 (2004).

[5] P. H. Bolivar, M. Brucherseifer, J. Gomez Rivas, R. Gonzalo, I. Ederra, A. L. Reynolds, M. Holker, and P. de Maagt, IEEE Trans. Microwave Theory Tech. **51**, 1062 (2003).

[6] S.A. Maier, *Plasmonics* (Springer, New York, 2007).

[7] J. A. Schuller, E. S. Barnard, W. S. Cai, Y. C. Yun, J. S. White, and M. L. Brongersma, Nat. Mater. **9**, 193 (2010).

[8] M.I. Stockman, Opt. Express **19**, 22029 (2011).

[9] R. Hillenbrand, T. Taubner, and F. Keilmann, Nature **418**, 159 (2002).

[10] W. Cai and V. Shalaev, *Optical Metamaterials: Fundamentals and Applications* (Springer, 2009).

[11] D. K. Gramotnev and S. I. Bozhevolnyi, Nat. Photonics **4**, 83 (2010).

[12] K. A. Willets and R. P. Van Duyne, Annu. Rev. Phys. Chem. **58**, 267 (2007).

[13] H. A. Atwater and A. Polman, Nat. Mater. **9**, 205 (2010).

[14] S.A. Ramakrishna, Rep. Prog. Phys. **68**, 449 (2005).

[15] V.G. Veselago, Sov. Phys. Usp. **10**, 509 (1968).

[16] J. B. Pendry, Phys. Rev. Lett. **85**, 3966 (2000).

[17] H.-T. Chen, J. F. O'Hara, A. K. Azad, and A. J. Taylor, Laser Photonics Rev. **5**, 513 (2011)

[18] D.R. Smith, W.J. Padilla, D.C. Vier, S.C. Nemat-Nasser, and S. Schultz, Phys. Rev. Lett. **84**, 4184 (2000).

[19] C. M. Soukoulis and M. Wegener, Nat. Photonics **5**, 523 (2011).

[20] T. J. Yen, W. J. Padilla, N. Fang, D. C. Vier, D. R. Smith, J. B. Pendry, D. N. Basov, and X. Zhang, Science **303**, 1494 (2004).

[21] C. Garcia-Meca, J. Hurtado, J. Marti, A. Martinez, W. Dickson, and A. V. Zayats, Phys. Rev. Lett. **106**, 067402 (2011).

[22] G. Dolling, M. Wegener, C.M. Soukoulis, and S. Linden, Opt. Lett. **32**, 53 (2007).

[23] S.D. Kirby, M. Lee, and R.B. van Dover, J. Phys. D: Appl. Phys. **40**, 1161 (2007).

[24] U. Keller, Nature **424**, 831 (2003).

[25] J.-C. Diels and W. Rudolph, *Ultrashort Laser Pulse Phenomena* (Academic Press, San Diego, 1996).

[26] A. M. Weiner, *Ultrafast Optics* (Wiley, 2009).

[27] *User's Manual Tsunami Model 3960 Laser* (Spectra-Physics, Inc., Mountain View, CA, 2002).

[28] J. Li, Ph.D. Dissertation, University of Michigan, 2012.

[29] W. Hayes and R. Loudon, *Scattering of Light by Crystals* (Wiley, New York, 1978).

[30] R. L. Fork, O. E. Martinez, and J. P. Gordon, Opt. Lett. **9**, 150 (1984).

[31] G. A. Garrett, Ph.D. Dissertation, University of Michigan, 2001.

[32] B. H. Kolner and D. M. Bloom, IEEE J. Quantum Electron. **QE-22**, 79 (1986).

[33] A. Yariv and P. Yeh, *Optical Waves in Crystals* (Wiley, New York, 1984).

[34] J. K. Wahlstrand, Ph.D. Dissertation, University of Michigan, 2005.

[35] D. H. Auston, K. P. Cheung, and P. R. Smith, Appl. Phys. Lett. **45**, 284 (1984).

[36] P. R. Smith, D. H. Auston, and M. C. Nuss, IEEE J. Quantum Electron. **24**, 255 (1988).

[37] J. T. Darrow, X.-C. Zhang, D. H. Auston, and J. D. Morse, IEEE J. Quantum Electron. **28**, 1607 (1992).

[38] L. Duvillaret, F. Garet, J.-F. Roux, and J.-L. Coutaz, IEEE J. Sel. Top. Quantum Electron. **7**, 615 (2001).

[39] D. Grischkowsky and N. Katzenellenbogen, *Femtosecond pulses of terahertz radiation: Physics and applications*, in Picosecond Electronics and Optoelectronics, T. C. L. G. Sollner and J. Shah, eds. Vol. 9 of OSA Proceedings Series, pp .9-14 (Optical Society of America, Washington, D.C., 1991).

[40] S. Gupta, J. F. Whitaker, and G. A. Mourou, IEEE J. Quantum Electron **28**, 2464 (1992).

[41] *User's Manual Tera-SED3 Large-area Terahertz Emitter* (Gigaoptics, GmbH., Konstanz, Germany, 2006).

[42] A. Dreyhaupt, S. Winnerl, M. Helm, and T. Dekorsy, Opt. Lett. **31**, 1546 (2006).

[43] Y.R. Shen, *The Principles of Nonlinear Optics* (Wiley, New York, 1984).

[44] A. Schneider, Phys. Rev. A **82**, 033825 (2010).

[45] K. Reimann, Rep. Prog. Phys. **70**, 1597 (2007).

[46] D. Ct, J. E. Sipe, and H. M. van Driel, J. Opt. Soc. Am. B **20**, 1374 (2003).

[47] G. Gallot and D. Grischkowsky, J. Opt. Soc. Am. B **16**, 1204 (1999).

[48] Q. Wu and X.-C. Zhang, Appl. Phys. Lett. **71**, 1285 (1997).

[49] Y. C. Shen, P. C. Upadhya, H. E. Beere, E. H. Linfield, A. G. Davies, I. S. Gregory, C. Baker, W. R. Tribe, and M. J. Evans, Appl. Phys. Lett. **85**, 164 (2004).

[50] I. -C. Ho, X. Guo, and X. -C. Zhang, Opt. Express **18**, 2872 (2010).

[51] R. Huber, A. Brodschelm, F. Tauser, and A. Leitenstorfer, Appl. Phys. Lett. **76**, 3191 (2000).

[52] A. Schneider, M. Neis, M. Stillhart, B. Ruiz, R. U. A. Khan, and P. Gunter, J. Opt. Soc. Am. B **23**, 1822 (2006).

[53] I. S. Gregory, C. Baker, W. R. Tribe, M. J. Evans, H. E. Beere, E. H. Linfield, A. G. Davies, and M. Missous, Appl. Phys. Lett. **83**, 4199 (2003).

[54] J. K. Wahlstrand and R. Merlin, Phys. Rev. B **68**, 054301 (2003).

[55] T. E. Stevens, J. K. Wahlstrand, J. Kuhl, and R. Merlin, Science **291**, 627 (2001).

[56] A. Nahata, A. S. Weling, and T. Heinz, Appl. Phys. Lett. **69**, 2321 (1996).

[57] D. F. Parsons and P. D. Coleman, Appl. Opt. **10**, 1683 (1971).

[58] Dynamic range in time domain is defined as the peak of a signal divided by its rms value of noise floor before the pulse. In the frequency domain, we compare the peak of a signal to the peak of its noise floor at 20 THz, where the signal vanishes.

[59] J. W. Goodman, *Introduction to Fourier Optics*, 2nd ed. (McGraw-Hill, New York, 1996), Chap. 6.

[60] A. Leitenstorfer, S. Hunsche, J. Shah, M. C. Nuss, and W. H. Knox, Appl. Phys. Lett. **74**, 1516 (1999).

[61] G. L. Dakovski, B. Kubera, and J. Shan, J. Opt. Soc. Am. B **22**, 1667 (2005).

[62] G. Gallot, J. Zhang, R. W. McGowan, T.-I. Jeon, and D. Grischkowsky, Appl. Phys. Lett. **74**, 3450 (1999).

[63] H. D. Riccius, J. Appl. Phys. **39**, 4381 (1968).

[64] H. M. Randall, D. M. Dennison, N. Ginsburg, and L. R. Weber, Phys. Rev. **52**, 160 (1937).

[65] S. Winnerl, F. Peter, A. Dreyhaupt, B. Zimmermann, M. Wagner, H. Schneider, M. Helm, and K. Khler, IEEE J. Sel. Top. Quantum Electron. **14**, 449 (2008).

[66] G. Chang, C. J. Divin, J. Yang, M. A. Musheinish, S. L. Williamson, A. Galvanauskas, and T. B. Norris, Opt. Express **15**, 16308 (2007).

[67] Y.-R. Shen, Prog. Quantum Electron. **4**, 207 (1976).

[68] Y. Li, F. Liu, Y. Li, L. Chai, Q. Xing, M. Hu, and C. Wang, Appl. Opt. **50**, 1958 (2011).

[69] M. Grimsditch, L.E. McNeil, and D.J. Lockwood, Phys. Rev. B **58**, 14462 (1998).

[70] P. J. Gielisse, J. N. Plendl, L. C. Mansur, R. Marshal, S. S. Mitra, R. Mykolajewycz, and A. Smakula, J. Appl. Phys. **36**, 2446 (1965).

[71] S. Mochizuki and M. Satoh, Phys. Stat. Sol. B **106**, 667 (1981).

[72] R.E. Dietz, G.I. Parisot, and A.E. Meixner, Phys. Rev. B **4**, 2302 (1971).

[73] A.J. Sievers III and M. Tinkham, Phys. Rev. **129**, 1566 (1963).

[74] W. G. Nilsen and J. G. Skinner, J. Chem. Phys. **48**, 2240 (1968).

[75] C. Kittel, *Introduction to Solid State Physics*, 7th ed. (Wiley, New York, 1975).

[76] T. Ostapchuk, J. Petzelt, V. Zelezny, A. Pashkin, J. Pokorny, I. Drbohlav, R. Kuzel, D. Rafaja, B. P. Gorshunov, M. Dressel, C. Ohly, S. Hoffmann-Eifert, and R. Waser, Phys. Rev. B **66**, 235406 (2002).

[77] R.A. Cowley, Phys. Rev. Lett. **9**, 159 (1962).

[78] K. Kamars, K.L. Barth, F. Keilmann, R. Henn, M. Reedyk, C. Thomsen, M. Cardona, J. Kircher, P. L. Richards, and J.L. Stehl, J. Appl. Phys. **78**, 1235 (1995).

[79] A. Sihvola, *Electromagnetic Mixing Formulas and applications*, (IET, 1999).

[80] G.W. Milton, J. Appl. Phys. **52**, 5286 (1981).

[81] D.J. Bergman and D. Stroud, Solid State Phys. **46**, 148 (1992).

[82] D. E. Aspnes, Am. J. Phys. **50**, 704 (1982).

[83] K. Peiponen and E. Gornov, Opt. Lett. **31**, 2202 (2006).

[84] Y. Kantor and D.J. Bergman, J. Phys. C, **15**, 2033 (1982).

[85] J. D. Jackson, *Classical Electrodynamics*, 3rd ed. (Wiley: New York, 1998).

[86] P. Mallet, C. A. Gurin, and A. Sentenac, Phys. Rev. B **72**, 014205 (2005).

[87] J. van Kranendonk and J.E. Sipe, Prog. Opt. **15**, 245 (1977).

[88] M. Born and E. Wolf, *Principles of Optics*, 7th ed. (Cambridge University Press, 1999).

[89] W. T. Doyle, J. Appl. Phys. **49**, 795 (1978).

[90] F. Claro, Phys. Rev. B **25**, 2483 (1982).

[91] C.F. Bohren and D.R. Huffman, *Absorption and Scattering of Light by Small Particles*, (New York: Wiley, 1983).

[92] R. Ruppin, *Electromagnetic Surface Modes*, edited by A. D. Boardman (Wiley, New York, 1982).

[93] R. Ruppin and R. Englman, Rep. Prog. Phys. **33**, 149 (1970).

[94] A. Sihvola and I.V. Lindell, Geoscience and Remote Sensing Symposium, IGARSS'89, p. 929 (1989).

[95] R. W. Cohen, G. D. Cody, M. D. Coutts, and B. Abeles, Phys. Rev. B **8**, 3689 (1973).

[96] J.A. Osborn, Phys. Rev. **67**, 351 (1945).

[97] A.H. Sihvola and J. A. Kong, IEEE Trans. Geosci. Remote Sensing **26**, 420 (1988).

[98] R. Summitt, Spectrochim. Acta **23**, 2857 (1967).

[99] S. Hayashi, N. Nakamori, J. Hirono, and H. Kanamori, J. Phys. Soc. Japan **43**, 2006 (1977).

[100] J.R. Luxon, D.J. Montgomery, and R. Summit, Phys. Rev. **188**, 1345 (1969).

[101] R. Fuchs, Phys. Rev. B **11**, 1732 (1975).

[102] I.J. Dayawansa and C.F. Bohren, Phys. Stat. Sol. (b) **86**, K27 (1978).

[103] Ref. 66, p. 361.

[104] J.R. Aronson and A. G. Emslie, J. Geophys. Res. **80**, 4925 (1975).

[105] D.R. Huffman, Festkrperprobleme (Advances in Solid State Physics) **23**, 49 (1983).

[106] M. Born and K. Huang, *Dynamical Theory of Crystal Lattices* (Oxford Univ. Press, Oxford, 1998).

[107] G. Mie, Ann. Phys. **25**, 377 (1908); G. Mie, *Contributions to the Optics of Turbid Media: Particularly of Colloidal Metal Solutions*, Issue 1873 of Royal Aircraft Establishment (Library translation), pp. 1-142 (H.M. Stationery Office, 1976).

[108] J. A. Stratton, *Electromagnetic Theory* (McGraw-Hill, New York, 1941).

[109] R. Fuchs and K.L. Kliewer, J. Opt. Soc. Am. **58**, 319 (1968).

[110] K. M. Haussler, Phys. Stat. Sol. (b) **105**, K81 (1981).

[111] S. D. Kirby, M.S. Dissertation, Cornell University, 2006, Ch. 2.